Informe del Uso de la Supercomputadora

Presentado por la Dra. Vicenta Sánchez Morales

El tiempo de supercómputo asignado para el proyecto “Transporte Cuántico en Sólidos Aperiódicos con y sin Impurezas Aplicando Campo Eléctrico” nos ha permitido publicar dos artículos en revistas indexadas y una memoria de congreso. Además, dos de los alumnos participantes en el proyecto obtuvieron su grado de Maestría y nos permitió participar en cuatro congresos internacionales. A continuación, se resume los avances de la investigación

Estudiamos el transporte electrónico por medio de los métodos de renormalización en espacio real desarrollados previamente para la fórmula de Kubo-Greenwood en sistema cuasiperiódicos y aperiódicos, donde el arreglo atómico sigue la secuencia de Fibonacci generalizada. Además, desarrollamos un nuevo método de renormalización unificado para el inverso de la razón de participación (IPR) en cadenas de Fibonacci generalizada, con el objetivo de estudiar la localización electrónica. Encontramos una ecuación analítica para el coeficiente de Lyapunov de una cadena periódica. Nuestros resultados muestran que, si las redes son cuasiperiódicas, el promedio espectral de la conductividad DC y de la razón de participación decaen siguiendo una ley de potencias cuando la longitud de las redes se incrementa. En cambio, si las redes son aperiódicas este promedio espectral decae suavemente. También realizamos un análisis detallado del espectro de la conductividad AC tanto para sistemas cuasiperiódicos como para no-cuasiperiódicos, encontrando zonas de muy alta conductividad (más de tres órdenes de magnitud) que superan ampliamente a la de los sistemas balísticos. En paralelo, se desarrollaron nuevos métodos de renormalización para la matriz de transferencia con el fin de estudiar la transmitancia fotónica en multicapas aperiódicas. Las capas siguen las secuencias de Fibonacci generalizada, Thue Morse generalizada, doble periodo y Rudin Shapiro. Nuestros resultados muestran un pico de transmisión perfecta en $\lambda=\lambda_0$ para multicapas con simetría de espejo y considerando la condición de un cuarto de onda. Se realizó un análisis detallado del ancho de este pico para diseñar un mejor filtro. Además, se varió el ángulo de incidencia para las polarizaciones transversal eléctrica y transversal magnética, encontrando que esta última no destruye el pico solo lo recorre suavemente. Estos resultados fueron la base del protocolo de investigación del alumno Juan Guillermo Munguía Fernández, que aprobó su examen de candidatura al grado de doctor en el Posgrado de Ciencias e Ingeniería de Materiales de la UNAM, presentado el 25 de mayo de 2016. También empezamos el estudio de las propiedades ópticas y electrónicas de los nanoalambres ramificados de silicio con y sin impurezas de oxígeno por medio de la teoría del funcional de la densidad. Los primeros resultados muestran que el ancho de la banda prohibida de energía (gap) depende fuertemente de la longitud de las ramas, decreciendo cuando la rama crece. El ancho de este gap depende también del número y la posición de las ramas, por lo que estamos haciendo un estudio detallado para cuantificar el número, su ancho y posición de las ramas con el objetivo de aumentar su adsorción y disminuir su reflectividad. Estos resultados fueron la base del protocolo de la alumna Adriana Patricia Gutiérrez

Rodríguez, que se tituló de Maestría por medio del examen general de conocimientos en el Posgrado en Ciencias e Ingeniería de Materiales de la UNAM.

Estudiamos la termoelectricidad en nanocintas y nanoalambres segmentados dentro del formalismo de Boltzmann a través del método de renormalización más convolución en espacio real desarrollado para la fórmula de Kubo-Greenwood, considerando los modelos de amarre fuerte y de Born. Para los nanoalambres periódicos, observamos un máximo de la figura de mérito termoeléctrica (ZT) en el espacio de temperaturas, como el que se reporta cuando varia la concentración de portadores. Este máximo de ZT se mejora si introducimos nanoalambres periódicamente segmentados y con sección transversal inhomogénea. Al considerar nanoalambres cuasiperiódicos el máximo de ZT es mayor que el de los sistemas periódicos.

Se enlistan los productos resultado de la investigación:

Artículos

1. Fernando Sánchez, Vicenta Sánchez y Chumin Wang,
   "Renormalization approach to the electronic localization and transport in macroscopic generalized Fibonacci lattices",
   Journal of Non-Crystalline Solids **450**, 194 (2016).
   http://dx.doi.org/10.1016/j.jnoncrysol.2016.07.031
2. J. Eduardo González, Vicenta Sánchez y Chumin Wang,
   "Improving Thermoelectric Properties of Nanowires Through Inhomogeneity"
   Journal of Electronic Materials. (2016). doi:10.1007/s11664-016-4946-y
3. J. Eduardo Gonzalez, Vicenta Sanchez y Chumin Wang,
   "Thermoelectricity in periodic and quasiperiodically segmented nanobelts and nanowires"
   Mater. Res. Soc Advances (2016) doi: https://doi.org/10.1557/adv.2016.291

Formación de recursos humanos

1. *Adriana Patricia Gutiérrez Rodríguez.* Obtuvó el grado de Maestra en Ciencia e Ingeniería de Materiales de la UNAM bajo mi supervisión, con el título del protocolo de investigación "*Fenómeno de resonancias en nanoalambres ramificados*", el 26 de julio de 2016.

2. *Abraham Lima Buendía,* Obtuvó el grado de Maestro en Ciencias (Física) de la UNAM bajo mi supervisión, con el título del protocolo de investigación "*Interacción electrón-electrón en la localización y superconductividad en sistemas aperiódicos*", el día 27 de enero de 2017.

Congresos

1. V. Sánchez,
   "Photonic localization and transmittance in macroscopic aperiodic multilayers" en The 3rd Conference on Physical Chemistry (CPC 2016), en Nanjing, China del 1 al 3 de junio de 2016.
2. , F. Sánchez V. Sánchez y C. Wang,
   "Electronic localization and transport in macroscopic generalized Fibonacci lattices: A renormalization approach" en el The Condensed Matter Division of the European Physical Society (CMD 26), en Groningen, Paises bajos del 4 al 9 de septiembre de 2016.
3. V. Sánchez, J.G. Munguia-Fernandez y C. Wang,
   "Quasiperiodicity and mirror symmetry in photonic devices" en el Energy Materials Nanotechnology Meeting on Materials Chemistry (EMN 2016), en Budapest, Hungría del 9 al 13 de septiembre de 2016.
4. V. Sánchez, F. Sánchez y C. Wang,
   "Resonant AC and optical absorption spectra of aperiodic branched nanowires" en el The 2015 Materials Research Society Fall Meeting, en Boston, USA del 27 de noviembre al 2 de diciembre de 2016.

Dado que nuestra investigación es de índole teórico la supercomputadora es una herramienta esencial para llevar a cabo la modelación y simulación de las propiedades físicas de los sólidos no periódicos con y sin impurezas, debido a que estos no cuentan con espacio reciproco y los sistemas que consideramos son de aproximadamente 10^8 átomos, por lo que nuestros cálculos requieren de cuádruple precisión. Por lo anterior es de suma importancia la utilización de la supercomputadora.

Atentamente

Dra. Vicenta Sánchez Morales

Profesora Titular "B" de T.C.
Facultad de Ciencias, UNAM
Tel: 56224973

Journal of Non-Crystalline Solids 450 (2016) 194–208

Contents lists available at ScienceDirect

Journal of Non-Crystalline Solids

journal homepage: www.elsevier.com/locate/jnoncrysol

Renormalization approach to the electronic localization and transport in macroscopic generalized Fibonacci lattices

Fernando Sánchez [a], Vicenta Sánchez [a], Chumin Wang [b,*]

[a] Departamento de Física, Facultad de Ciencias, Universidad Nacional Autónoma de México, Mexico City, Mexico
[b] Instituto de Investigaciones en Materiales, Universidad Nacional Autónoma de México, Mexico City, Mexico

ARTICLE INFO

Article history:
Received 22 April 2016
Received in revised form 16 July 2016
Accepted 23 July 2016

Keywords:
Kubo-Greenwood formula
Real-space renormalization method
Generalized Fibonacci lattices

ABSTRACT

Electronic transport and wavefunction localization are two closely related phenomena, but their behavior in truly macroscopic aperiodic lattices is a non-widely addressed issue. We study in this article the electrical conductivity of generalized Fibonacci (GF) lattices through the Kubo-Greenwood formula, while the localization of electronic wavefunction is analyzed by means of the Lyapunov exponent and participation ratio (*PR*). For periodic chains, an analytical expression of the Lyapunov exponent is obtained. We have also developed for the first time a real-space renormalization method to calculate the *PR* of macroscopic GF lattices described by tight-binding Hamiltonians. Moreover, we report a novel unified renormalization method for the Kubo-Greenwood formula applied to GF chains. For quasiperiodic lattices, the results reveal a power-law decay of the spectral averages for both *PR* and DC conductivity when the system length increases. In addition, we present a systematic analysis of the AC conductivity spectra observing truly large resonant peaks in comparison to the ballistic one. The electrical conductance of GF nanowires is also investigated. Finally, the results suggest that *PR* could not be proper for the analysis of critically localized states.

© 2016 Elsevier B.V. All rights reserved.

1. Introduction

The structural disorder of a solid can profoundly modify the nature of electronic states. It is well known that they are all extended in periodic lattices and exponentially localized in random-disordered systems of one and two dimensions [1]. However, the degree of localization in other non-periodic systems is still an unclear subject. In fact, delocalized electronic states are found in one-dimensional systems with correlated disorder [2,3] and some of these results have been experimentally confirmed [4,5].

Nowadays, the study of electronic states in artificial structures is of great importance in condensed matter physics, because they introduce many new physical properties essential for technological applications of atomic-scale devices. These structures can be multilayers, quantum wires, rings, or dots, etc. In particular, quasiperiodic and aperiodic systems become a subject of remarkable interest since the discovery of quasicrystals [6] and the fabrication of high-quality superlattices including quasiperiodic ones [7], whose Raman spectrum has a good agreement with the theory [8]. Much attention has been devoted to the Fibonacci lattice, because it provides a prototype structure for studying quasiperiodic systems and possesses critically localized electronic states [9]. The corresponding energy spectrum is neither absolutely continuous nor pure point, but singular continuous [10].

There is a generalization of the Fibonacci sequence obtained by the substitutions $A \to A^m B^n$ and $B \to A$, where m and n are positive integer numbers. The symbol A^m represents a string of m A's. The original Fibonacci sequence is recovered when $m = n = 1$ and generalized ones with $m > 1$ and $n = 1$ are called precious means, while metallic means stand for sequences with $m = 1$ and $n > 1$ [11]. Along last two decades, the electronic, vibrational, and optical properties of generalized Fibonacci (GF) lattices have been investigated [11–14]. In particular, real-space renormalization-group methods based on the decimation technique were developed for calculating the local density of states at any given site [15] and the average Green's functions [16] of several macroscopic GF lattices. Moreover, the total density of states and the electrical conductivity in mixing Fibonacci chains with $m = n = 1$ are investigated [17], and the alternating current (AC) of transparent states is also analyzed [18] observing a decreasing oscillatory behavior as occurred in periodic lattices, in contrast to the resonant AC conduction found at bandgap energies [19].

In this article, we report a detailed analysis of the electrical conductivity, Lyapunov coefficient, and participation ratio (*PR*) of GF lattices with macroscopic length. This analysis was carried out by means of a real-space renormalization method capable to address truly macroscopic systems without introducing any additional approximations, whose mathematical formulations are presented in Appendices *A*, *B* and *C*. We will introduce the GF sequences in section two, and define the localization and transport physical quantities in section three. The results of both direct current (DC) conductivity and the wavefunction localization

* Corresponding author.
E-mail address: chumin@unam.mx (C. Wang).

http://dx.doi.org/10.1016/j.jnoncrysol.2016.07.031
0022-3093/© 2016 Elsevier B.V. All rights reserved.

are presented in section four, while the AC conduction is investigated in section five. We further discuss the electronic transport and localization in GF nanowires with a square cross-section in section six. Finally, the conclusions of this study are given in section seven.

2. Generalized Fibonacci sequences

The Fibonacci chains can be studied in several forms, for example, by using two sorts of bonds (bond problem), two kinds of atoms (site problem) or a combination of both (mixing problem) [17]. In this paper, we analyze the bond problem, in which two hoping integrals, t_A and t_B, are arranged following the GF sequences and the nature of atoms are assumed to be the same with a null self-energy. The GF sequences (S_l) can be built by using the following addition scheme [13,20],

$$\begin{aligned} &S_0(m,n)=\{B\},\ \ S_1(m,n)=\{A\},\\ &\text{and }\ S_l(m,n)=S_{l-1}^{m}(m,n)\oplus S_{l-2}^{n}(m,n), \end{aligned} \tag{1}$$

where l is the generation index, m and n are positive integers that define the type (m,n) of GF sequences. For example, $S_2(2,1)=\{AAB\}$ and $S_3(2,1)=\{AABAABA\}$. These $S_l(m,n)$ can also be obtained by the substitution rules given by [20,21]

$$A\rightarrow A^{m}B^{n}\ \text{ and }\ B\rightarrow A, \tag{2}$$

which may be rewritten by using the substitution matrix ($\mathbf{M}$) as [22]

$$\begin{aligned} \begin{pmatrix} A\\ B\end{pmatrix}\rightarrow \boldsymbol{M}\begin{pmatrix} A\\ B\end{pmatrix}&=\begin{pmatrix} m & n\\ 1 & 0\end{pmatrix}\begin{pmatrix} A\\ B\end{pmatrix}\\ &=\begin{pmatrix} \underbrace{AA\cdots A}_{m} & \underbrace{BB\cdots B}_{n}\\ A & \end{pmatrix}. \end{aligned} \tag{3}$$

Matrix $\mathbf{M}$ has the following eigenvalues ($\lambda_{\pm}$),

$$\begin{aligned} \begin{vmatrix} m-\lambda & n\\ 1 & -\lambda\end{vmatrix}=0 \qquad &\Rightarrow \lambda^2-m\lambda-n=0\\ \Rightarrow\ \lambda_{\pm}&=\frac{m\pm\sqrt{m^2+4n}}{2}. \end{aligned} \tag{4}$$

For $n=1$, Eq. (4) leads to $\lambda_{+}>1$ and $|\lambda_{-}|<1$, which fulfill the Pisot condition [22,23].

Moreover, the determinant of $\mathbf{M}$,

$$\begin{vmatrix} m & n\\ 1 & 0\end{vmatrix}=-n, \tag{5}$$

is unimodular if $n=1$. Hence, the corresponding sequence is called quasiperiodic and possesses Bragg-peak diffraction spectra, because both the Pisot eigenvalue condition and the unit-determinant requirement of $\mathbf{M}$ are satisfied [24]. Conversely, the GF sequences with $n\neq 1$ do not satisfy the Pisot condition neither the unit-determinant requirement, thus they are not quasiperiodic. Among non-quasiperiodic structures, the Thue-Morse sequence is another widely studied one, since it accomplishes the Pisot condition but has a non-unimodular substitution matrix; in consequence, it is not quasiperiodic neither [25].

The total number of A and B in $S_l(m,n)$, denoted by $F_l(m,n)$, satisfies the relation

$$F_l(m,n)=mF_{l-1}(m,n)+nF_{l-2}(m,n) \tag{6}$$

with $F_0(m,n)=F_1(m,n)=1$. At the limit of infinite length, the ratio of $F_l(m,n)$ for subsequent generations defined as

$$\tau(m,n)\equiv\lim_{l\to\infty}\frac{F_{l+1}(m,n)}{F_l(m,n)} \tag{7}$$

satisfies the quadratic equation $\tau^2-m\tau-n=0$, whose positive solution is

$$\tau(m,n)=\frac{m+\sqrt{m^2+4n}}{2}. \tag{8}$$

In fact, the irrational number $\tau(1,1)=(1+\sqrt{5})/2$ is referred as the golden mean, $\tau(2,1)=1+\sqrt{2}$ as the silver mean, $\tau(3,1)=(3+\sqrt{13})/2$ as the bronze mean, $\tau(1,2)=2$ as the copper mean, and $\tau(1,3)=(1+\sqrt{13})/2$ as the nickel mean.

Both substitution and addition methods for the nine GF sequences, with m and $n=1$, 2 or 3, analyzed in this paper are summarized in Table 1. Segments of these GF chains for the bond problem are illustrated in Fig. 1, where the initial conditions were $S_0(m,n)=\{B\}$ and $S_1(m,n)=\{A\}$. Notice that for a given generation l, a GF chain of type (3,3) has more atoms than a standard Fibonacci chain with (1,1).

In the next section, we describe the model used for the study of electronic transport and localization of wavefunctions in GF chains defined in this section.

3. Modeling electronic transport and localization

In order to isolate the quasicrystalline effects on the physical properties of GF chains, let us consider a single-band tight-binding Hamiltonian (H) given by

$$H=\sum_{<i,j>}t_{i,j}\{|i><j|+|j><i|\}, \tag{9}$$

where $|j\rangle$ represents the Wannier function of atom j with null self-energy and $t_{i,j}$ is the hopping integral between nearest-neighbor sites i and j, indicated by $\langle i,j\rangle$, which may be t_A or t_B arranged according to the GF sequences.

The density of states (DOS) can be calculated by means of the retarded single-electron Green's function (G) [26],

$$DOS(E)=-\frac{1}{\pi}\lim_{\eta\to 0^{+}}\mathrm{Im}Tr[G(E+i\eta)], \tag{10}$$

where η is the imaginary part of energy (E) and the Green's function is determined by the Dyson equation given by $(E-H)G=1$.

The electronic wavefunction ($|\psi>=\sum_j c_j|j>$) satisfies the stationary Schrödinger's equation, which for both periodic or non-periodic chains described by Hamiltonian (Eq. (9)) can be written as

$$\boldsymbol{C}_{j+1}=\boldsymbol{T}_j\boldsymbol{C}_j, \tag{11}$$

where

$$\begin{aligned} \boldsymbol{T}_j&=\begin{pmatrix} E/t_{j,j+1} & -t_{j,j-1}/t_{j,j+1}\\ 1 & 0\end{pmatrix}\\ &\text{and }\ \boldsymbol{C}_j=\begin{pmatrix} c_j\\ c_{j-1}\end{pmatrix} \end{aligned} \tag{12}$$

are respectively the transfer matrix and amplitude vector of the wavefunction. The amplitude vectors of atoms at the begin and end of the chain are related by the product of transfer matrices,

$$\boldsymbol{T}_N\boldsymbol{T}(l)\boldsymbol{T}_1\equiv\boldsymbol{T}_N\left(\prod_{j=2}^{N-1}\boldsymbol{T}_j\right)\boldsymbol{T}_1=\begin{pmatrix}\tau_{11} & \tau_{12}\\ \tau_{21} & \tau_{22}\end{pmatrix}, \tag{13}$$

where N is the number of atoms in the chain of generation l,

$$\boldsymbol{T}(l)=\prod_{j=2}^{N-1}\boldsymbol{T}_j, \tag{14}$$

Table 1
Substitution and addition rules for the GF sequences of type (m, n).

	n = 1	n = 2	n = 3
m = 1	$A\to AB$ & $B\to A$ $S_l = S_{l-1}\oplus S_{l-2}$	$A\to ABB$ & $B\to A$ $S_l = S_{l-1}\oplus 2S_{l-2}$	$A\to ABBB$ & $B\to A$ $S_l = S_{l-1}\oplus 3S_{l-2}$
m = 2	$A\to AAB$ & $B\to A$ $S_l = 2S_{l-1}\oplus S_{l-2}$	$A\to AABB$ & $B\to A$ $S_l = 2S_{l-1}\oplus 2S_{l-2}$	$A\to AABBB$ & $B\to A$ $S_l = 2S_{l-1}\oplus 3S_{l-2}$
m = 3	$A\to AAAB$ & $B\to A$ $S_l = 3S_{l-1}\oplus S_{l-2}$	$A\to AAABB$ & $B\to A$ $S_l = 3S_{l-1}\oplus 2S_{l-2}$	$A\to AAABBB$ & $B\to A$ $S_l = 3S_{l-1}\oplus 3S_{l-2}$

and the transfer matrices that connect the system to the semi-infinite periodic leads with null self-energies and hopping integrals t are

$$\boldsymbol{T}_1 = \begin{pmatrix} E/t_{1,2} & -t/t_{1,2} \\ 1 & 0 \end{pmatrix} \quad \text{and} \quad \boldsymbol{T}_N = \begin{pmatrix} E/t & -t_{N-1,N}/t \\ 1 & 0 \end{pmatrix}. \tag{15}$$

From Eq. (13), the transmittance (T) of a linear chain is given by [27]

$$T(E) = \frac{4-\left(\frac{E}{t}\right)^2}{\left[\tau_{21}-\tau_{12}+\frac{(\tau_{22}-\tau_{11})E}{2t}\right]^2 + (\tau_{22}+\tau_{11})^2\left(1-\frac{E^2}{4t^2}\right)}. \tag{16}$$

The electrical conductance (g) can be calculated through the Landauer formula [28]

$$\mathrm{g}(E) = \frac{2e^2}{h}T(E) = \mathrm{g}_0 T(E), \tag{17}$$

where $\mathrm{g}_0 \equiv 2e^2/h$ is the quantum of conductance.

The localization of wavefunction can be analyzed by looking at the Lyapunov coefficient (γ) and the participation ratio (PR), which are respectively defined by [27]

$$\gamma(E) = \frac{1}{N}\ln\sqrt{\tau_{1,1}^2+\tau_{1,2}^2+\tau_{2,1}^2+\tau_{2,2}^2} \quad \text{and} \quad PR(E) = \left(\sum_{j=1}^{N}|c_j(E)|^4\right)^{-1}. \tag{18}$$

In general, the inverse of γ is interpreted as the localization length if the wavefunction is exponentially localized. On the other hand, PR counts the number of atoms that contributes to a normalized wavefunction, *e.g.*, $PR = N$ for a fully extended state and $PR = 1$ for a wavefunction with amplitude only at a single atom.

Within the linear response theory, the electrical conductivity can be calculated by means of the Kubo-Greenwood formula [29],

$$\sigma(\mu,\omega,T) = \frac{2e^2\hbar}{\Omega\pi m^2}\int_{-\infty}^{\infty} \mathrm{d}E \frac{f(E)-f(E+\hbar\omega)}{\hbar\omega} \times \mathrm{Tr}\left[p\ \mathrm{Im}G^+(E+\hbar\omega)\ p\ \mathrm{Im}G^+(E)\right], \tag{19}$$

where Ω is the system volume, $p = \frac{im}{\hbar}[H,x] = \sum_j\{t_{j,j+1}|j><j+1| - t_{j,j-1}|j><j-1|\}$ is the projection of the momentum operator along the applied electrical field, $G^+(E) = G(E+i\eta)$ is the retarded one-particle Green's function, and $f(E) = \{1+\exp[(E-\mu)/k_BT]\}^{-1}$ is the Fermi-Dirac distribution with the chemical potential μ and temperature T.

For a periodic linear chain of N atoms with null self-energies and hopping integral t, connected to two semi-infinite periodic leads with the same t, the AC conductivity at zero temperature has an analytical solution of [30]

$$\sigma_P(\mu,\omega,0) = \frac{8e^2t^2a}{\pi(N-1)\hbar^3\omega^2}\left[1-\left(\frac{\mu}{2t}\right)^2\right] \times \left\{1-\cos\left[\frac{(N-1)\hbar\omega}{2t\sqrt{1-(\mu/2t)^2}}\right]\right\}, \tag{20}$$

when $-2|t| \le \mu \le 2|t|$. In particular, its DC conductivity for $\omega \to 0$ is

$$\sigma_P \equiv \sigma_P(\mu,0,0) = \frac{e^2a}{\pi\hbar}(N-1). \tag{21}$$

It is easy to verify that $\sigma_P(\mu,\omega,0) \le \sigma_P$ for $-2|t| \le \mu \le 2|t|$. Analytical solutions can also be found for the density of states $DOS(E) = N(\pi\sqrt{4t^2-E^2})^{-1}$, the participation ratio $PR(E) = N$ and the Lyapunov coefficient

$$\gamma_p(E) = \frac{1}{2N}\ln\left\{2+\frac{E^2}{t^2}\left[f(N-1)+2\sum_{i=0}^{N-2}f(i)\right]\right\} \tag{22}$$

where

$$f(J) = \sum_{l=0}^{\lfloor J/2\rfloor}\frac{(-1)^l(J-l)!}{l!(J-2l)!}\left(\frac{E^2}{t^2}-2\right)^{J-2l}. \tag{23}$$

However, there are no general analytical solutions for these physical quantities in long GF chains and they are calculated in this article by means of the real-space renormalization method, whose procedure can be illustrated for the case of transfer matrix, by using the method of addition given by Eq. (1) and by taking the advantage of the associativity of matrix products. For example, the transfer matrix of a (m,n)-type GF chain of generation l can be calculated by

$$\boldsymbol{T}(l) = [\boldsymbol{T}(l-2)]^n\boldsymbol{T}_M[\boldsymbol{T}(l-1)]^m, \tag{24}$$

where the middle connecting matrix ($\boldsymbol{T}_M$) is given by

$$\boldsymbol{T}_M = \begin{pmatrix} E/t_A & -t_M/t_A \\ 1 & 0 \end{pmatrix} \tag{25}$$

being $t_M = t_A$ if l is odd and $t_M = t_B$ if l is even. In other words, the transfer matrix of generation l can be obtained just by multiplying n times the transfer matrix of generation $l-2$ and m times the transfer matrix of generation $l-1$. Nevertheless, the formulation of this renormalization procedure for the DOS and PR is considerably more complex, whose mathematical details are respectively given in Appendices A and B. It is worth mentioning that once these new renormalization methods are developed, the computing time is proportional to the generation number l, *i.e.*, it is proportional to the logarithm of the system length.

In the next section, we present the results of DOS, DC conductivity, Lyapunov coefficient, and participation ratio for the nine GF chains of type (m,n) with m and n equal to 1, 2, or 3.

4. Localization and DC conductivity

In order to study macroscopic GF chains with lengths of 10^8 atoms, different generation numbers (l) are chosen for each type of GF chains, as specified in Table 2.

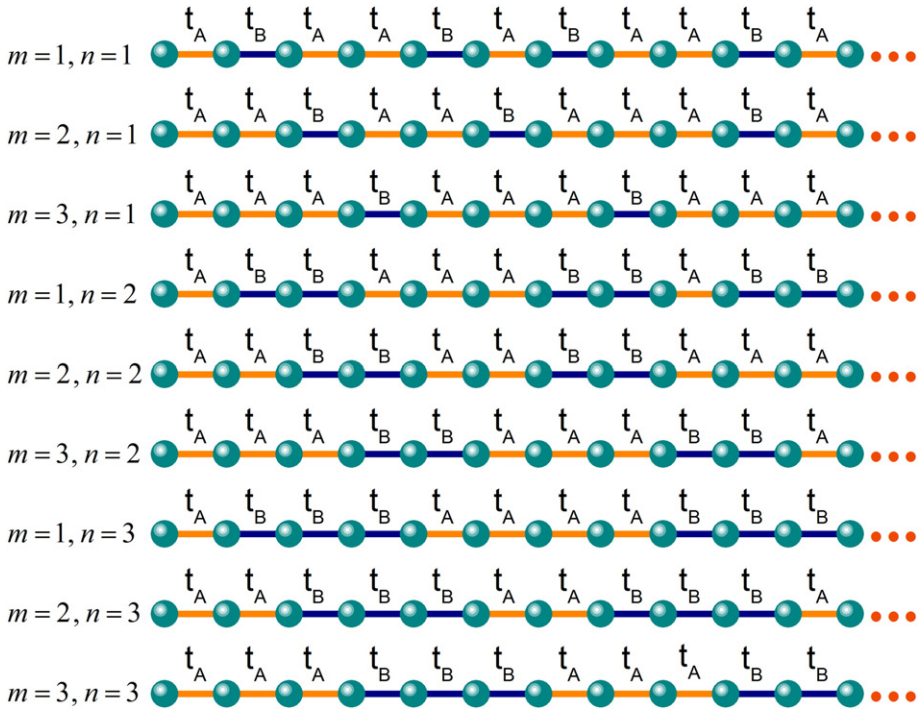

Fig. 1. Segments of generalized Fibonacci chains of type (m,n) defined by Eq. (2) for the bond problem with m and n equal to 1, 2, or 3. Two hopping strengths of bonds, t_A and t_B, are indicated.

For the sake of simplicity, a uniform bond length (a) is taken and the aperiodicity is introduced through the order of hopping integrals t_A and t_B. Two semi-infinite periodic leads with null self-energy and hopping integral t are connected to the ends of all analyzed GF chains. In these leads, a phase difference of $e^{i\theta}$ between the wavefunction amplitudes of nearest-neighbor sites is considered, where θ satisfies the dispersion relation $E=2t\cos\theta$. In Fig. 2(a)–(l), spectra of the density of states (*DOS*), zero-temperature DC conductivity [$\sigma=\sigma(\mu,0,0)$], Lyapunov coefficient (γ) and participation ratio (*PR*) are plotted as functions of the chemical potential (μ) for the three GF chains with $n=1$, null self-energies, hopping integrals of $t_A=0.8\,t$ and $t_B=t$. The lengths of these chains are given in Table 2. The used imaginary part of the energy is $\eta=10^{-5}|t|$ for *DOS* in Fig. 2(a–c), $\eta=10^{-15}|t|$ for their magnifications in Fig. 2(a′–c′), and $\eta=10^{-13}|t|$ for σ in Fig. 2(d–f). Grids of 400,000 and of 1,594,324 chemical potentials are respectively used for plotting Fig. 2(a-i) and (j-l).

Notice that all spectra of *DOS*, σ, γ, and *PR* show the same band-gap structure for each type of GF chains. In particular, the inverse of Lyapunov coefficient (γ^{-1}) of Fig. 2(g–i) reveals localization lengths very close to those of the periodic chain (γ_P^{-1}). Such behavior is confirmed by the almost ballistic DC conductivity (σ_P) in each minibands, in contrast to a general small *PR* values. In fact, they are even smaller when t_A diminishes, contrary to practically unchanged σ and γ^{-1} values in each miniband whose bandwidth decreases with t_A. Magnifications of *DOS* spectra around $\mu=0$ are further presented in Fig. 2(a′–c′) and they confirm the fractal nature of these spectra from quasiperiodic chains [9].

It is worth mentioning that the *DOS* spectrum of Fig. 2(b) for the silver mean is very close to the band structure reported in Ref. [31], in which the total band width is slightly larger than ours since their hopping integrals were $t_A=t$ and $t_B=0.8\,t$. In addition, the silver mean sequence of Ref. [31] is an isomer of ours, *i.e.*, instead of $A\to AAB$ they used a substitution rule of $A\to ABA$. In fact, the three isomers of the silver mean have almost the same *DOS* spectra. However, the localization nature of their states could be very different. For example, there are analytical solutions for the transmittance (T) at $E=0$ and they are

$$T(E=0,l)=\begin{cases}4(\chi^{p}+\chi^{-p})^{-2}, & \text{for isomer } A\to AAB\\ 4(\chi^{l}+\chi^{-l})^{-2}, & \text{for isomer } A\to ABA\\ 4(\chi^{p}+\chi^{-p})^{-2}, & \text{for isomer } A\to BAA\end{cases}, \tag{26}$$

where $\chi=t_A/t_B$, $p=[1-(-1)^l]/2$ and l is the generation number. Notice that for the case $A\to ABA$ and $\chi\neq 1$, $T(E=0,l)\to 0$ when $l\to\infty$. But for the isomers $A\to AAB$ and $A\to BAA$, $T(E=0,l)=1$ when l is an even number, regardless the value of χ. Hence, we have always transparent states at $E=0$ in these two isomers with even generation numbers.

In Figs. 3 and 4, the density of states (*DOS*), zero-temperature DC conductivity (σ), Lyapunov coefficient (γ) and participation ratio (*PR*) as functions of the chemical potential (μ) are plotted for the GF chains with $n=2$ and $n=3$, respectively. The parameters for numerical calculations are the same as in Fig. 2, except that the lengths of these chains are given in Table 2.

Notice that in Fig. 3(d–f) the DC conductivity around $\mu=0$ is almost σ_P, despite of the minimum *DOS* at the same region observed in Fig. 3(a–c). In Fig. 3(a′–c′), magnifications of *DOS* around $\mu=0$ show oscillating behaviors, in contrast to the fractal one observed in Fig. 2(a′–c′) for quasiperiodic chains.

Table 2
Number of atoms in (m,n)-type GF chains of generation l.

N	$n=1$	$n=2$	$n=3$
$m=1$	433,494,438 for $l=42$	357,913,942 for $l=29$	315,732,482 for $l=24$
$m=2$	318,281,040 for $l=23$	268,377,089 for $l=20$	581,130,734 for $l=19$
$m=3$	239,244,623 for $l=17$	253,841,390 for $l=16$	187,869,862 for $l=15$

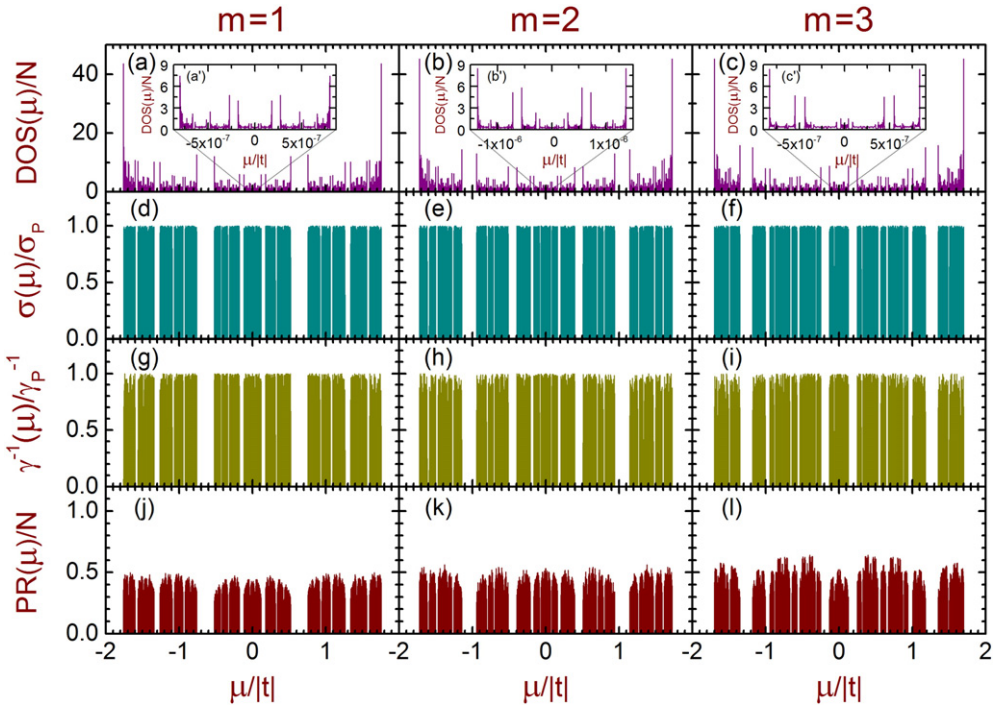

Fig. 2. Density of states (*DOS*), DC conductivity (σ), Lyapunov coefficient (γ) and participation ratio (*PR*) as functions of the chemical potential (μ) for three generalized Fibonacci chains with $n=1$, null self-energies, hopping integrals of $t_A=0.8t$ and $t_B=t$.

Contrast to Fig. 3, the high-conductivity zones in Fig. 4(d–f) are located outside the central region, correspondingly again to small values of *DOS* and an oscillating behavior as shown in Fig. 4(a′–c′). Note also that in Figs. 3 and 4, the DC conductivity (d–f), Lyapunov (g–i) and *PR* (j–l) spectra possess almost the same band structure with their high-value zones located at the same energy regions. A further analysis of *PR* for $n=2$ and $n=3$ reveals their practical constant values when the hopping integral t_A decreases, contrary to the decay behavior in *PR*

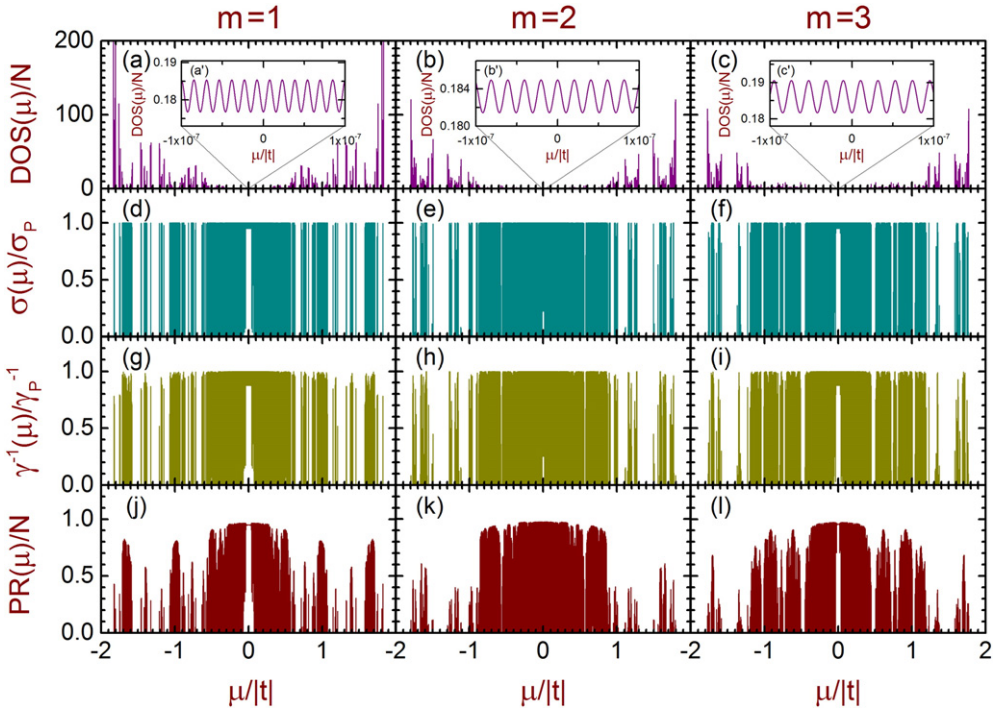

Fig. 3. Density of states (*DOS*), DC conductivity (σ), Lyapunov coefficient (γ) and participation ratio (*PR*) as functions of the chemical potential (μ) for three generalized Fibonacci chains with $n=2$, null self-energies, hopping integrals of $t_A=0.8t$ and $t_B=t$.

spectra of Fig. 2. This fact confirms the presence of almost extended states around $\mu=0$ in the (1,2) copper-mean lattice reported in reference [16].

In order to analyze the global behavior of DC conductivity (σ) and participation ratio (PR) spectra, we introduce the spectral averages of σ and of PR defined as

$$\langle\sigma\rangle = \frac{\int_{-\infty}^{\infty}\sigma(\mu)DOS(\mu)d\mu}{\int_{-\infty}^{\infty}DOS(\mu)d\mu} \quad \text{and} \quad \langle PR\rangle = \frac{\int_{-\infty}^{\infty}PR(\mu)DOS(\mu)d\mu}{\int_{-\infty}^{\infty}DOS(\mu)d\mu}. \tag{27}$$

The results of $\langle\sigma\rangle$ as functions of the system length (N) are shown in Fig. 5(a–i) for the nine GF chains of Fig. 1 with hopping integrals $t_A=t_B$ (dark yellow circles), $t_A=0.99\,t_B$ (red hexagons), $t_A=0.95\,t_B$ (blue pentagons), $t_A=0.9\,t_B$ (orange down triangles), $t_A=0.85\,t_B$ (green squares) and $t_A=0.8\,t_B$ (magenta up triangles). The imaginary part of the energy was $\eta=10^{-13}\,|t|$ for σ and $\eta=10^{-5}\,|t|$ for DOS. Observe that when the system length grows, $\langle\sigma\rangle$ is a constant for the periodic case and it decays following a power law for quasiperiodic systems with $n=1$ and it is truly archived when the system size is large enough. For other six GF systems that do not fulfill the Pisot quasiperiodic criteria, the average conductivity decay more slowly than the quasiperiodic systems, neither a constant as in periodic ones.

In Fig. 6, the spectral average of participation ratio ($\langle PR\rangle$) is plotted as functions of the number of atoms (N) in the nine GF chains of Fig. 1. The numerical calculations of $\langle PR\rangle$ were carried out by using a new renormalization method developed for the participation ratio of GF chains and presented in Appendix B. The parameters used in these calculations are the same as in Fig. 5. Observe that the $\langle PR\rangle$ results confirm the power-law and sub-power-law behaviors of $\langle\sigma\rangle$, respectively for quasiperiodic and non-quasiperiodic systems, obtained from the Kubo-Greenwood formula.

In order to perform an analytical and comparative study of PR at $\mu=0$ for (1,2)- and (2,1)-type GF chains, let us introduce the notation $PR(m,n,l)$ for a (m,n)-type GF chain of generation l evaluated at $\mu=0$, where the transfer matrices of Eq. (12) can be

$$\begin{pmatrix}0 & -\chi\\ 1 & 0\end{pmatrix},\ \begin{pmatrix}0 & -\chi^{-1}\\ 1 & 0\end{pmatrix} \text{ or } \begin{pmatrix}0 & -1\\ 1 & 0\end{pmatrix}, \tag{28}$$

with $\chi=t_A/t_B$. Hence, the normalized PR for a (2,1)-type GF chain of generation $l=2k+1$ with N_l atoms is given by

$$PR(2,1,2k+1) = \frac{\left[\sum_{j=-k}^{k-1}\Lambda_j(l)\chi^{2j}\right]^2}{N_l\sum_{j=-k}^{k-1}\Lambda_j(l)\chi^{4j}}, \tag{29}$$

where $\Lambda_j(2k+1)=2\Lambda_j(2k)+\Lambda_j(2k-1)-2\delta_{j,0}$ and $\Lambda_{-k}(l)=\frac{1}{2}[3-(-1)^l]$. At the limit of $\chi\to0$ and $l\to\infty$, we have

$$\lim_{\substack{l\to\infty\\ \chi\to0}} PR(2,1,2k+1) = \lim_{l\to\infty}\frac{\Lambda_{-k}(l)}{N_l} = 0. \tag{30}$$

In contrast, the (1,2)-type GF chain has

$$PR(1,2,l) = \frac{\left[\Theta_{-1}(l)\chi^{-2}+\Theta_0(l)+\Theta_1(l)\chi^2\right]^2}{N_l\left[\Theta_{-1}(l)\chi^{-4}+\Theta_0(l)+\Theta_1(l)\chi^4\right]}, \tag{31}$$

whose coefficients Θ_{-1},Θ_0,and Θ_1 are given in Table 3.

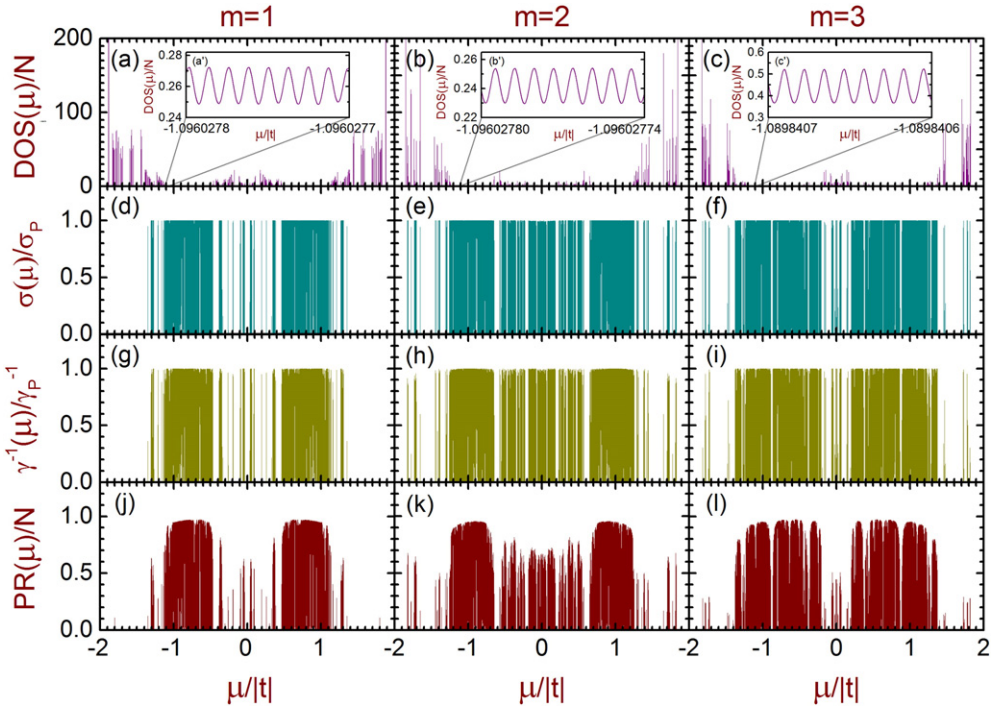

Fig. 4. Density of states (DOS), DC conductivity (σ), Lyapunov coefficient (γ) and participation ratio (PR) as functions of the chemical potential (μ) for three generalized Fibonacci chains with $n=3$, null self-energies, hopping integrals of $t_A=0.8\,t$ and $t_B=t$.

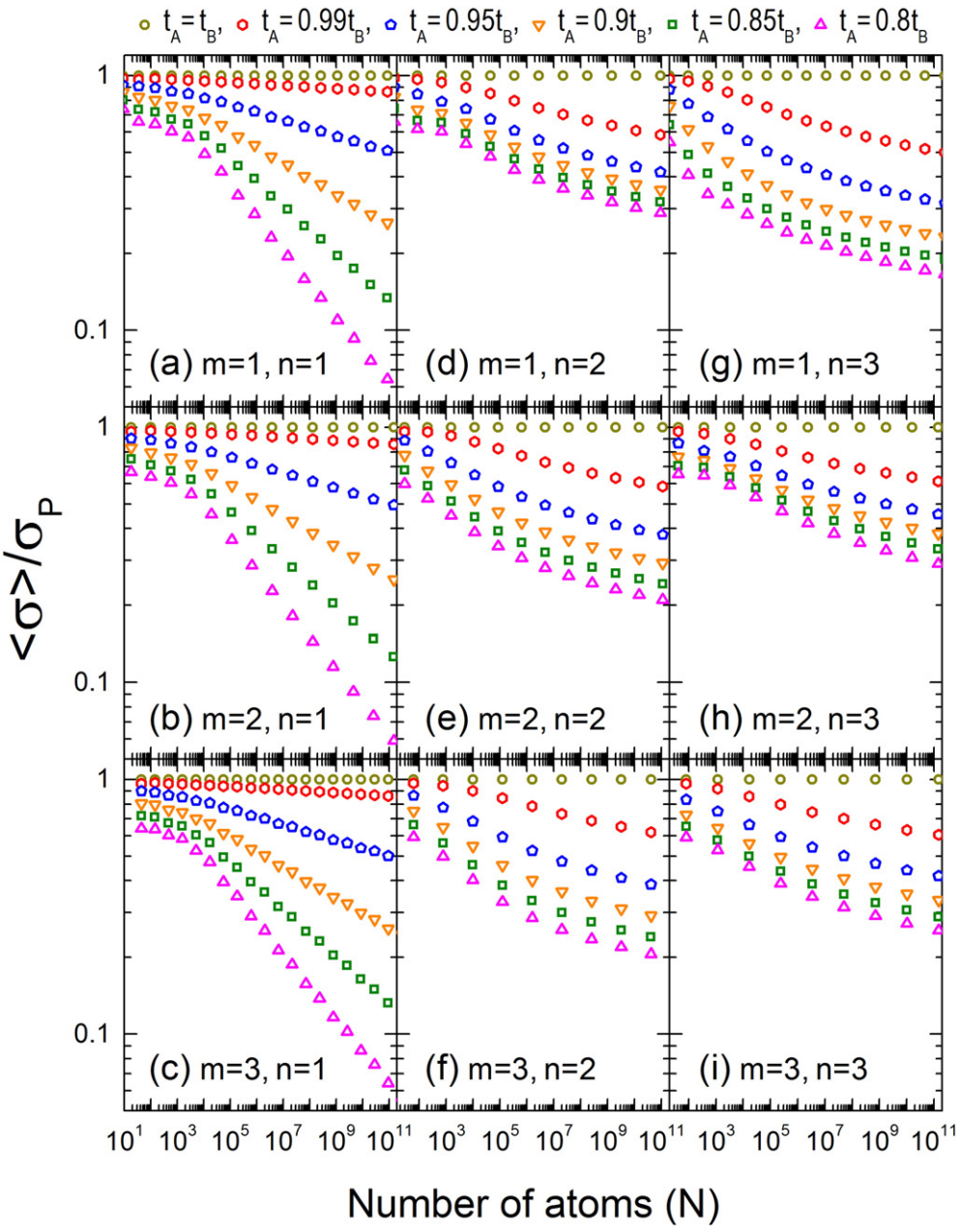

Fig. 5. Spectral average of DC conductivity ($\langle\sigma\rangle$) versus the number of atoms (N) for the nine generalized Fibonacci chains illustrated in Fig. 1 with hopping integrals $t_A = t_B$ (dark yellow solid circles), $t_A = 0.99t_B$ (red open hexagons), $t_A = 0.95t_B$ (blue open pentagons), $t_A = 0.9t_B$ (orange open down triangles), $t_A = 0.85t_B$ (green open squares) and $t_A = 0.8t_B$ (magenta open up triangles).

At the limit of $\chi \to 0$ and $l \to \infty$, Eq. (31) leads to

$$\lim_{\substack{l\to\infty \\ \chi\to 0}} PR(1,2,l) = \lim_{l\to\infty} \frac{\Theta_{-1}(l)}{N_l} = \lim_{l\to\infty} \frac{2N_{l-2} + N_{l-3} \mp 1}{N_l} = \frac{3}{8}, \tag{32}$$

because $N_l = N_{l-1} + 2N_{l-2} - 2$ and $\lim_{l\to\infty}(N_{l+1}/N_l) = 2$. The analytical results of Eqs. (30) and (32) confirm the numerical ones shown in Figs. 2 and 3.

5. AC conductivity

As observed in Figs. 2, 3 and 4, there are many peaks in DC conductivity (σ) spectra. If we choose a chemical potential (μ) located between two successive peaks and an external alternating electrical field with $\hbar\omega$ equal to the difference between their energies, a resonant AC electronic transport is registered in segmented [32] and branched nanowires [19]. In this section, we analyze such transport in GF chains. Fig. 7 shows AC conductivity spectra in color scale versus the chemical potential (μ) and the electrical field frequency (ω) for GF chains with $t_A = 0.8t$, $t_B = t$ (a) $m = 1$, $n = 1$ and $l = 14$; (b) $m = 2$, $n = 2$ and $l = 7$; (c) $m = 3$, $n = 3$ and $l = 5$. The calculations were performed by using an imaginary part of energy $\eta = 10^{-15}|t|$ and these GF chains are connected to two semi-infinite periodic leads with hopping integrals of t.

Observe in Fig. 7(a) a band structure at low frequency limit similar to that of Fig. 2(d). For several frequencies, red zones with an AC conductivity larger than the ballistic one $\sigma_P(\mu,\omega,0)$ of periodic chain given by Eq. (20) can be found. For example, in Fig. 7(a) there is a resonant peak of $\sigma(\mu,\omega,0) = 1.755\,\sigma_P$ (red bar) at $\hbar\omega = 0.06123246|t|$ for

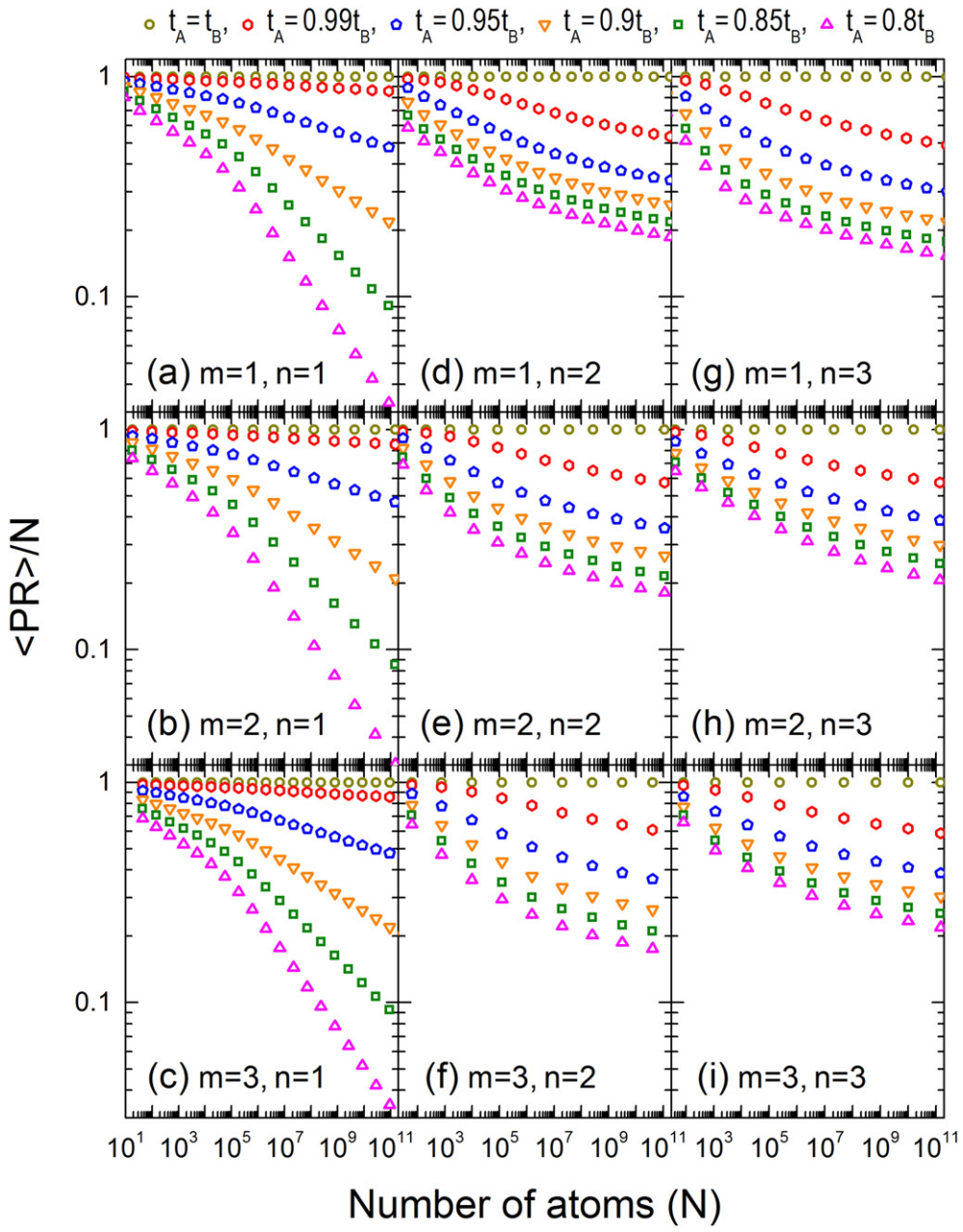

Fig. 6. Spectral average of participation ratio ($\langle PR \rangle$) versus the number of atoms (N) for the nine generalized Fibonacci chains illustrated in Fig. 1 with hopping integrals $t_A = t_B$ (dark yellow solid circles), $t_A = 0.99t_B$ (red open hexagons), $t_A = 0.95t_B$ (blue open pentagons), $t_A = 0.9t_B$ (orange open down triangles), $t_A = 0.85t_B$ (green open squares) and $t_A = 0.8t_B$ (magenta open up triangles).

$0.11738557|t| \le \mu \le 0.17861803|t|$, whose conductivity quickly decays with the diminution or the increase of frequency. Close to this red bar, there is another resonant peak of $\sigma(\mu, \omega, 0) = 0.384\sigma_P$ (green bar) at $\hbar\omega = 0.06745621|t|$ for $0.11400161|t| \le \mu \le 0.18145782|t|$. The first one is originated by an interband excitation between two high DC conduction states at $E = 0.11738557|t|$ and $E = 0.17861803|t|$ just located at the borders of a bandgap, while the second one is due to third neighbor peaks of high DC conductions located at $E = 0.11400161|t|$ and $E = 0.18145782|t|$. In fact, there are resonant AC conductions when $\hbar\omega$ is equal to the energy difference corresponding to DC conductivity peaks separated by an even number of peaks in the DC conductivity spectrum, as shown in Fig. 3 of Ref. [19]. Furthermore, notice in Fig. 7(b) and (c) the presence of color zones with AC conductivity $0.2\sigma_P \le \sigma(\mu, \omega, 0) \le 0.9\sigma_P$, caused by resonances between rounded peaks shown in Figs. 3(b′) and 4(c′) separated by an energy of the order of $|t|/N$, in contrast to sharp peaks in Fig. 2(a′) leading to well defined resonant frequencies in Fig. 7(a). In general, high resonant AC conductivities have been found at the extremes of bands.

Table 3
Coefficients Θ_i of term χ^i in Eq. (31) for (1,2)-type GF chains.

$m=1, n=2$	l even	l odd
$\Theta_{-1}(l)$	$2N_{l-2} - N_{l-3} - 1$	$2N_{l-2} - N_{l-3} + 1$
$\Theta_0(l)$	$N_{l-1} - 1$	$N_{l-1} - 2$
$\Theta_1(l)$	N_{l-3}	$N_{l-3} - 1$

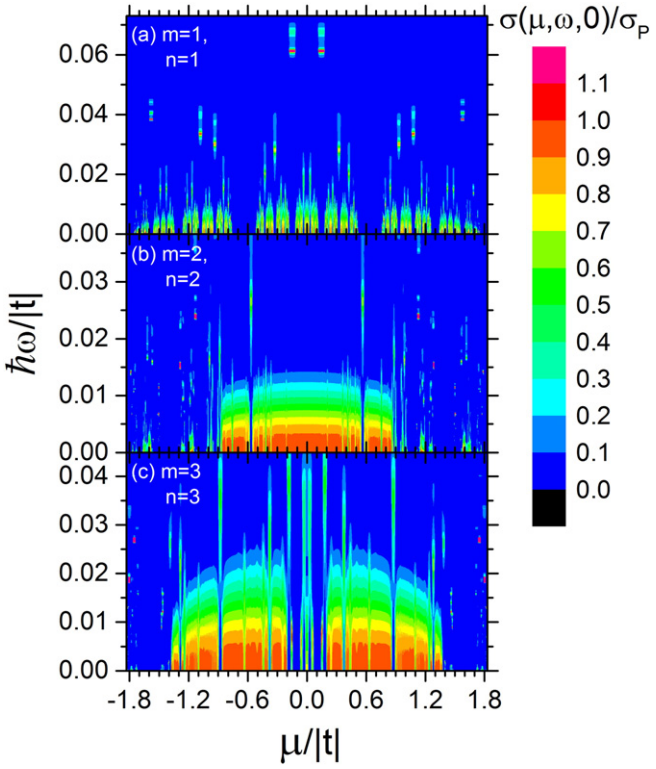

Fig. 7. AC conductivity spectra (in color scale) versus chemical potential (μ) and frequency (ω) for generalized Fibonacci chains with (a) $m=1, n=1$ and $l=14$, (b) $m=2, n=2$ and $l=7$, (c) $m=3, n=3$ and $l=5$.

In order to compare the global resonant AC conduction capability in different GF chains, we introduce a spectral average conductivity defined as

$$<\sigma(\mu,\omega,0)> = \frac{1}{N_{pk}-1}\sum_{j=1}^{N_{pk}-1}\sigma(\mu_j,\omega_j,0), \tag{33}$$

where N_{pk} is the total number of peaks in the DC conductivity spectrum, $\mu_j=(E_{j+1}+E_j)/2$ and $\omega_j=(E_{j+1}-E_j)/\hbar$ are respectively the central energy and the resonant frequency of two successive DC conductivity peaks with energies of E_j and E_{j+1}. Fig. 8 show $<\sigma(\mu,\omega,0)>$ (open circles) versus the number of atoms (N) in nine GF chains, where the error bars illustrate the maximum and minimum values of AC conductivities in each generation (l). Observe that $\langle\sigma(\mu,\omega,0)\rangle$ grows with the number of atoms and the maximum AC conductivity can reach to 10^{10} times the ballistic DC conductivity (σ_P) for non-quasiperiodic GF chains of 10^5 atoms. In fact, the zero-temperature ballistic AC conductivity $\sigma_P(\mu,\omega,0)$ of periodic chains is bounded by σ_P. Overall, the truly high AC conductivities were obtained from the resonance of very sharp DC conductivity peaks.

6. Generalized Fibonacci nanowires

The electronic transport in aperiodic nanowires with finite cross-section can be studied by using the renormalization plus convolution method for the Kubo-Greenwood formula and its electrical conductivity (σ) is expressed as [30]

$$\sigma(\mu,\omega,T) = \frac{1}{\Omega_\perp}\sum_\beta \sigma^{\parallel}(\mu-E_\beta,\omega,T), \tag{34}$$

where $\sigma^{\parallel}$ is the electrical conductivity of the parallel subsystem, $\Omega_\perp$ and E_β are respectively the volume and the eigenenergies of the

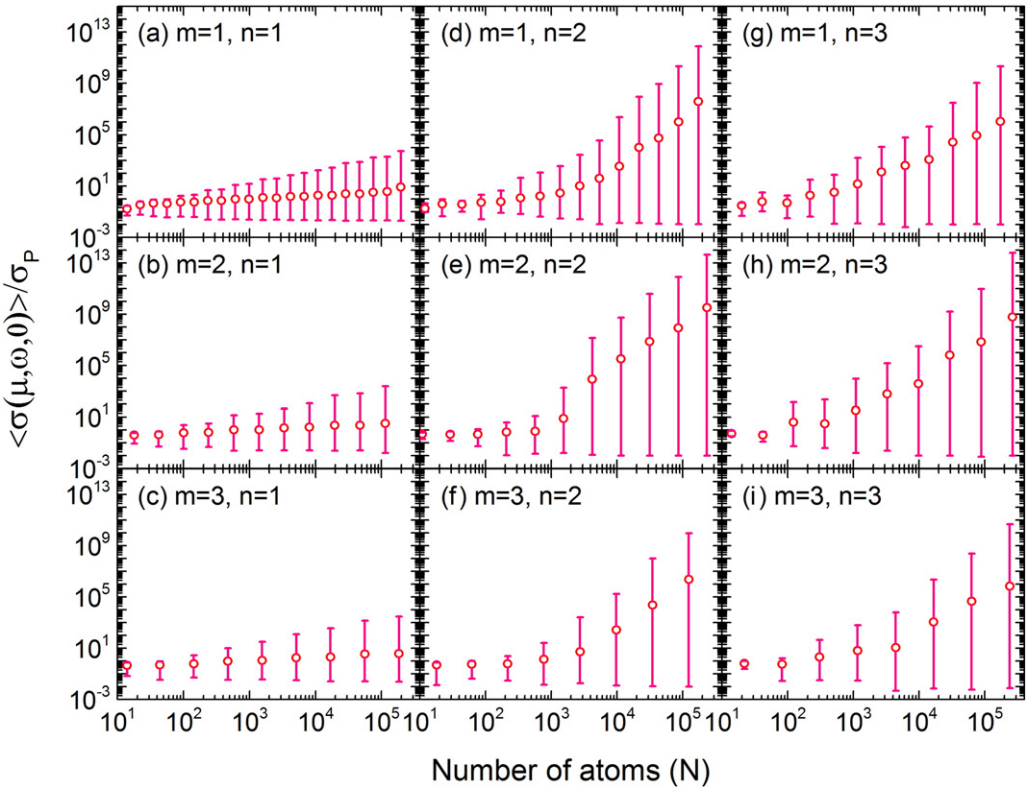

Fig. 8. Spectral averages of zero-temperature AC conductivity $\langle\sigma(\mu,\omega,0)\rangle$ (open circles) versus the number of atoms (N) for nine generalized Fibonacci chains of type (m,n), where the error bars indicate the maximum and minimum AC conductivity values.

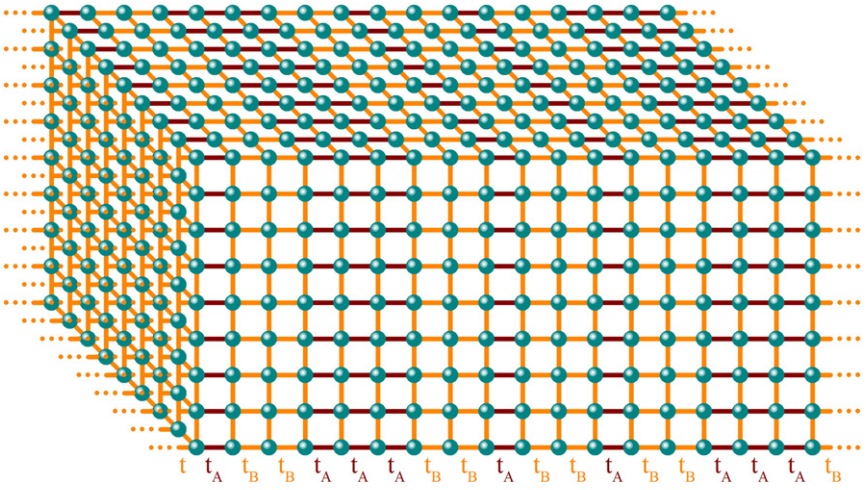

Fig. 9. Sketch of a segment of a nanowire with a periodic cross section of 9×9 atoms, whose hopping integrals t_A and t_B along the longitudinal direction follow the copper-mean sequence.

perpendicular subsystem. The electrical conductance is written as $g(\mu,\omega,T)\equiv\sigma(\mu,\omega,T)\Omega_\perp/\Omega_\parallel$, where $\Omega_\parallel$ is the length of the nanowire. For example, a nanowire with a periodic cross section of 9×9 atoms is shown in Fig. 9, whose hopping integrals t_A and t_B along the longitudinal direction of nanowire are ordered following the copper-mean sequence with $m=1$ and $n=2$.

The zero-temperature DC conductance (g) as a function of the chemical potential (μ) is presented in Fig. 10 for nine GF nanowires with cross sections of 9 × 9 atoms (see Fig. 9), whose longitudinal arrangements of hopping integrals follow the sequences shown in Fig. 1. The lengths of these nanowires are specified in Table 2 and the Hamiltonian parameters are $t_A=0.8\,t$, $t_B=t$ and null self-energies. The imaginary part of the energy is $\eta=10^{-15}|t|$ and Fig. 10 are plotted by using a grid of 120,000 chemical potentials. The conductance g spectra, normalized by the quantum of conductance $g_0\equiv 2e^2/h$, of GF nanowires are compared to that of a periodic nanowire with the same cross section (light grey lines). Observe its quantized conductance, in which the step height in unity of g_0 at $\pm(|E_\beta|+2|t|)$ is the degeneracy of E_β. In particular, the maximum step height is $9g_0$ located at $\mu=\pm 2|t|$, since the cross section is of 9 × 9 atoms. Moreover, the integral $\int_{-\infty}^{\infty} g(\mu,0,0)d\mu$ of this stepped spectrum is $324g_0|t|$, because each of the 81 ballistic conducting channels provides a constant area of $4g_0|t|$ wherever it is placed. When the arrangement of hopping integrals follows a quasiperiodic sequence along the longitudinal direction, the conductance is significantly smaller than the periodic case. In general, the non-quasiperiodic nanowires with $n>1$ have larger electrical conductance

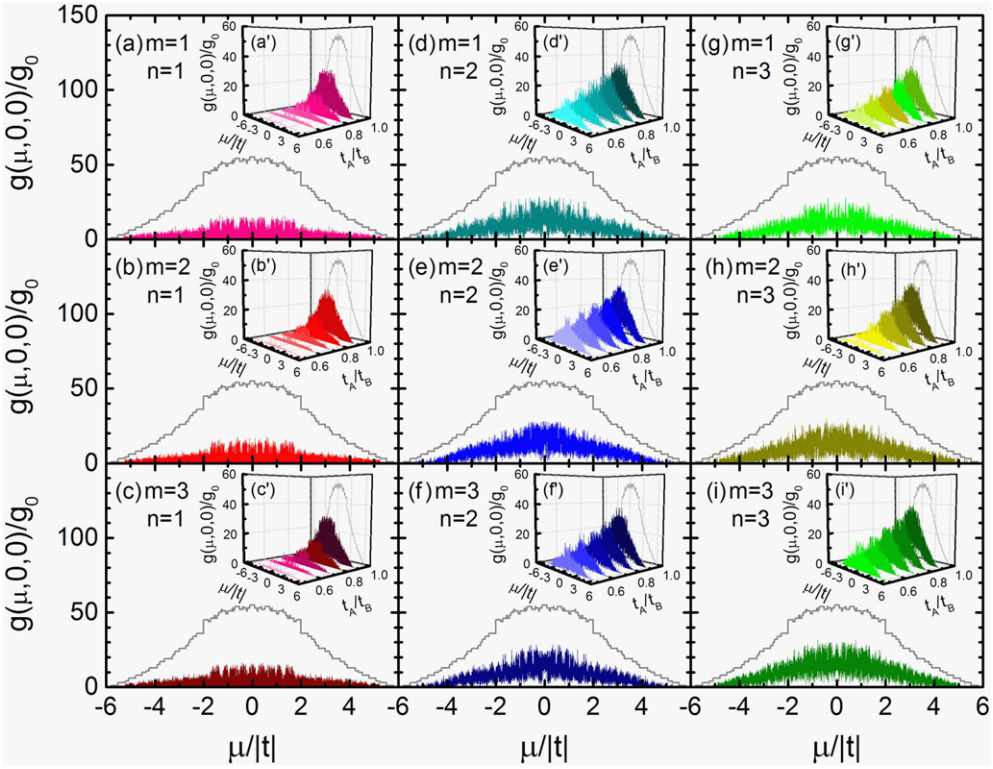

Fig. 10. Zero-temperature electrical conductance (g) versus the chemical potential (μ) for nine GF nanowires of type (m,n) with cross sections of 9×9 atoms, $t_A=0.8\,t$, $t_B=t$, null self-energies, whose longitudinal arrangements of hopping integrals follow the sequences of Fig. 1. These spectra are compared to that of a periodic nanowire with the same cross section (light gray lines). Insets: Corresponding conductance spectra for $t_A/t_B=0.5$, 0.6, 0.7, 0.8, 0.9 and 1.0.

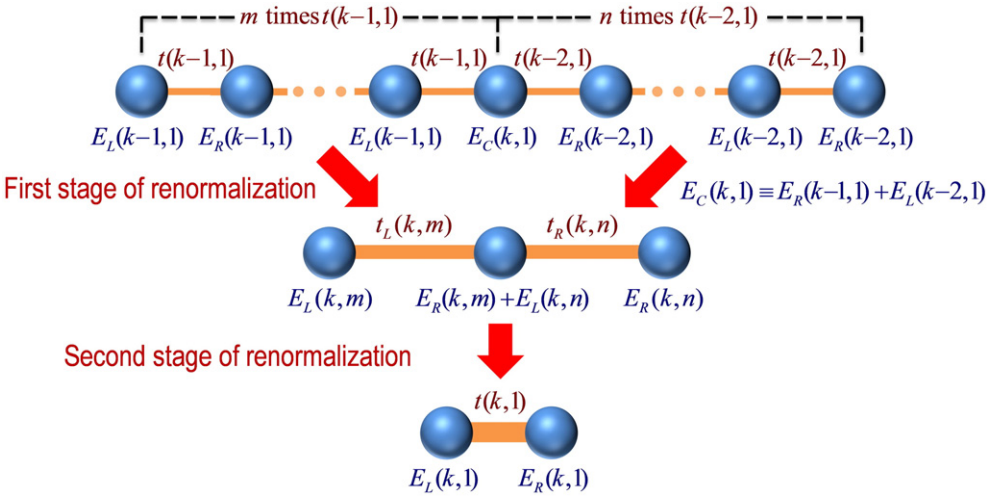

Fig. A1. Schematic representation of the two-stage renormalization procedure for generalized Fibonacci chains of type (m,n).

than those of quasiperiodic ones with $n=1$, in consistence with the single-channel spectral-average results of Fig. 5. In fact, they have large intervals of μ with $g(\mu,0,0)>0$, in contrast to the almost zero minimum value of g over whole spectra for quasiperiodic nanowires, which could be related to the eigenvalue spectra supported on Cantor sets of Lebesgue measure zero for quasiperiodic chains with site disorder [33]. Finally, the insets of Fig. 10 show the evolution of electrical conductance spectra when the bond disorder amplitude of GF nanowires grows. Observe the rapid vanish of conductance spectra of quasiperiodic nanowires in comparison to the non-quasiperiodic ones.

7. Conclusions

To quantify the localization of wavefunctions in macroscopic generalized Fibonacci (GF) systems, we have developed a new real-space renormalization method for the participation ratio (*PR*). Also, we have extended the renormalization method previously developed for the Kubo-Greenwood formula in Fibonacci lattices [30] with $n=m=1$ to all (m,n)-type GF ones. In general, these renormalization methods have the advantage of being computationally efficient without introducing additional approximations and representing a useful alternative for the study of non-periodic systems, where the reciprocal space is absent or useless.

The *PR* has been one of the most used quantities for the study of wavefunction localization in disordered systems and the results of this article reveal its deficiency in quasiperiodic lattices. In particular, we found a transparent state at $\mu=0$ in (2,1)-type GF chains for any even number of generation [34] and $\chi=t_A/t_B>0$. However, the corresponding *PR* has a limiting value of zero, as demonstrated in Eq. (30). In other words, an extremely localized electronic state with almost zero *PR* could possess a ballistic transport. In general, the results confirm the close relation, with the possible exception of critically localized states [9], between the wavefunction localization and the electronic transport at zero temperature. For example, the close resemblance between DC conductivity spectra and Lyapunov exponent ones. In particular, they are self-similar for the GF chains with $n=1$, in accordance to their purely singular continuous spectra established for the site problem [33]. This fact leads to a power-law decay of the spectral averages of both DC conductivity and *PR* when the number of atoms increases. In contrast, GF chains with $n=2$ and $n=3$ present zones with high-conduction oscillating behavior, which gives rise a slow decay of these spectral averages. In addition, we found an analytical expression of Lyapunov exponent for periodic lattices.

Finally, we report the first global analysis of AC conduction over entire spectra of GF chains. The results show extremely high resonant AC conductivity peaks in comparison to the ballistic AC one, whose average value grows faster in non-quasiperiodic systems than quasiperiodic ones. In general, partially localized electronic states could favor the interaction with external oscillating electric fields through local electric dipoles, inducing a larger AC response than a homogeneous charge distribution in periodic systems. Hence, the spatial localization of states determines their resonance intensity via the Fermi's golden rule, from which the Kubo-Greenwood formula can be obtained [26]. This study of the correlation between wavefunction localization and electronic transport can be extended to multidimensional systems, as partially done in Section VI for the DC conductivity of GF nanowires by using the convolution theorem.

Table A1
Significance of symbols in Eq. (A.2).

Stage	α	β	ε	δ	λ	ξ	ζ
First	L	L	F	$j-1$	j	$k-1$	1
	R	R				$k-2$	
Second	F	L	R	m	1	k	n

Acknowledgements

We would like to acknowledge Dr. Carlos Ramirez for the useful discussions. This work has been partially supported by CONACyT-252943 and by UNAM-DGAPA-PAPIIT through IN113714 and IN114916. Computations were performed at Miztli of DGTIC-UNAM.

Appendix A. Renormalization formulas for the density of states

For a generalized Fibonacci (GF) chain of type (m,n) with two kinds of bonds, t_A and t_B, the density of states (*DOS*) of generation l evaluated at energy E in terms of the Green's function (G) can be written as in Ref. [30],

$$\begin{aligned} DOS(E,l) &= -\frac{1}{\pi}\lim_{\eta\to 0^+}\mathrm{Im}\sum_{j=1}^{N(l)}G_{j,j}(z) \\ &= -\frac{1}{\pi}\lim_{\eta\to 0^+}\mathrm{Im}[A_F(l,1)G_{L,L}(z)+B_F(l,1)G_{R,R}(z) \\ &\quad +C_F(l,1)G_{L,R}(z)+D_F(l,1)] \end{aligned} \tag{A.1}$$

where $z=E+i\eta$, $N(l)$ is the total number of atoms in a GF chain of generation l, and the coefficients A, B, C and D are iteratively calculated by

means of a two-stage renormalization procedure, as schematically summarized in Fig. A1, through

$$\begin{cases} A_\alpha(k,\lambda) = A_\beta(k,\delta) + \theta_\alpha^2(k,\lambda)[A_\varepsilon(\xi,\zeta) \\ \quad +B_\beta(k,\delta)-1] + \theta_\alpha(k,\lambda)C_\beta(k,\delta) \\ B_\alpha(k,\lambda) = B_\varepsilon(\xi,\zeta) + \phi_\alpha^2(k,\lambda)[A_\varepsilon(\xi,\zeta) \\ \quad +B_\beta(k,\delta)-1] + \phi_\alpha(k,\lambda)C_\varepsilon(\xi,\zeta) \\ C_\alpha(k,\lambda) = \phi_\alpha(k,\lambda)C_\beta(k,\delta) + \theta_\alpha(k,\lambda)C_\varepsilon(\xi,\zeta) \\ \quad +2\theta_\alpha(k,\lambda)\phi_\alpha(k,\lambda)\left[A_\varepsilon(\xi,\zeta) + B_\beta(k,\delta)-1\right] \\ D_\alpha(k,\lambda) = D_\beta(k,\delta) + D_\varepsilon(\xi,\zeta) + [A_\varepsilon(\xi,\zeta) \\ \quad +B_\beta(k,\delta)-1]/[z-E_R(k,\delta)-E_L(\xi,\zeta)] \end{cases}, \tag{A.2}$$

where

$$\begin{cases} \theta_\alpha(k,\lambda) = t_\beta(k,\delta)/[z-E_R(k,\delta)-E_L(\xi,\zeta)] \\ \phi_\alpha(k,\lambda) = t_\varepsilon(\xi,\zeta)/[z-E_R(k,\delta)-E_L(\xi,\zeta)] \\ E_L(k,\lambda) = E_L(k,\delta) + t_\beta^2(k,\delta)/[z-E_R(k,\delta) \\ \quad -E_L(\xi,\zeta)] \\ E_R(k,\lambda) = E_\varepsilon(\xi,\zeta) + t_\varepsilon^2(\xi,\zeta)/[z-E_R(k,\delta) \\ \quad -E_L(\xi,\zeta)] \\ t_\alpha(k,\lambda) = t_\beta(k,\delta)t_\varepsilon(\xi,\zeta)/[z-E_R(k,\delta) \\ \quad -E_L(\xi,\zeta)] \end{cases} \tag{A.3}$$

and the significance of $\alpha,\beta,\varepsilon,\delta,\lambda,\xi$ and ζ are given in Table A1, where in each row the value of α determines the meaning of the subsequent parameters.

For a GF chain of generation k, the renormalization procedure consists of using the same Eqs. (A.2)–(A.3) and following the steps: (1) iteratively calculating the coefficients $A_L(k-1,j)$, $B_L(k-1,j)$, $C_L(k-1,j)$ and $D_L(k-1,j)$ for $j=2,\ 3,\cdots,\ m$; (2) iteratively computing $A_R(k-2,j)$, $B_R(k-2,j)$, $C_R(k-2,j)$ and $D_R(k-2,j)$ for $j=2,\ 3,\cdots,\ n$; and (3) using the results of left- and right-segment renormalizations to calculate $A_F(k,1)$, $B_F(k,1)$, $C_F(k,1)$ and $D_F(k,1)$ of generation k. This calculation should be repeated for $k=2,\ 3,\ \cdots,\ l$ in order to finally determine the *DOS* of a GF chain of type (m,n) and generation l.

The initial conditions for Eqs. (A.2)–(A.3) are $t_F(0,1)=t_B$, $A_F(0,1)=B_F(0,1)=1$, $C_F(0,1)=D_F(0,1)=0$, $E_L(0,1)=E_R(0,1)=0$, $A_F(1,1)=B_F(1,1)=1$, $C_F(1,1)=D_F(1,1)=0$, $t_F(1,1)=t_A$, and $E_L(1,1)=E_R(1,1)=0$.

When the system is connected to two periodic leads, the Green's functions at its extreme atoms are given by

$$G_{L,L}(z) = \left\{ z-E_L(l,1)-E_P^R(l')-\frac{t_P^2(l')}{z-E_P^L(l')} - \frac{t_F^2(l,1)}{z-E_R(l,1)-E_P^L(l')-t_P^2(l')/\left[z-E_P^R(l')\right]} \right\}^{-1}, \tag{A.4}$$

$$G_{R,R}(z) = \left\{ z-E_R(l,1)-E_P^L(l')-\frac{t_P^2(l')}{z-E_P^R(l')} - \frac{t_F^2(l,1)}{z-E_L(l,1)-E_P^R(l')-t_P^2(l')/\left[z-E_P^L(l')\right]} \right\}^{-1}, \tag{A.5}$$

and

$$G_{L,R}(z) = \frac{t_F(l,1)G_{R,R}(z)}{z-E_L(l,1)-E_P^R(l')-t_P^2(l')/\left[z-E_P^L(l')\right]}, \tag{A.6}$$

where l' is the generation number of these periodic leads built following the GF renormalization procedure with $m=n=1$ and $t_A=t_B=t$, whose effective self-energies and hopping-integrals are $E_P^L(l')=E_P^L(l'-1)+t_P^2(l'-1)\gamma_P$, $E_P^R(l')=E_P^R(l'-2)+t_P^2(l'-2)\gamma_P$, and $t_P(l')=t_P(l'-1)\,t_P(l'-2)\gamma_P$, being $\gamma_P=[z-E_P^R(l'-1)-E_P^L(l'-2)]^{-1}$.

In order to illustrate the procedure for obtaining the renormalization formulas, we may take the middle state of Fig. A1 as the initial system, whose *DOS* can be written from Eq. (A.1) as

$$DOS(E,l) = -\frac{1}{\pi}\lim_{\eta\to 0^+}\mathrm{Im}\begin{bmatrix} \sum_{j=1}^{mN(l-1)}G_{j,j}(z) \\ +\sum_{j=mN(l-1)}^{N(l)}G_{j,j}(z) \\ -G_{C,C}(z) \end{bmatrix} \tag{A.7}$$

$$= -\frac{1}{\pi}\lim_{\eta\to 0^+}\mathrm{Im}\begin{bmatrix} A_L(l,m)G_{L,L}(z) + B_L(l,m)G_{C,C}(z) \\ +C_L(l,m)G_{L,C}(z) + D_L(l,m)+ \\ A_R(l,n)G_{C,C}(z) + B_R(l,n)G_{R,R}(z) \\ +C_R(l,n)G_{C,R}(z) \\ +D_R(l,n)-G_{C,C}(z) \end{bmatrix},$$

where the Green's function elements satisfy the Dyson's equation given by

$$\begin{pmatrix} z-E_L(l,m) & -t_L(l,m) & 0 \\ -t_L(l,m) & z-E_C(l,1) & -t_R(l,n) \\ 0 & -t_R(l,n) & z-E_R(l,n) \end{pmatrix}\times \begin{pmatrix} G_{L,L}(z) & G_{L,C}(z) & G_{L,R}(z) \\ G_{C,L}(z) & G_{C,C}(z) & G_{C,R}(z) \\ G_{R,L}(z) & G_{R,C}(z) & G_{R,R}(z) \end{pmatrix} = \begin{pmatrix} 1 & 0 & 0 \\ 0 & 1 & 0 \\ 0 & 0 & 1 \end{pmatrix}. \tag{A.8}$$

In other words,

$$G_{C,X}(z) = \frac{\delta_{C,X}}{z-E_C(l,1)} + \frac{t_L(l,m)}{z-E_C(l,1)}G_{L,X}(z) + \frac{t_R(l,n)}{z-E_C(l,1)}G_{R,X}(z), \tag{A.9}$$

where $X=L,C$, or R, and $E_C(l,1)=E_R(l,m)+E_L(l,n)$. Taking the advantage of being the Green's function a symmetric matrix derived from a symmetric Hamiltonian, Eq. (A.9) for $X=C$ can be rewritten by using the same equation for $X=L$ and $X=R$ as

$$G_{C,C}(z) = [z-E_C(l,1)]^{-1} + \theta_F^2(l,1)G_{L,L}(z) + \phi_F^2(l,1)G_{R,R}(z) + 2\theta_F(l,1)\phi_F(l,1)G_{L,R}(z). \tag{A.10}$$

Substituting Eqs. (A.9)–(A.10) into Eq.(A.7), one obtains

$$\begin{aligned} DOS(E,l) = -\frac{1}{\pi}\lim_{\eta\to 0^+}\mathrm{Im}\{&A_L(l,m)G_{L,L}(z) \\ &+D_L(l,m) + D_R(l,n) + B_R(l,n)G_{R,R}(z) \\ &+C_L(l,m)\left[\theta_F(l,1)G_{L,L}(z) + \phi_F(l,1)G_{R,L}(z)\right] \\ &+C_R(l,n)\left[\theta_F(l,1)G_{L,R}(z) + \phi_F(l,1)G_{R,R}(z)\right] \\ &+[B_L(l,m) + A_R(l,n)-1][\theta_F^2(l,1)G_{L,L}(z) \\ &+\phi_F^2(l,1)G_{R,R}(z) + 2\theta_F(l,1)\phi_F(l,1)G_{L,R}(z) \\ &+[z-E_C(l,1)]^{-1}]\}, \end{aligned} \tag{A.11}$$

which leads to Eq. (A.2). On the other hand, substituting Eqs. (A.9) into Eq. (A.8), it becomes to

$$\begin{pmatrix} z-E_L(l,1) & -t_F(l,1) \\ -t_F(l,1) & z-E_R(l,1) \end{pmatrix}\times \begin{pmatrix} G_{L,L}(z) & G_{L,R}(z) \\ G_{R,L}(z) & G_{R,R}(z) \end{pmatrix} = \begin{pmatrix} 1 & 0 \\ 0 & 1 \end{pmatrix}, \tag{A.12}$$

where the renormalized hopping integral $t_F(l,1)$ and self-energies, $E_L(l,1)$ and $E_R(l,1)$, are given in Eq. (A.3).

Appendix B. Renormalization formulas for the participation ratio

Since the single-electron wavefunction ($|\Psi\rangle$) can be written as a linear combination of the Wannier's function ($|j\rangle$) of atom j, $|\Psi\rangle = \sum_j c_j|j\rangle$, the participation ratio (PR) for a non-normalized wavefunction is given by

$$PR = \frac{\left(\sum_j |c_j|^2\right)^2}{\sum_j |c_j|^4} \tag{B.1}$$

and its denominator may be expressed in term of the wavefunction amplitudes at extreme sites, c_L and c_R, as

$$\begin{aligned}\textstyle\sum_j |c_j|^4 = {} & I_F(l,1)|c_L|^4 + L_F(l,1)\left[c_L^2 c_R^{*2} + c_R^2 c_L^{*2}\right] \\ & + J_F(l,1)|c_R|^4 + P_F(l,1)|c_L|^2\left(c_L c_R^* + c_R c_L^*\right) + \\ & K_F(l,1)|c_L|^2|c_R|^2 + Q_F(l,1)|c_R|^2\left(c_L c_R^* + c_R c_L^*\right),\end{aligned} \tag{B.2}$$

where $I_F(l,1)$, $J_F(l,1)$, $K_F(l,1)$, $L_F(l,1)$, $P_F(l,1)$ and $Q_F(l,1)$ are the renormalization coefficients for PR. Analogously, the normalization condition of wavefunction $|\Psi\rangle$ can also be expressed as

$$\begin{aligned}1 = \sum_j |c_j|^2 = {} & R_F(l,1)|c_L|^2 + S_F(l,1)|c_R|^2 \\ & + U_F(l,1)[c_L c_R^* + c_R c_L^*].\end{aligned} \tag{B.3}$$

Following a similar renormalization procedure for the DOS explained at the end of Appendix A, by using the Schrödinger equation instead of the Dyson one, the renormalization coefficients for PR of a (m,n)-type GF chain of generation l can be iteratively calculated for $k = 2, 3, \cdots, l$ by means of

$$\begin{aligned}I_\alpha(k,\lambda) = {} & \theta_\alpha^3(k,\lambda)\Big\{\theta_\alpha(k,\lambda)\Big[J_\beta(k,\delta) + I_\varepsilon(\xi,\zeta) - 1\Big] \\ & + 2Q_\beta(k,\delta)\Big\} + I_\beta(k,\delta) + 2\theta_\alpha(k,\lambda)P_\beta(k,\delta) \\ & + \theta_\alpha^2(k,\lambda)\left[K_\beta(k,\delta) + 2L_\beta(k,\delta)\right],\end{aligned} \tag{B.4}$$

$$\begin{aligned}J_\alpha(k,\lambda) = {} & \phi_\alpha^3(k,\lambda)\Big\{\phi_\alpha(k,\lambda)\Big[J_\beta(k,\delta) + I_\varepsilon(\xi,\zeta) - 1\Big] \\ & + 2P_\varepsilon(\xi,\zeta)\Big\} + J_\varepsilon(\xi,\zeta) + 2\phi_\alpha(k,\lambda)Q_\varepsilon(\xi,\zeta) \\ & + \phi_\alpha^2(k,\lambda)[K_\varepsilon(\xi,\zeta) + 2L_\varepsilon(\xi,\zeta)],\end{aligned} \tag{B.5}$$

$$\begin{aligned}K_\alpha(k,\lambda) = {} & \theta_\alpha^2(k,\lambda)\Big\{4\phi_\alpha^2(k,\lambda)\Big[J_\beta(k,\delta) + I_\varepsilon(\xi,\zeta) - 1\Big] \\ & + K_\varepsilon(\xi,\zeta) + 4\phi_\alpha(k,\lambda)P_\varepsilon(\xi,\zeta)\Big\} \\ & + \phi_\alpha^2(k,\lambda)\left[K_\beta(k,\delta) + 4\theta_\alpha(k,\lambda)Q_\beta(k,\delta)\right],\end{aligned} \tag{B.6}$$

$$\begin{aligned}L_\alpha(k,\lambda) = {} & \theta_\alpha^2(k,\lambda)\Big\{\phi_\alpha^2(k,\lambda)\Big[J_\beta(k,\delta) + I_\varepsilon(\xi,\zeta) - 1\Big] \\ & + L_\varepsilon(\xi,\zeta) + \phi_\alpha(k,\lambda)P_\varepsilon(\xi,\zeta)\Big\} \\ & + \phi_\alpha^2(k,\lambda)\left[L_\beta(k,\delta) + \theta_\alpha(k,\lambda)Q_\beta(k,\delta)\right],\end{aligned} \tag{B.7}$$

$$\begin{aligned}P_\alpha(k,\lambda) = {} & \theta_\alpha^3(k,\lambda)\Big\{2\phi_\alpha(k,\lambda)\Big[J_\beta(k,\delta) + I_\varepsilon(\xi,\zeta) - 1\Big] \\ & + P_\varepsilon(\xi,\zeta)\Big\} + \theta_\alpha(k,\lambda)\phi_\alpha(k,\lambda)\{[K_\beta(k,\delta) + \\ & 2L_\beta(k,\delta)] + 3\theta_\alpha(k,\lambda)Q_\beta(k,\delta)\Big\} + \phi_\alpha(k,\lambda)P_\beta(k,\delta),\end{aligned} \tag{B.8}$$

$$\begin{aligned}Q_\alpha(k,\lambda) = {} & \phi_\alpha^3(k,\lambda)\Big\{2\theta_\alpha(k,\lambda)\Big[J_\beta(k,\delta) + I_\varepsilon(\xi,\zeta) - 1\Big] \\ & + Q_\beta(k,\delta)\Big\} + \theta_\alpha(k,\lambda)\phi_\alpha(k,\lambda)\{[K_\varepsilon(\xi,\zeta) + \\ & 2L_\varepsilon(\xi,\zeta)] + 3\phi_\alpha(k,\lambda)P_\varepsilon(\xi,\zeta)\Big\} + \theta_\alpha(k,\lambda)Q_\varepsilon(\xi,\zeta),\end{aligned} \tag{B.9}$$

$$\begin{aligned}R_\alpha(k,\lambda) = {} & \theta_\alpha^2(k,\lambda)\left[S_\beta(k,\delta) + R_\varepsilon(\xi,\zeta) - 1\right] \\ & + R_\beta(k,\delta) + 2\theta_\alpha(k,\lambda)U_\beta(k,\delta),\end{aligned} \tag{B.10}$$

$$\begin{aligned}S_\alpha(k,\lambda) = {} & \phi_\alpha^2(k,\lambda)\left[S_\beta(k,\delta) + R_\varepsilon(\xi,\zeta) - 1\right] \\ & + S_\varepsilon(\xi,\zeta) + 2\phi_\alpha(k,\lambda)U_\varepsilon(\xi,\zeta),\end{aligned} \tag{B.11}$$

$$\begin{aligned}U_\alpha(k,\lambda) = {} & \theta_\alpha(k,\lambda)\Big\{\phi_\alpha(k,\lambda)\left[S_\beta(k,\delta) + R_\varepsilon(\xi,\zeta) - 1\right] \\ & + U_\varepsilon(\xi,\zeta)\Big\} + R_\beta(k,\delta) + \phi_\alpha(k,\lambda)U_\beta(k,\delta),\end{aligned} \tag{B.12}$$

where θ_α and ϕ_α are given in Eq. (A.3) while the meaning of α, β, ε, δ, λ, ξ and ζ are specified in Table A1.

The initial conditions for the renormalization of PR are $I_F(0,1) = J_F(0,1) = 1$, $K_F(0,1) = L_F(0,1) = P_F(0,1) = Q_F(0,1) = 0$, $R_F(0,1) = S_F(0,1) = 1$, $U_F(0,1) = 0$, $E_L(0,1) = E_R(0,1) = 0$, $t_F(0,1) = t_B$, $I_F(1,1) = J_F(1,1) = 1$, $K_F(1,1) = L_F(1,1) = P_F(1,1) = Q_F(1,1) = 0$, $R_F(1,1) = S_F(1,1) = 1$, $U_F(1,1) = 0$, $E_L(1,1) = E_R(1,1) = 0$, and $t_F(1,1) = t_A$.

Appendix C. Renormalization formulas for the Kubo-Greenwood conductivity

In this article, the electrical conductivity (σ) is analyzed by means of the Kubo-Greenwood formula given by Eq. (19), in which the trace can be written as [30]

$$\begin{aligned}& Tr\left\{p\,\mathrm{Im}G^+(E+\hbar\omega)\,p\,\mathrm{Im}G^+(E)\right\} \\ & = \frac{m^2a^2}{4\hbar^2}\left[S(E_\omega^+, E^+, l) + S(E_\omega^-, E^-, l) - S(E_\omega^+, E^-, l) - S(E_\omega^-, E^+, l)\right]\end{aligned} \tag{C.1}$$

where $E_\omega^\pm = E + \hbar\omega \pm i\eta$, $E^\pm = E \pm i\eta$, η is the imaginary part of the energy and

$$\begin{aligned}& S(E_\omega^\kappa, E^\nu, l) \\ & = \sum_{i,j=1}^{N(l)-1} t_{i,i+1}t_{j,j+1}\Big\{2G_{i+1,j}^\kappa(E_\omega)G_{j+1,i}^\nu(E) \\ & - G_{i+1,j+1}^\kappa(E_\omega)G_{j,i}^\nu(E) - G_{i,j}^\kappa(E_\omega)G_{j+1,i+1}^\nu(E)\Big\},\end{aligned} \tag{C.2}$$

in which κ and ν could be $+$ or $-$. The partial sums $S(E_\omega^\kappa, E^\nu, l)$ can be written in terms of the Green's function at extreme sites of the system as

$$\begin{aligned}& S(E_\omega^\kappa, E^\nu, l) = Z_F(E_\omega^\kappa, E^\nu, l, 1) \\ & + A_F(E_\omega^\kappa, E^\nu, l, 1)G_{L,L}(E_\omega^\kappa)G_{L,L}(E^\nu) \\ & + B_F(E_\omega^\kappa, E^\nu, l, 1)G_{L,R}(E_\omega^\kappa)G_{L,R}(E^\nu) \\ & + C_F(E_\omega^\kappa, E^\nu, l, 1)G_{R,R}(E_\omega^\kappa)G_{R,R}(E^\nu) \\ & + D_F(E_\omega^\kappa, E^\nu, l, 1)G_{L,L}(E_\omega^\kappa)G_{L,R}(E^\nu) \\ & + D_F(E^\nu, E_\omega^\kappa, l, 1)G_{L,L}(E^\nu)G_{L,R}(E_\omega^\kappa) \\ & + F_F(E_\omega^\kappa, E^\nu, l, 1)G_{L,L}(E_\omega^\kappa)G_{R,R}(E^\nu) \\ & + F_F(E^\nu, E_\omega^\kappa, l, 1)G_{L,L}(E^\nu)G_{R,R}(E_\omega^\kappa) \\ & + I_F(E_\omega^\kappa, E^\nu, l, 1)G_{L,R}(E_\omega^\kappa)G_{R,R}(E^\nu) \\ & + I_F(E^\nu, E_\omega^\kappa, l, 1)G_{L,R}(E^\nu)G_{R,R}(E_\omega^\kappa) \\ & + J_F(E_\omega^\kappa, E^\nu, l, 1)G_{L,L}(E_\omega^\kappa) \\ & + J_F(E^\nu, E_\omega^\kappa, l, 1)G_{L,L}(E^\nu) \\ & + K_F(E_\omega^\kappa, E^\nu, l, 1)G_{L,R}(E_\omega^\kappa) \\ & + K_F(E^\nu, E_\omega^\kappa, l, 1)G_{L,R}(E^\nu) \\ & + L_F(E_\omega^\kappa, E^\nu, l, 1)G_{R,R}(E_\omega^\kappa) \\ & + L_F(E^\nu, E_\omega^\kappa, l, 1)G_{R,R}(E^\nu),\end{aligned} \tag{C.3}$$

where the subscripts L and R of the Green's function respectively denote the left and right extreme atom. The coefficients $A_F(E_1, E_2, l, 1)$, $B_F(E_1, E_2, l, 1)$, $\cdots$, $Z_F(E_1, E_2, l, 1)$ in Eq. (C.3), being E_1 and E_2 either E_ω^κ or E^ν, can be iteratively calculated for $k = 2, 3, \cdots, l$ by means of

$$A_\alpha(E_1, E_2, k, \lambda) = -\left[P_\alpha(E_1, E_2, k, \lambda) - P_\alpha(E_2, E_1, k, \lambda)\right]^2, \tag{C.4}$$

$$\begin{aligned}& B_\alpha(E_1, E_2, k, \lambda) = 2[P_\alpha(E_1, E_2, k, \lambda) - \\ & P_\alpha(E_2, E_1, k, \lambda)][Q_\alpha(E_2, E_1, k, \lambda) - Q_\alpha(E_1, E_2, k, \lambda)] \\ & + 2[R_\alpha(E_1, E_2, k, \lambda) - S_\alpha(E_2, E_1, k, \lambda)] \times \\ & [R_\alpha(E_2, E_1, k, \lambda) - S_\alpha(E_1, E_2, k, \lambda)],\end{aligned} \tag{C.5}$$

$$C_\alpha(E_1, E_2, k, \lambda) = -\left[Q_\alpha(E_1, E_2, k, \lambda) - Q_\alpha(E_2, E_1, k, \lambda)\right]^2, \tag{C.6}$$

$$D_\alpha(E_1,E_2,k,\lambda) = 2[P_\alpha(E_1,E_2,k,\lambda)-P_\alpha(E_2,E_1,k,\lambda)] \times[S_\alpha(E_2,E_1,k,\lambda)-R_\alpha(E_1,E_2,k,\lambda)], \tag{C.7}$$

$$F_\alpha(E_1,E_2,k,\lambda) = -[R_\alpha(E_1,E_2,k,\lambda)-S_\alpha(E_2,E_1,k,\lambda)]^2, \tag{C.8}$$

$$I_\alpha(E_1,E_2,k,\lambda) = 2[Q_\alpha(E_1,E_2,k,\lambda)-Q_\alpha(E_2,E_1,k,\lambda)] \times[S_\alpha(E_2,E_1,k,\lambda)-R_\alpha(E_1,E_2,k,\lambda)], \tag{C.9}$$

$$\begin{aligned} J_\alpha(E_1,E_2,k,\lambda) &= \rho_\alpha(E_2,k,\lambda)F_\beta(E_1,E_2,k,\delta) \\ &+\theta_\alpha(E_1,k,\lambda)K_\beta(E_1,E_2,k,\delta)+\theta_\alpha(E_1,k,\lambda) \\ &\times\rho_\alpha(E_2,k,\lambda)\{I_\beta(E_1,E_2,k,\delta)+U_\alpha(E_1,E_2,k,\lambda) \\ &+\theta_\alpha(E_1,k,\lambda)[C_\beta(E_1,E_2,k,\delta)+A_\varepsilon(E_1,E_2,\xi,\zeta) \\ &+T_\alpha(E_1,E_2,k,\lambda)]\}+\theta_\alpha^2(E_1,k,\lambda) \\ &\times[L_\beta(E_1,E_2,k,\delta)+J_\varepsilon(E_1,E_2,\xi,\zeta)] \\ &+J_\beta(E_1,E_2,k,\delta), \end{aligned} \tag{C.10}$$

$$\begin{aligned} K_\alpha(E_1,E_2,k,\lambda) &= 2\rho_\alpha(E_2,k,\lambda)\theta_\alpha(E_1,k,\lambda) \\ &\times\phi_\alpha(E_1,k,\lambda)[C_\beta(E_1,E_2,k,\delta)+A_\varepsilon(E_1,E_2,\xi,\zeta) \\ &+T_\alpha(E_1,E_2,k,\lambda)]+\rho_\alpha(E_2,k,\lambda)V_\alpha(E_1,E_2,k,\lambda) \\ &+2\theta_\alpha(E_1,k,\lambda)\phi_\alpha(E_1,k,\lambda)[L_\beta(E_1,E_2,k,\delta) \\ &+J_\varepsilon(E_1,E_2,\xi,\zeta)]+\rho_\alpha(E_2,k,\lambda)\{\theta_\alpha(E_1,k,\lambda) \\ &\times[D_\varepsilon(E_2,E_1,\xi,\zeta)+W_\alpha(E_2,E_1,k,\lambda)]+ \\ &\phi_\alpha(E_1,k,\lambda)[I_\beta(E_1,E_2,k,\delta)+U_\alpha(E_1,E_2,k,\lambda)]\} \\ &+\phi_\alpha(E_1,k,\lambda)K_\beta(E_1,E_2,k,\delta) \\ &+\theta_\alpha(E_1,k,\lambda)K_\varepsilon(E_1,E_2,\xi,\zeta), \end{aligned} \tag{C.11}$$

$$\begin{aligned} L_\alpha(E_1,E_2,k,\lambda) &= \rho_\alpha(E_2,k,\lambda)F_\varepsilon(E_2,E_1,\xi,\zeta) \\ &+\phi_\alpha(E_1,k,\lambda)K_\varepsilon(E_1,E_2,\xi,\zeta)+\rho_\alpha(E_2,k,\lambda)\times \\ &\phi_\alpha(E_1,k,\lambda)\{D_\varepsilon(E_2,E_1,\xi,\zeta)+W_\alpha(E_2,E_1,k,\lambda) \\ &+\phi_\alpha(E_1,k,\lambda)[C_\beta(E_1,E_2,k,\delta)+A_\varepsilon(E_1,E_2,\xi,\zeta)+ \\ &T_\alpha(E_1,E_2,k,\lambda)]\}+\phi_\alpha^2(E_1,k,\lambda)[L_\beta(E_1,E_2,k,\delta) \\ &+J_\varepsilon(E_1,E_2,\xi,\zeta)]+L_\varepsilon(E_1,E_2,\xi,\zeta), \end{aligned} \tag{C.12}$$

and

$$\begin{aligned} Z_\alpha(E_1,E_2,k,\lambda) &= \rho_\alpha(E_1,k,\lambda)[L_\beta(E_1,E_2,k,\delta) \\ &+J_\varepsilon(E_1,E_2,\xi,\zeta)]+Z_\beta(E_1,E_2,k,\delta)+\rho_\alpha(E_1,k,\lambda) \\ &\times\rho_\alpha(E_2,k,\lambda)[C_\beta(E_1,E_2,k,\delta)+A_\varepsilon(E_1,E_2,\xi,\zeta) \\ &+T_\alpha(E_1,E_2,k,\lambda)]+\rho_\alpha(E_2,k,\lambda) \\ &\times[L_\beta(E_2,E_1,k,\delta)+J_\varepsilon(E_2,E_1,\xi,\zeta)] \\ &+Z_\varepsilon(E_1,E_2,\xi,\zeta), \end{aligned} \tag{C.13}$$

where the meaning of α, β, ε, δ, λ, ξ and ζ are specified in Table A1 for each stage of renormalization,

$$\rho_\alpha(E_\varphi,k,\lambda) = [z-E_L(E_\varphi,\xi,\zeta)-E_R(E_\varphi,k,\delta)]^{-1}, \tag{C.14}$$

$$\theta_\alpha(E_\varphi,k,\lambda) = t_\beta(E_\varphi,k,\delta)\rho_\alpha(E_\varphi,k,\lambda), \tag{C.15}$$

$$\phi_\alpha(E_\varphi,k,\lambda) = t_\varepsilon(E_\varphi,\xi,\zeta)\rho_\alpha(E_\varphi,k,\lambda), \tag{C.16}$$

$$E_L(E_\varphi,k,\lambda) = E_L(E_\varphi,k,\delta)+t_\beta^2(E_\varphi,k,\delta)\rho_\alpha(E_\varphi,k,\lambda), \tag{C.17}$$

$$E_R(E_\varphi,k,\lambda) = E_\varepsilon(E_\varphi,\xi,\zeta)+t_\varepsilon^2(E_\varphi,\xi,\zeta)\rho_\alpha(E_\varphi,k,\lambda), \tag{C.18}$$

$$t_\alpha(E_\varphi,k,\lambda) = t_\beta(E_\varphi,k,\delta)t_\varepsilon(E_\varphi,\xi,\zeta)\rho_\alpha(E_\varphi,k,\lambda), \tag{C.19}$$

$$\begin{aligned} P_\alpha(E_1,E_2,k,\lambda) &= \theta_\alpha(E_2,k,\lambda)R_\beta(E_1,E_2,k,\delta) \\ &+\theta_\alpha(E_1,k,\lambda)S_\beta(E_1,E_2,k,\delta)+\theta_\alpha(E_1,k,\lambda)\times \\ &\theta_\alpha(E_2,k,\lambda)[P_\varepsilon(E_1,E_2,\xi,\zeta)+Q_\beta(E_1,E_2,k,\delta)] \\ &+P_\beta(E_1,E_2,k,\delta), \end{aligned} \tag{C.20}$$

$$\begin{aligned} Q_\alpha(E_1,E_2,k,\lambda) &= \phi_\alpha(E_1,k,\lambda)R_\varepsilon(E_1,E_2,\xi,\zeta) \\ &+Q_\varepsilon(E_1,E_2,\xi,\zeta)+\phi_\alpha(E_2,k,\lambda)S_\varepsilon(E_1,E_2,\xi,\zeta) \\ &+\phi_\alpha(E_1,k,\lambda)\phi_\alpha(E_2,k,\lambda)[P_\varepsilon(E_1,E_2,\xi,\zeta) \\ &+Q_\beta(E_1,E_2,k,\delta)], \end{aligned} \tag{C.21}$$

$$\begin{aligned} R_\alpha(E_1,E_2,k,\lambda) &= \phi_\alpha(E_2,k,\lambda)R_\beta(E_1,E_2,k,\delta) \\ &+\theta_\alpha(E_1,k,\lambda)\phi_\alpha(E_2,k,\lambda)[P_\varepsilon(E_1,E_2,\xi,\zeta)+ \\ &Q_\beta(E_1,E_2,k,\delta)]+\theta_\alpha(E_1,k,\lambda)R_\varepsilon(E_1,E_2,\xi,\zeta), \end{aligned} \tag{C.22}$$

$$\begin{aligned} S_\alpha(E_1,E_2,k,\lambda) &= \phi_\alpha(E_1,k,\lambda)S_\beta(E_1,E_2,k,\delta) \\ &+\theta_\alpha(E_2,k,\lambda)\phi_\alpha(E_1,k,\lambda)[P_\varepsilon(E_1,E_2,\xi,\zeta)+ \\ &Q_\beta(E_1,E_2,k,\delta)]+\theta_\alpha(E_2,k,\lambda)S_\varepsilon(E_1,E_2,\xi,\zeta), \end{aligned} \tag{C.23}$$

$$T_\alpha(E_1,E_2,k,\lambda) = 2[P_\varepsilon(E_1,E_2,\xi,\zeta)-P_\varepsilon(E_2,E_1,\xi,\zeta)] \times[Q_\beta(E_2,E_1,k,\delta)-Q_\beta(E_1,E_2,k,\delta)], \tag{C.24}$$

$$U_\alpha(E_1,E_2,k,\lambda) = 2[P_\varepsilon(E_1,E_2,\xi,\zeta)-P_\varepsilon(E_2,E_1,\xi,\zeta)] \times[S_\beta(E_2,E_1,k,\delta)-R_\beta(E_1,E_2,k,\delta)], \tag{C.25}$$

$$V_\alpha(E_1,E_2,k,\lambda) = 2[S_\varepsilon(E_1,E_2,\xi,\zeta)-R_\varepsilon(E_2,E_1,\xi,\zeta)] \times[S_\beta(E_2,E_1,k,\delta)-R_\beta(E_1,E_2,k,\delta)], \tag{C.26}$$

and

$$W_\alpha(E_1,E_2,k,\lambda) = 2[Q_\beta(E_1,E_2,k,\delta)-Q_\beta(E_2,E_1,k,\delta)] \times[S_\varepsilon(E_2,E_1,\xi,\zeta)-R_\varepsilon(E_1,E_2,\xi,\zeta)], \tag{C.27}$$

being E_φ either E_1 or E_2.

The Green's functions at the ends of system are the same as in Appendix A, except they are evaluated at E_φ instead of z, *i.e.*,

$$G_{L,L}(E_\varphi) = \left\{E_\varphi-E_L(E_\varphi,l,1)-\frac{t_P^2(l')}{E_\varphi-E_P^L(l')} -E_P^R(l')-\frac{t_F^2(E_\varphi,l,1)}{E_\varphi-E_R(E_\varphi,l,1)-E_P^L(l')-\frac{t_P^2(l')}{E_\varphi-E_P^R(l')}}\right\}^{-1}, \tag{C.28}$$

$$G_{R,R}(E_\varphi) = \left\{E_\varphi-E_R(E_\varphi,l,1)-\frac{t_P^2(l')}{E_\varphi-E_P^R(l')} -E_P^L(l')-\frac{t_F^2(E_\varphi,l,1)}{E_\varphi-E_L(E_\varphi,l,1)-E_P^R(l')-\frac{t_P^2(l')}{E_\varphi-E_P^L(l')}}\right\}^{-1}, \tag{C.29}$$

and

$$G_{L,R}(E_\varphi) = \frac{t_F(E_\varphi,l,1)G_{R,R}(E_\varphi)}{E_\varphi-E_L(E_\varphi,l,1)-E_P^R(l')-\frac{t_P^2(l')}{E_\varphi-E_P^L(l')}}. \tag{C.30}$$

Finally, the initial conditions are $A_F(E_1,E_2,0,1)=0$, $C_F(E_1,E_2,0,1)=0$, $D_F(E_1,E_2,0,1)=0$, $I_F(E_1,E_2,0,1)=0$, $J_F(E_1,E_2,0,1)=0$, $K_F(E_1,E_2,0,1)=0$, $L_F(E_1,E_2,0,1)=0$, $Z_F(E_1,E_2,0,1)=0$, $P_F(E_1,E_2,0,1)=0$, $Q_F(E_1,E_2,0,1)=0$, $R_F(E_1,E_2,0,1)=0$, $E_L(E_\varphi,0,1)=0$, $E_R(E_\varphi,0,1)=0$, $B_F(E_1,E_2,0,1)=2t_B^2$, $F_F(E_1,E_2,0,1)=-t_B^2$, $t_F(E_\varphi,0,1)=t_B$, $A_F(E_1,E_2,1,1)=0$, $S_F(E_1,E_2,0,1)=t_B$, $C_F(E_1,E_2,1,1)=0$, $D_F(E_1,E_2,1,1)=0$, $I_F(E_1,E_2,1,1)=0$, $J_F(E_1,E_2,1,1)=0$, $K_F(E_1,E_2,1,1)=0$, $L_F(E_1,E_2,1,1)=0$, $Z_F(E_1,E_2,1,1)=0$, $P_F(E_1,E_2,1,1)=0$, $Q_F(E_1,E_2,1,1)=0$, $R_F(E_1,E_2,1,1)=0$, $E_L(E_\varphi,1,1)=0$, $E_R(E_\varphi,1,1)=0$, $B_F(E_1,E_2,1,1)=2t_A^2$, $F_F(E_1,E_2,1,1)=-t_A^2$, $S_F(E_1,E_2,1,1)=t_A$, and $t_F(E_\varphi,1,1)=t_A$.

References

[1] E. Abrahams, P.W. Anderson, D.C. Licciardello, T.V. Ramakrishnan, Phys. Rev. Lett. 42 (1979) 673.
[2] C. Flores, J. Phys. C 1 (1989) 8471.
[3] D.H. Dunlap, H.L. Wu, P.W. Phillips, Phys. Rev. Lett. 65 (1990) 88.

[4] V. Bellani, E. Diez, R. Hey, L. Toni, L. Tarricone, G.B. Parravicini, F. Domínguez-Adame, R. Gómez-Alcalá, Phys. Rev. Lett. 82 (1999) 2159.
[5] U. Kuhl, F.M. Izrailev, A.A. Krokhin, H.J. Stöckmann, Appl. Phys. Lett. 77 (2000) 633.
[6] D. Shechtman, I. Blech, D. Gratias, J.W. Cahn, Phys. Rev. Lett. 53 (1984) 1951.
[7] R. Merlin, K. Bajema, R. Clarke, F.Y. Juang, P.K. Bhattacharya, Phys. Rev. Lett. 55 (1985) 1768.
[8] C. Wang, R.A. Barrio, Phys. Rev. Lett. 61 (1988) 191.
[9] M. Kohmoto, B. Sutherland, C. Tang, Phys. Rev. B 35 (1987) 1020.
[10] A. Sütő, J. Stat. Phys. 56 (1989) 525.
[11] E. Maciá, Rep. Prog. Phys. 75 (2012) 036502.
[12] G. Gumbs, M.K. Ali, Phys. Rev. Lett. 60 (1988) 1081.
[13] G. Gumbs, G.S. Dubey, A. Salman, B.S. Mahmoud, D. Huang, Phys. Rev. B 52 (1995) 210.
[14] A.G. Barriuso, J.J. Monzón, T. Yonte, A. Felipe, L.L. Sánchez-Soto, Opt. Express 21 (2013) 30039.
[15] J.X. Zhong, J.R. Yan, J.Q. You, J. Phys. A Math. Gen. 24 (1991) L949.
[16] A. Chakrabarti, S.N. Karmakar, Phys. Rev. B 44 (1991) 896.
[17] V. Sánchez, L.A. Pérez, R. Oviedo-Roa, C. Wang, Phys. Rev. B 64 (2001) 174205.
[18] V. Sanchez, C. Wang, J. Alloys Compd. 342 (2002) 410.
[19] V. Sánchez, C. Wang, Philos. Mag. 95 (2015) 326.
[20] G.Y. Oh, M.H. Lee, Phys. Rev. B 48 (1993) 12465.
[21] X. Fu, Y. Liu, Z. Gou, P. Zhou, X. Huang, Phys. Rev. B 51 (1995) 3910.
[22] E. Maciá, Aperiodic Structures in Condensed Matter: Fundamentals and Applications, CRC Press, Boca Raton, 2009 132.
[23] J.W.S. Cassels, An Introduction to Diophantine Approximation, Cambridge University Press, Cambridge, 1957 133.
[24] J.M. Luck, C. Godreche, A. Janner, T. Janssen, J. Phys. A Math. Gen. 26 (1993) 1951.
[25] W. Steurer, Crytallography of Quasicrystals, Springer, Berlin, 2009 13.
[26] E.N. Economou, Green's Functions in Quantum Physics, Springer, Berlin, 2006 7.
[27] R. Oviedo-Roa, L.A. Pérez, C. Wang, Phys. Rev. B 62 (2000) 13805.
[28] Y. Imry, R. Landauer, Rev. Mod. Phys. 71 (1999) S306.
[29] B. Kramer, A. MacKinon, Rep. Prog. Phys. 56 (1993) 1469.
[30] V. Sánchez, C. Wang, Phys. Rev. B 70 (2004) 144207.
[31] S. Thiem, M. Schreiber, Eur. Phys. J. B 83 (2011) 415.
[32] V. Sánchez, C. Wang, Int. J. Comp. Mat. Sci. Eng. 1 (2012) 1250003.
[33] D. Damanik, Lett. Math. Phys. 46 (1998) 303.
[34] C. Wang, C. Ramírez, F. Sánchez, V. Sánchez, Phys. Status Solidi B 252 (2015) 1370.

Journal of ELECTRONIC MATERIALS
DOI: 10.1007/s11664-016-4946-y
© 2016 The Minerals, Metals & Materials Society

Improving Thermoelectric Properties of Nanowires Through Inhomogeneity

J. EDUARDO GONZÁLEZ,[1] VICENTA SÁNCHEZ,[2] and CHUMIN WANG[1,3]

1.—Instituto de Investigaciones en Materiales, Universidad Nacional Autónoma de México, Mexico City, Mexico. 2.—Departamento de Física, Facultad de Ciencias, Universidad Nacional Autónoma de México, Mexico City, Mexico. 3.—e-mail: chumin@unam.mx

Inhomogeneity in nanowires can be present in the cross-section and/or by breaking the translational symmetry along the nanowire. In particular, the quasiperiodicity introduces an unusual class of electronic and phononic transport with a singular continuous eigenvalue spectrum and critically localized wave functions. In this work, the thermoelectricity in periodic and quasiperiodically segmented nanobelts and nanowires is addressed within the Boltzmann formalism by using a real-space renormalization plus convolution method developed for the Kubo–Greenwood formula, in which tight-binding and Born models are, respectively, used for the calculation of electric and lattice thermal conductivities. For periodic nanowires, we observe a maximum of the thermoelectric figure-of-merit (ZT) in the temperature space, as occurred in the carrier concentration space. This maximum ZT can be improved by introducing into nanowires periodically arranged segments and an inhomogeneous cross-section. Finally, the quasiperiodically segmented nanowires reveal an even larger ZT in comparison with the periodic ones.

Key words: Thermoelectricity, Kubo–Greenwood formula, real-space renormalization method, nanowire heterostructures

INTRODUCTION

The direct conversion between thermal and electrical energies by thermoelectric devices has attracted great attention in recent years. Low-dimensional materials seem to be promising candidates for high-performance thermoelectric devices, whose efficiency is determined by the dimensionless figure-of-merit defined as $ZT \equiv (\sigma S^2 T)/(\kappa_{el} + \kappa_{ph})$, where the Seebeck coefficient (S), electrical conductivity (σ), electronic (κ_{el}) and phononic (κ_{ph}) thermal conductivities can be calculated by using the Boltzmann formalism.[1] The inherent correlation between these thermoelectric quantities makes difficult to improve the value of ZT.

In general, the Seebeck coefficient (S) is proportional to the average transported electron energy relative to the chemical potential (μ), i.e., $S \propto \langle E - \mu \rangle$.[2] Thus, S is null for μ located at the center of a symmetric electronic band. When μ moves towards the band edges in a three-dimensional system, the magnitude of S grows and σ diminishes. The combination of these two trends leads to the existence of a maximum ZT in the carrier concentration space.[3]

In the temperature space, the power factor (σS^2) is null at zero temperature, since σ or S is, respectively, nil for μ located outside or inside the electronic band. Hence, the power factor increases with T in the low-temperature regime, because it is a positively defined quantity. This trend has been observed in single nanowires.[4,5] For the extreme high-temperature limit, both electrons and holes of a semiconductor have contributions to S with different sign and almost the same magnitude, leading to a significant reduction of the Seebeck coefficient. Consequently, a maximum ZT is often observed in the temperature space.[6]

This maximum ZT can be improved by reducing the cross-section of a nanowire, as reported by many

(Received June 2, 2016; accepted September 7, 2016)

Published online: 14 October 2016

theoretical[7] and experimental[8] studies, where a rapid growth of the power factor with the reduction of cross-section area is observed. On the other hand, nanowire (NW) heterostructures constitute another important alternative to improve thermoelectric properties, because the phonon scattering at the compositional interfaces leads to a lower lattice thermal conductivity.[9] For example, $M_2O_3(ZnO)_n$ (M = In, Ga, Fe) segmented nanowires reveal the importance of segmentation in nanowires.[10] In fact, a quasiperiodic arrangement of these segments following the Fibonacci sequence could induce interesting changes in the thermoelectric properties of a nanowire, since its energy spectrum is singular continuous on a Cantor set of zero Lebesgue measure[11] whose wavefuctions are critical and self-similarly localized in the real space.[12] In this article, we analyze the dependence of ZT on the temperature, carrier concentration, cross-section area and longitudinal inhomogeneity of a nanowire, by using the Boltzmann and Kubo–Greenwood formalisms and a previously developed renormalization plus convolution method.

In order to isolate the effects of long-range quasiperiodic order on thermoelectric properties, we will carry out this analysis by means of a simple single-electron tight-binding Hamiltonian and a first-neighbor Born model on cubically structured nanowires, without considering the electron–electron and electron–phonon interactions nor the anharmonicity. This kind of electronic Hamiltonians has been successfully used in the description of electronic properties of semiconductors,[13] while its vibrational behavior derived from covalent bonds can be properly reproduced by the nearest-neighbor Born model including central and non-central forces.[14,15] Despite the simplicity of this semi-empirical model, its results can be extended beyond the analyzed parameters, as discussed in "Analysis of Parameter Dependence".

THE MODEL

Based on the Boltzmann formalism and the Kubo–Greenwood formula, thermoelectric quantities can be calculated through[16,17]

$$ZT = \frac{\sigma S^2 T}{\kappa_{\mathrm{el}} + \kappa_{\mathrm{ph}}}, \tag{1}$$

$$\sigma(\mu,T) = e^2 L_0(\mu,T), \tag{2}$$

$$S(\mu,T) = -\frac{L_1(\mu,T)}{|e|TL_0(\mu,T)}, \tag{3}$$

and

$$\kappa_{\mathrm{el}}(\mu,T) = \frac{L_2(\mu,T)L_0(\mu,T) - L_1^2(\mu,T)}{TL_0(\mu,T)}, \tag{4}$$

where

$$L_n(\mu,T) = \frac{-2\hbar}{\pi m^2 \Omega}\int_{-\infty}^{\infty} \mathrm{d}E(E-\mu)^n \frac{\partial f}{\partial E}\mathrm{Tr}\left\{\hat{p}_{\mathrm{x}}\tilde{G}(E)\hat{p}_{\mathrm{x}}\tilde{G}(E)\right\}, \tag{5}$$

being Ω the system volume, $\hat{p}_{\mathrm{x}}$ the projection of momentum operator along the nanowire, $f(E) = \{1+\exp[(E-\mu)/(k_{\mathrm{B}}T)]\}^{-1}$ the Fermi-Dirac distribution with chemical potential μ and temperature T, $\tilde{G}(E) = G^{+}(E) - G^{-}(E)$ the discontinuity of Green's functions with $G^{+}(E)$ and $G^{-}(E)$ being the retarded and advanced single-electron Green's functions, respectively.[18]

On the other hand, the lattice thermal conductivity (κ_{ph}) can be calculated by using the Kubo–Greenwood formula for phonons given by[19,20]

$$\kappa_{\mathrm{ph}}(T) = \frac{-2\hbar^2}{\pi\Omega k_{\mathrm{B}}}\sum_l \int_0^{\infty} \mathrm{d}\omega \frac{\omega^2 e^{\hbar\omega/k_{\mathrm{B}}T}}{T^2\left(e^{\hbar\omega/k_{\mathrm{B}}T}-1\right)^2} \mathrm{Tr}\left\{A_{\mathrm{x}}\tilde{G}_{\mathrm{ph}}(\omega)A_{\mathrm{x}}\tilde{G}_{\mathrm{ph}}(\omega)\right\}_l, \tag{6}$$

where the summation of l is over the longitudinal (L) and transversal (T) modes, $\tilde{G}_{\mathrm{ph}}(\omega)$ is the discontinuity of phononic Green's functions determined by $(M\omega^2 I - \Phi)G_{\mathrm{ph}}(\omega) = I$ and the elements of matrix $\mathbf{A}_{\mathrm{x}}$ are $[A_{\mathrm{x}}]_{\nu\nu'}(l,j) \equiv \frac{1}{2}(R_l - R_j)_{\mathrm{x}}\Phi_{\nu\nu'}(l,j)$, being M the atomic mass, $\mathbf{I}$ the matrix identity and $\Phi_{\nu\nu'}(l,j) = \partial^2 V_{lj}/\partial u_{\nu}(l)\partial u_{\nu'}(j)$ the dynamic matrix. The interaction potential (V_{lj}) between nearest-neighbor atoms l and j in the Born model is given by[15] $V_{lj} = \frac{1}{2}(\alpha-\beta)\left|[u(l)-u(j)]\cdot\hat{n}_{lj}\right|^2 + \frac{1}{2}\beta|[u(l)-u(j)]|^2$, where $u(j)$ is the displacement of atom j with respect to its equilibrium position, α and β are the central and non-central restoring force constants, respectively. The unitary vector $\hat{n}_{lj}$ indicates the bond direction between atoms l and j. Notice that in this article the temperature dependence of thermoelectric properties arises from the statistical factors in Eqs. 5 and 6, while the electronic band structure is independent on the carrier concentration determined by the position of chemical potential.

Let us consider a single-band tight-binding Hamiltonian ($\hat{H}$) with null on-site self-energies given by $\hat{H} = \sum_{\langle l,j\rangle}\{t_{l,j}|l\rangle\langle j| + t_{j,l}|j\rangle\langle l|\}$, where $t_{l,j} = t_{j,l}$ is the nearest-neighbor hopping integral. For the sake of simplicity, a uniform bond length (a) is taken and $\hat{p}_{\mathrm{x}} = \frac{im}{\hbar}\left[\hat{H},x\right] = \frac{ima}{\hbar}\sum_l\{t_{l,l+1}|l\rangle\langle l+1| - t_{l-1,l}|l\rangle\langle l-1|\}$. For a cubically structured nanowire with planar defects, the Hamiltonian $\hat{H}$ and the dynamic matrix Φ are separable, i.e., $\hat{H} = \hat{H}_{\parallel}\otimes\hat{I}_{\perp} + \hat{I}_{\parallel}\otimes\hat{H}_{\perp}$, where $\hat{H}_{\parallel}$ ($\hat{I}_{\parallel}$) and $\hat{H}_{\perp}$ ($\hat{I}_{\perp}$) are Hamiltonians (identity matrices) of the parallel and perpendicular subsystems, respectively. The convolution theorem can be expressed as[21]

$$\mathrm{Tr}\left(\hat{p}_x\tilde{G}(E)\hat{p}_x\tilde{G}(E)\right) = \sum_\lambda \mathrm{Tr}\left(\hat{p}_x\tilde{G}^{\parallel}(E-E_\lambda)\hat{p}_x\tilde{G}^{\parallel}(E-E_\lambda)\right) \quad (7)$$

for electrons and

$$\mathrm{Tr}\left\{A_x\tilde{G}_{\mathrm{ph}}(\omega^2)A_x\tilde{G}_{\mathrm{ph}}(\omega^2)\right\}_l = \sum_\lambda \mathrm{Tr}\left\{A_x\tilde{G}^{\parallel}_{\mathrm{ph}}(\omega^2-\omega_\lambda^2)A_x\tilde{G}^{\parallel}_{\mathrm{ph}}(\omega^2-\omega_\lambda^2)\right\}_l \quad (8)$$

for phonons, where E_λ and $M\omega_\lambda^2$ are eigenvalues of $\hat{H}_\perp$ and $\Phi_\perp$, respectively. In this article, we only analyze the bond problem, i.e., nanowires with null self-energies and a constant atomic mass (M).

PERIODIC NANOWIRES

For cubically structured periodic NW of $N_\parallel N_\perp$ atoms connected to two semi-infinite periodic NW leads with hopping integrals t and Born central (α) and non-central (β) interactions, analytical solutions of thermoelectric quantities can be found, since the traces of Eqs. 7 and 8 for a periodic NW with square cross-section of $N_\perp$ atoms are, respectively, given by,[22]

$$\mathrm{Tr}\left\{\hat{p}_x\tilde{G}(E)\hat{p}_x\tilde{G}(E)\right\} = \sum_\lambda \left[\Theta(E-E_\lambda+2|t|)-\Theta(E-E_\lambda-2|t|)\right] \left(N_\parallel-1\right)^2a^2m^2\Big/\left(2\hbar^2\right) \quad (9)$$

and

$$\mathrm{Tr}\left\{A_x\tilde{G}_{\mathrm{ph}}(\omega^2)A_x\tilde{G}_{\mathrm{ph}}(\omega^2)\right\}_l = -\sum_\lambda \left[\left[1-\Theta\left(\omega^2-\omega_{\lambda_l}^2-4\omega_l^2\right)\right]\left(N_\parallel-1\right)^2a^2\Big/8\right], \quad (10)$$

where $\Theta(x)$ is the Heaviside step function, ω_l^2 could be $\omega_\alpha^2=\alpha/M$ for longitudinal or $\omega_\beta^2=\beta/M$ for transversal vibrational modes,

$$E_\lambda = -2|t|\left\{\cos\left[m\pi\Big/\left(N_\perp^{1/2}+1\right)\right] + \cos\left[n\pi\Big/\left(N_\perp^{1/2}+1\right)\right]\right\}, \quad (11)$$

$$\omega_{\lambda_L}^2 = 2\omega_\beta^2\left\{2-\cos\left[(m-1)\pi\Big/N_\perp^{1/2}\right] - \cos\left[(n-1)\pi\Big/N_\perp^{1/2}\right]\right\}, \quad (12)$$

and

$$\omega_{\lambda_T}^2 = 2\omega_\alpha^2\left\{1-\cos\left[(m-1)\pi\Big/N_\perp^{1/2}\right]\right\} + 2\omega_\beta^2\left\{1-\cos\left[(n-1)\pi\Big/N_\perp^{1/2}\right]\right\}, \quad (13)$$

being $m=1,2,\ldots,N_\perp^{1/2}$ and $n=1,2,\ldots,N_\perp^{1/2}$.

In Fig. 1, we show (a–d) the electronic density of states $\mathrm{DOS}(\mu)=-\frac{1}{\pi}\sum_j \mathrm{Im}\left[G_j^+(\mu)\right]$ (blue lines) and (a′–d′) the zero-temperature electrical conductance $g(\mu)=\sigma(\mu)\Omega_\perp/\Omega_\parallel$ (red lines) normalized by the quantum conductance $g_0=2e^2/h$ as functions of the chemical potential (μ) for (a,a′) a periodic chain, (b,b′) a periodic nanobelt with cross-section of 7×1 atoms, and periodic nanowires with cross-sections of (c,c′) 7×3 and (d,d′) 7×5 atoms, whose structures are schematically presented in the respective figures (a″–d″). All these nanostructures have a length of $N_\parallel=100663297$ atoms connected to two semi-infinite periodic leads with the same cross-section and Hamiltonian parameters of the system. The figures of this section correspond to periodic nanostructures with null self-energies, hopping integral $t=-1$ eV, atomic mass $M=4.81381\times10^{-26}$ kg, central and non-central restoring force constants $\alpha=100$ N/m and $\beta=20$ N/m, respectively. These vibrational parameters are close to those of crystalline silicon[15] and lead to $\hbar\omega_\alpha=30$ meV. The imaginary part of energy used in this article has been $\eta=10^{-3}|t|$ for DOS and $\eta=10^{-3}|t|/N_\parallel$ for conductance. Observe the quantized conductance steps present in these periodic nanostructures and its number grows with the cross-section area. Furthermore, in DOS spectra, the van Hove singularity is found at the edge of each step.

In Fig. 2, we show (a, a′, a″) the density of states (DOS) (gray lines) and electrical conductivity (σ) normalized by $\sigma_0=e^2\Omega_\parallel/(a\pi\hbar)$ of a periodic chain, (b, b′, b″) Seebeck coefficient (S) normalized by $S_0=-k_B/|e|$, (c, c′, c″) thermal conductivity by electrons (κ_{el}), (d, d′, d″) lattice thermal conductivity (κ_{ph}) normalized by $\kappa_0=k_B\omega_\alpha\Omega_\parallel/(2a\pi)$ of a periodic chain, and (e, e′, e″) ZT as functions of chemical potential (μ) for the same periodic (a–e) nanobelt, (a′–e′) nanowire with cross-section of 7×3 atoms and (a″–e″) nanowire with cross-section of 7×5 atoms as in Fig. 1. The temperature (T) dependence of these thermoelectric properties is exhibited in Fig. 3 for the same nanostructures analyzed in Fig. 2, where the chemical potentials are chosen at $\mu_{\mathrm{out}}=E_c-0.01$ eV and $\mu_{\mathrm{in}}=E_c-0.01$ eV, being band edges at $E_c=-3.84776$ eV, $E_c=-5.26197$ eV and $E_c=-5.57981$ eV, respectively, for the periodic nanobelt with cross-section of 7×1, and nanowires with cross-sections of 7×3 and 7×5 atoms.

Observe that the electrical (σ) and thermal conductivities (κ_{el} and κ_{ph}) in Fig. 2 diminish with the growth of cross-section area, due to the quantum interference between conduction channels. For a given temperature, the Seebeck coefficient (S) linearly increases when μ moves away from the band edge and this linear dependence has a weak influence of the cross-section area. Furthermore, maximum values of ZT are found, as a consequence of the growth of σ and the decay of S when μ increases, and

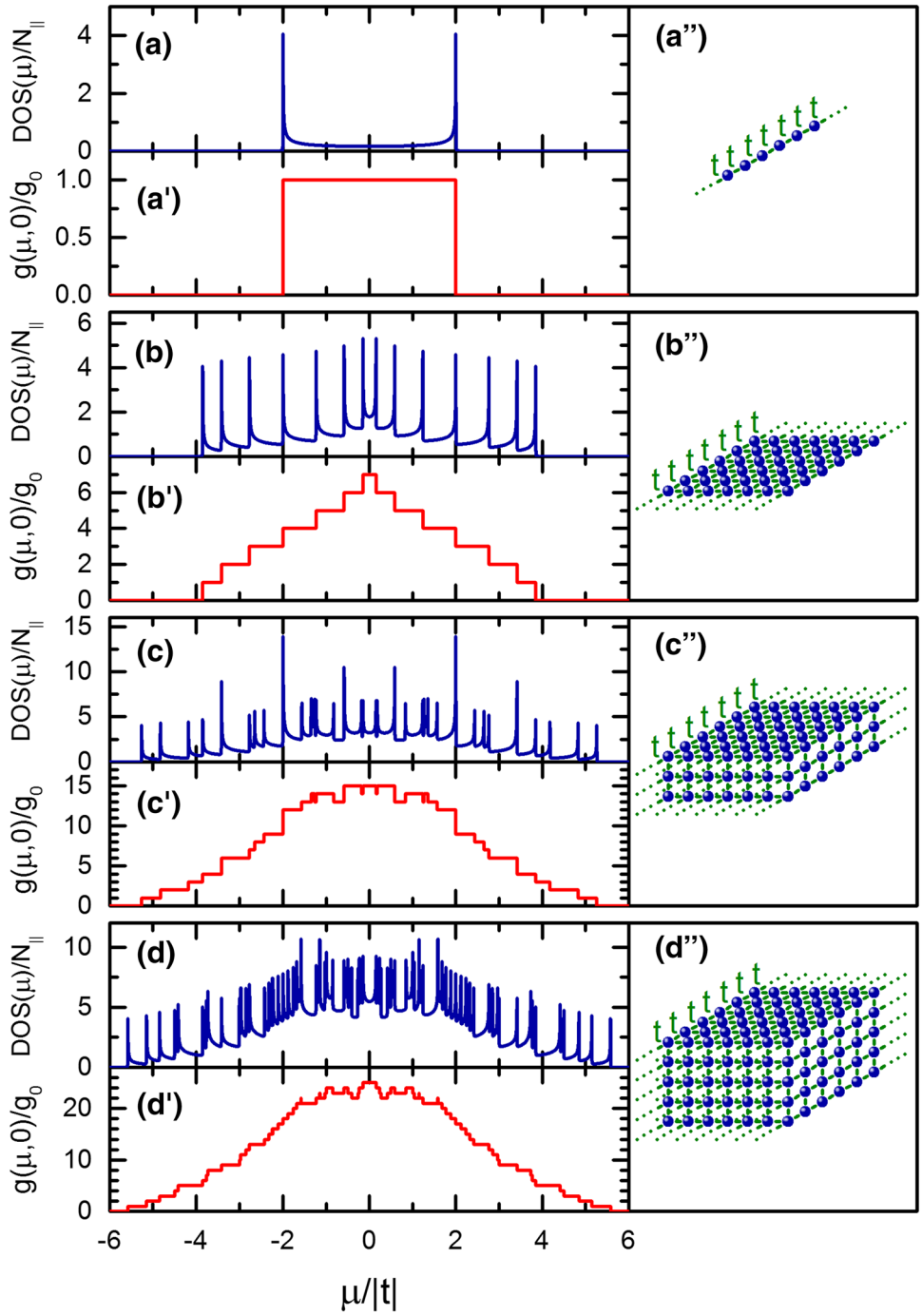

Fig. 1. (a–d) Density of states (DOS) (blue lines) and (a′–d′) zero-temperature electrical conductance (g) (red lines) as functions of chemical potential (μ) for (a, a′) a periodic chain, (b, b′) a periodic nanobelt, and periodic nanowires with cross-sections of (c, c′) 7 × 3 and (d, d′) 7 × 5 atoms, whose structure sketches are, respectively, shown in (a″–d″) (Color figure online).

their locations go away from the band edge when the temperature increases.

Figure 3 exhibit thermoelectric properties obtained from the same nanobelt and nanowires of Fig. 2, now versus the temperature (T). Observe the metallic (blue triangles) and semiconducting (magenta circles) behaviors of the electrical conductivity (σ), when the chemical potential (μ) is, respectively, placed inside ($\mu_{\text{in}} = E_{\text{c}} + 0.01|t|$) and outside ($\mu_{\text{out}} = E_{\text{c}} - 0.01|t|$) the electronic band. In fact, the thermal conductivity by electrons (κ_{el}) is related to σ through the Wiedemann-Franz law given by $\kappa_{\text{el}} = \pi^2 k_{\text{B}}^2 \sigma T/(3e^2)$ when $\mu = \mu_{\text{in}}$. Furthermore, the thermal conductivity by phonons (κ_{ph})

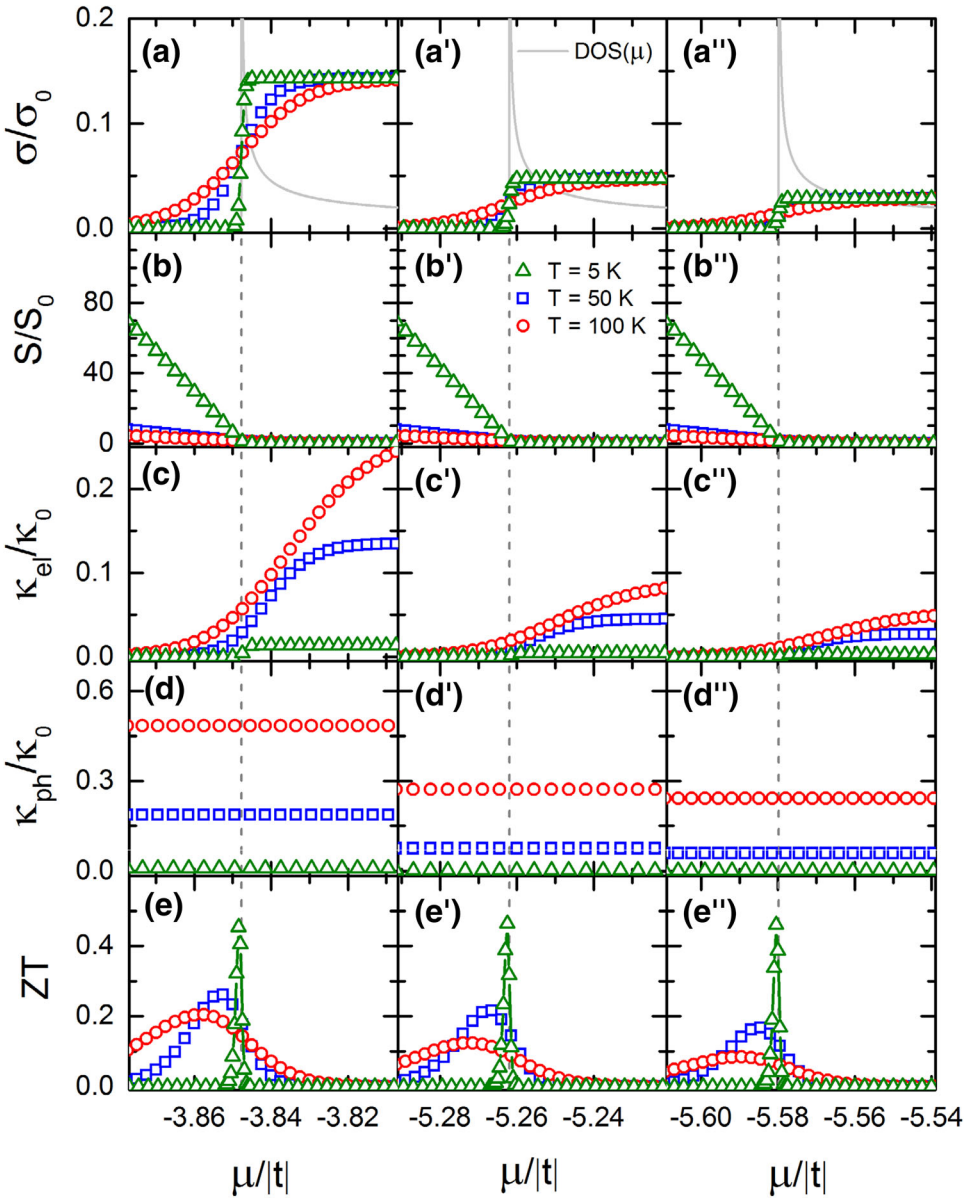

Fig. 2. (a, a′, a″) Density of states (DOS) and electrical conductivity (σ), (b, b′, b″) Seebeck coefficient (S), (c, c′, c″) thermal conductivity by electrons (κ_{el}), (d, d′, d″) thermal conductivity by phonons (κ_{ph}), and (e, e′, e″) figure-of-merit (ZT) as functions of chemical potential (μ) for periodic nanobelt and nanowires with cross-sections of (a–e) 7 × 1, (a′–e′) 7 × 3, and (a″–e″) 7 × 5 atoms.

grows with T, the Seebeck coefficient (S) decreases with T, and the maxima of ZT in the temperature space diminish with the growth of cross-section area, when $\mu = \mu_{out}$.

SEGMENTED NANOWIRES

In this section, we study segmented nanobelts and nanowires with two types of blocks, A and B, which can be periodic or quasiperiodically arranged, as respectively shown in Fig. 4a–d and a′–d′. For the quasiperiodic case, these blocks are ordered following the Fibonacci sequence (F) defined by the addition rule given by $F(n) = F(n-1) \oplus F(n-2)$, where n is the generation number and $\oplus$ indicates the catenation process. If $F(1) = A$ and $F(2) = AB$, the Fibonacci chain of generation four is $F(4) = ABAAB$.

For this study, we chose blocks of three bonds, which can be characterized by hopping integrals (t_A, t_B) or by central (α_A, α_B) and non-central (β_A, β_B) restoring force constants, when the electronic or phononic transport is addressed. The studied nanobelts and nanowires have inhomogeneous cross-sections with non-constant hopping integrals (t_n^x and t_n^y) placed in such a way that maintains the mirror

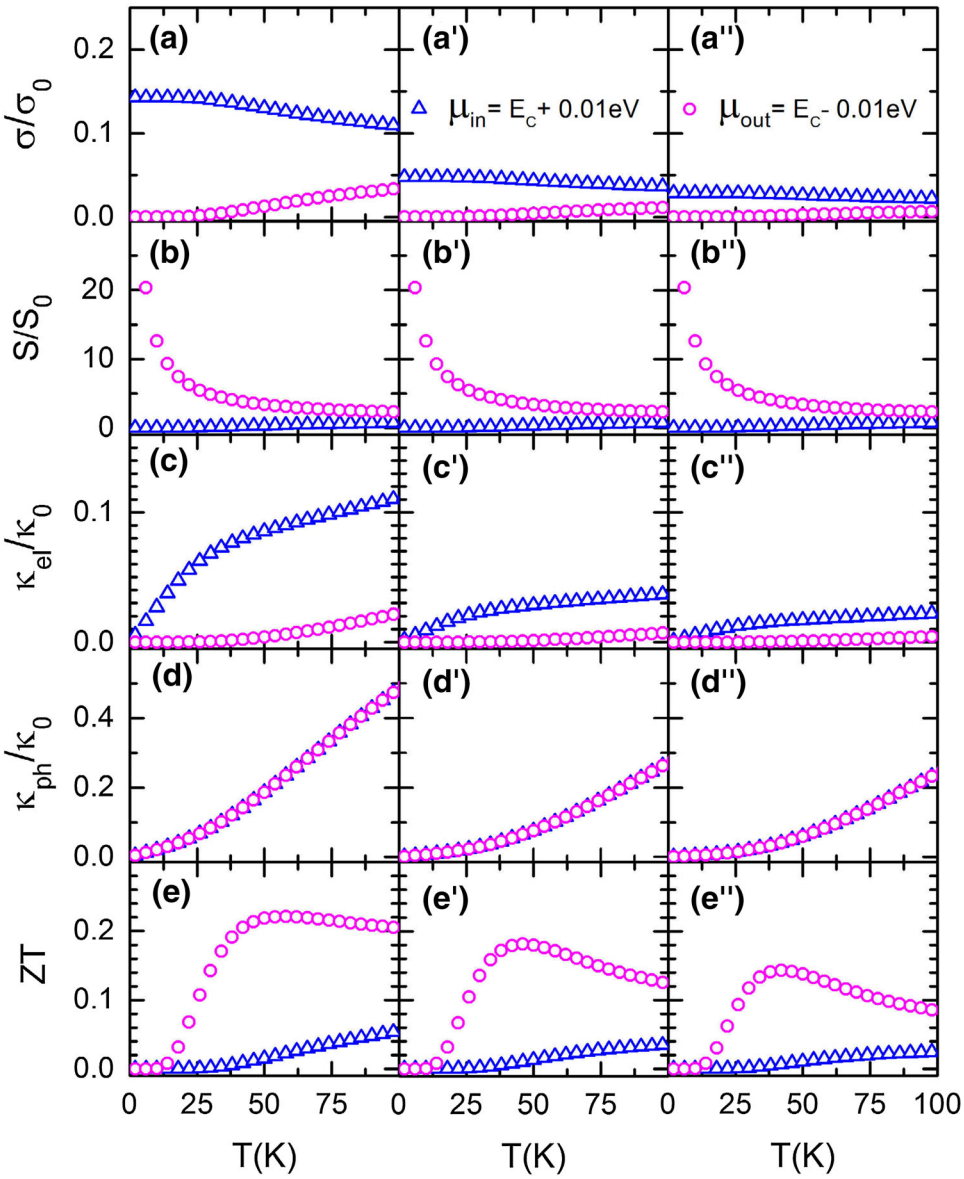

Fig. 3. Temperature (T) dependence of (a, a′, a″) electrical conductivity (σ), (b, b′, b″) Seebeck coefficient (S), (c, c′, c″) thermal conductivity by electrons (κ_{el}), (d, d′, d″) thermal conductivity by phonons (κ_{ph}), and (e, e′, e″) figure-of-merit (ZT) for periodic nanobelt and nanowires with cross-sections of (a–e) 7 × 1, (a′–e′) 7 × 3, and (a″–e″) 7 × 5 atoms.

symmetry along both x and y directions, as illustrated in Fig. 4.

Figure 5 shows the electronic density of states (DOS) (blue lines) and the zero-temperature electrical conductance (g) (red lines) versus the chemical potential (μ) for (a–d) periodically and (a′–d′) quasiperiodically segmented (a, a′) single chains, (b, b′) nanobelts with cross-section of 7 × 1 atoms, and nanowires with cross-sections of (c, c′) 7 × 3 and (d, d′) 7 × 5 atoms, whose atomic ordering is sketched in Fig. 4. The numerical calculations were performed by taking $t_A = 0.3t$, $t_B = t$, $\alpha_A = 0.3\alpha$, $\alpha_B = \alpha$, $\beta_A = 0.3\beta$, $\beta_B = \beta$ and a uniform atomic mass $M = 4.81381 \times 10^{-26}$ kg, where $t = -1$ eV is the hopping integral, $\alpha = 100$ N/m and $\beta = 20$ N/m are, respectively, central and non-central restoring force constants of the periodic leads.

The analyzed nanobelts and nanowires in Fig. 5 have a inhomogeneous cross-section, whose atoms are connected by hopping integrals $t_j^v = c_j^v t$, central $\alpha_j^v = c_j^v \alpha$ and non-central $\beta_j^v = c_j^v \beta$ restoring force constants, where $j = 1$, 2, or 3 and $v = x$ or y with $c_1^x = 1.249$, $c_2^x = 0.855$, $c_3^x = 0.579$, $c_1^y = 0.365$, $c_2^y = 0.517$, and $c_3^y = 0.632$. The periodically segmented nanostructures have a length of $N_{\|} = 100663297$ atoms and quasiperiodic ones have a length of $N_{\|} = 117264509$ atoms corresponding to generation $n = 36$. Notice the multiband structure in Fig. 5a–d, which are related to the periodic

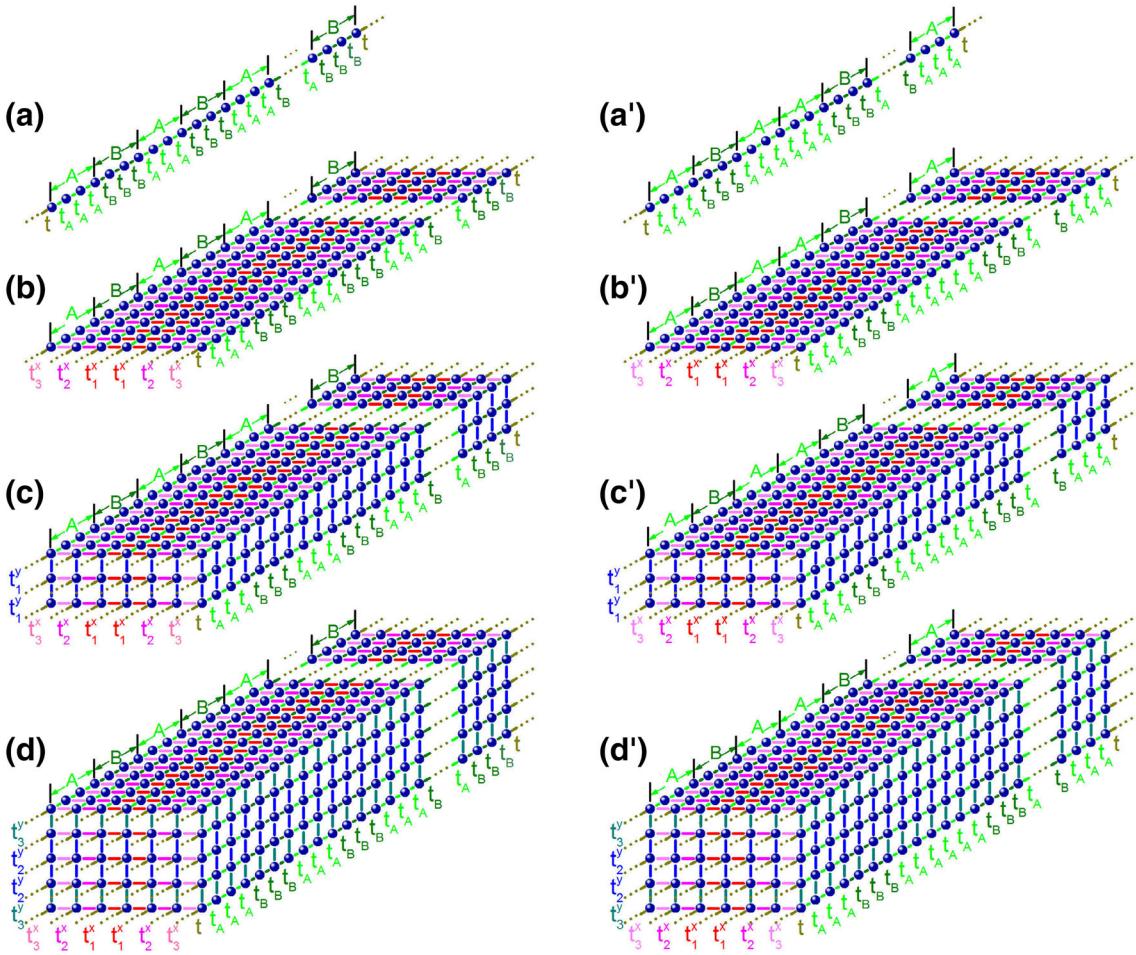

Fig. 4. Schematic representation of (a–d) periodic and (a′–d′) quasiperiodically segmented nanostructures, being (a, a′) single chains, (b, b′) nanobelts with cross-section of 7×1 atoms, (c, c′) and (d, d′) nanowires with cross-sections of 7×3 and 7×5 atoms, respectively. Both segments, *A* and *B*, contain three bonds characterized by hopping integrals t_A or t_B. The cross-sections have non-constant hopping integrals distributed by keeping the mirror symmetry.

segmentation. For example, there are six electronic bands in Fig. 5a, which is originated by folding the first Brillouin zone of a non-segmented linear chain with a new lattice constant $\tilde{a} = 6a$.[23] Moreover, the values of hopping integral in the cross-section were chosen in order to preserve true band gaps around the spectrum center ($\mu = 0$) in Fig. 5b–d. For the quasiperiodic case, at the spectrum center of Fig. 5a′ there is a narrow band containing a transparent state[24] surrounded by two band gaps, and such feature is almost preserved in Fig. 5b′–d′. In general, the conductance peaks of quasiperiodic systems are smaller than those of periodic ones, due to the absence of translational symmetry. However, this reduction of electrical conductance does not necessarily imply a worse thermoelectric efficiency.

In Fig. 6, we show (a, a′, a″) the density of states (DOS) (gray lines) and electrical conductivity (σ), (b, b′, b″) Seebeck coefficient (S), (c, c′, c″) thermal conductivity by electrons (κ_{el}), (d, d′, d″) lattice thermal conductivity (κ_{ph}), and (e, e′, e″) ZT as functions of chemical potential (μ) for the same periodically segmented (a–e) nanobelts and nanowires with cross-sections of (a′–e′) 7 × 3 and (a″–e″) 7 × 5 atoms as in Fig. 5, at temperatures of 5 K (green triangles), 50 K (blue squares) and 100 K (red circles). The dashed lines in these figures indicate the electronic band edges.

Notice that in Fig. 6 the values of σ, S and κ_{el} are unchanged when the cross-section area grows, in contrast to the clear reduction of κ_{ph}, as occurred in Fig. 2a–a″, c–c″ and d–d″ for periodic nanobelts and nanowires without segmentation. These collective behavior leads to an increase of the maximum values of ZT when the cross-section area goes up. These maxima are located out of the electronic band and approach to the band edge located at $E_c = -0.348652$ eV when the temperature diminishes.

Figure 7 exhibit the thermoelectric properties versus temperature (T) for the same nanobelts and nanowires analyzed in Fig. 6. The chemical

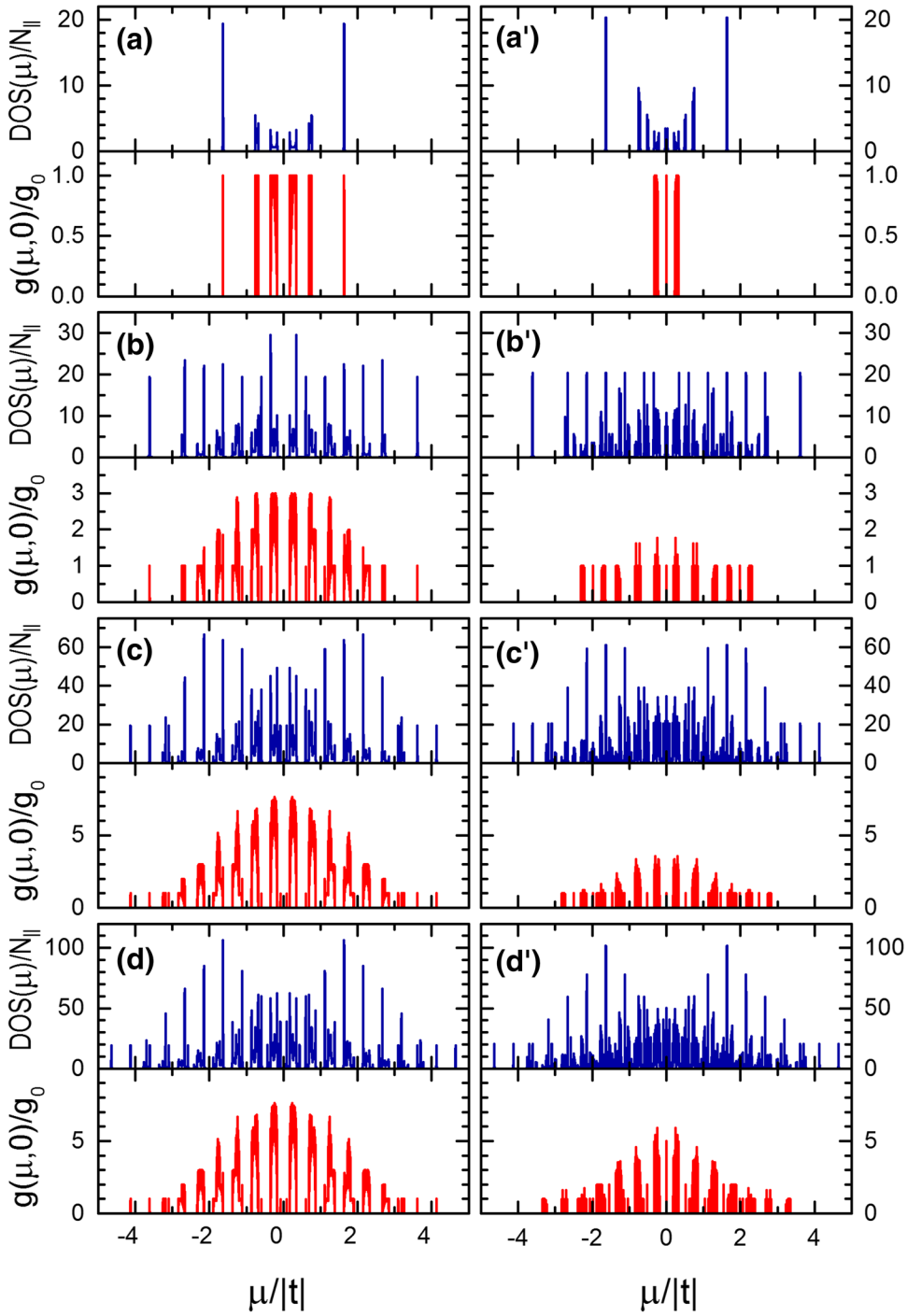

Fig. 5. Density of states (DOS) (blue lines) and zero-temperature electrical conductance (g) (red lines) versus chemical potential (μ) for (a–d) periodic and (a′–d′) quasiperiodically segmented (a, a′) single chains, (b, b′) nanobelts with a cross-section of 7 × 1 atoms, and nanowires with cross-sections of (c, c′) 7 × 3 and (d, d′) 7 × 5 atoms (Color figure online).

potentials (μ) were chosen for $\mu_{in} = E_c + 0.01$ eV (blue triangles) and $\mu_{out} = E_c + 0.01$ eV (magenta circles) for the same band edge of Fig. 6. Notice the growth of ZT from 0.2 of Fig. 3 to almost unity and its enhancement with the cross-section area, when the segmentation and inhomogeneous cross-section are introduced, in spite of the qualitative likeness between Figs. 3 and 7.

In Fig. 8, the same thermoelectric properties of Fig. 6 are exhibited as functions of the chemical potential (μ) for quasiperiodically segmented (a–e) nanobelts and nanowires with cross-sections of (a′–e′) 7 × 3 and (a″–e″) 7 × 5 atoms sketched in Fig. 4b′–d′. The analyzed band edge is located at $E_c = -0.33234$ eV. Observe the fluctuation of the electrical conductivity (σ) at 5 K around

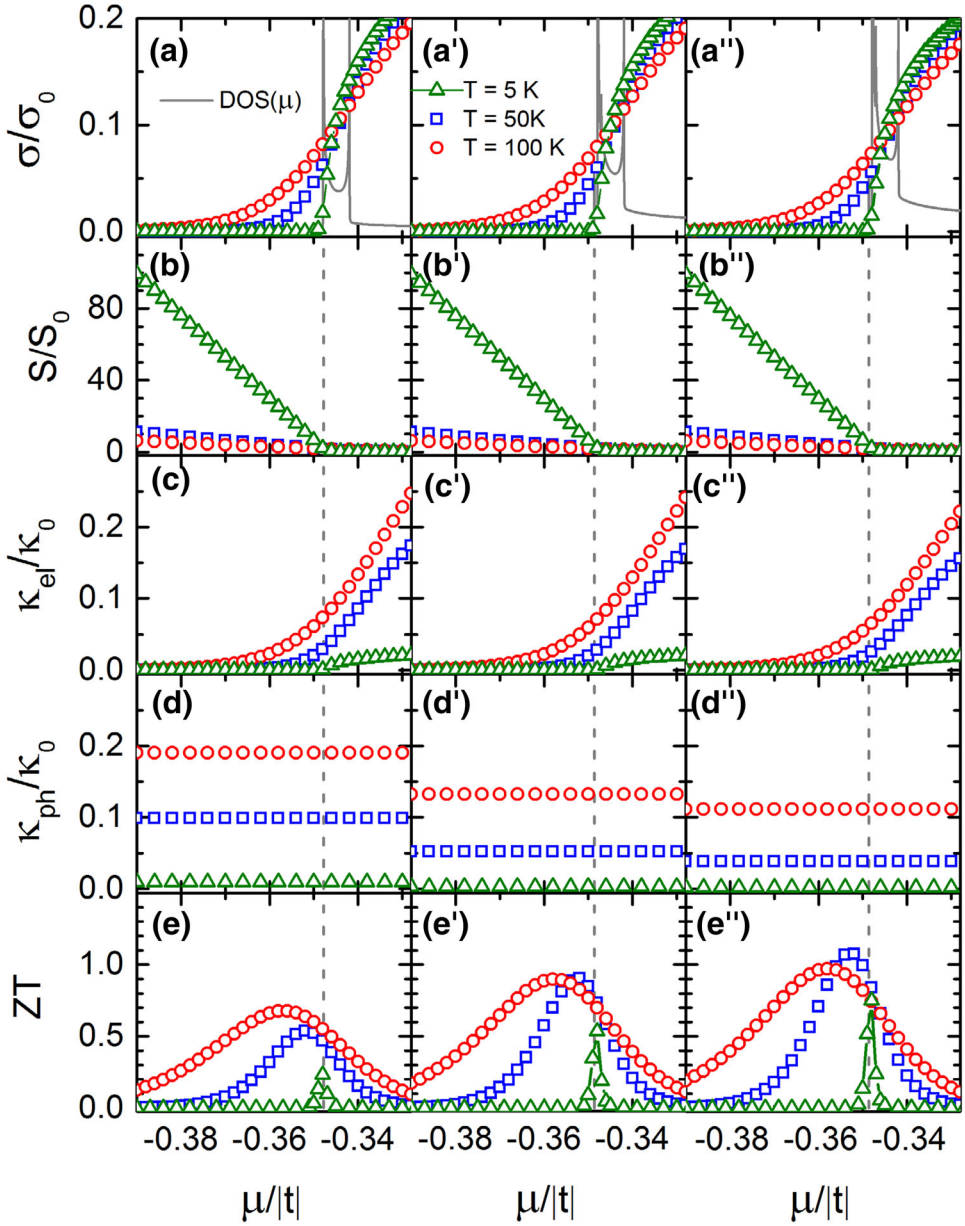

Fig. 6. (a, a′, a″) Density of states (DOS) and electrical conductivity (σ), (b, b′, b″) Seebeck coefficient (S), thermal conductivities by (c, c′, c″) electrons (κ_{el}) and (d, d′, d″) phonons (κ_{ph}), and (e, e′, e″) figure-of-merit (ZT) as functions of chemical potential (μ) for periodically segmented nanobelts and nanowires with inhomogeneous cross-sections of (a–e) 7 × 1, (a′–e′) 7 × 3, and (a″–e″) 7 × 5 atoms.

$\mu = -0.32$ eV, consistent with the density of states spectra (solid gray lines). These fluctuations caused by a dense distribution of bands and gaps smooth out as the temperature grows. Moreover, we note an additional increase of 20% in the maximum ZT at 100 K, mainly due to the reduction of thermal conductivities.

Figure 9 show the temperature dependence of thermoelectric properties corresponding to quasiperiodically segmented nanostructures of Fig. 8. The analyzed chemical potentials (μ) were $\mu_{in} = E_c + 0.01$ eV (blue triangles) and $\mu_{out} = E_c - 0.01$ eV (magenta circles) with $E_c = -0.33234$ eV. In contrast to Fig. 7, ZT for μ_{in} is close to that for μ_{out}, raised from a neither metallic nor semiconductor temperature dependence of σ. Also, we observe an almost linear growth of ZT with temperature around 100 K, which suggests a possible larger ZT close to the room temperature.

ANALYSIS OF PARAMETER DEPENDENCE

There are essentially four parameters in the electronic and vibrational Hamiltonians of periodic

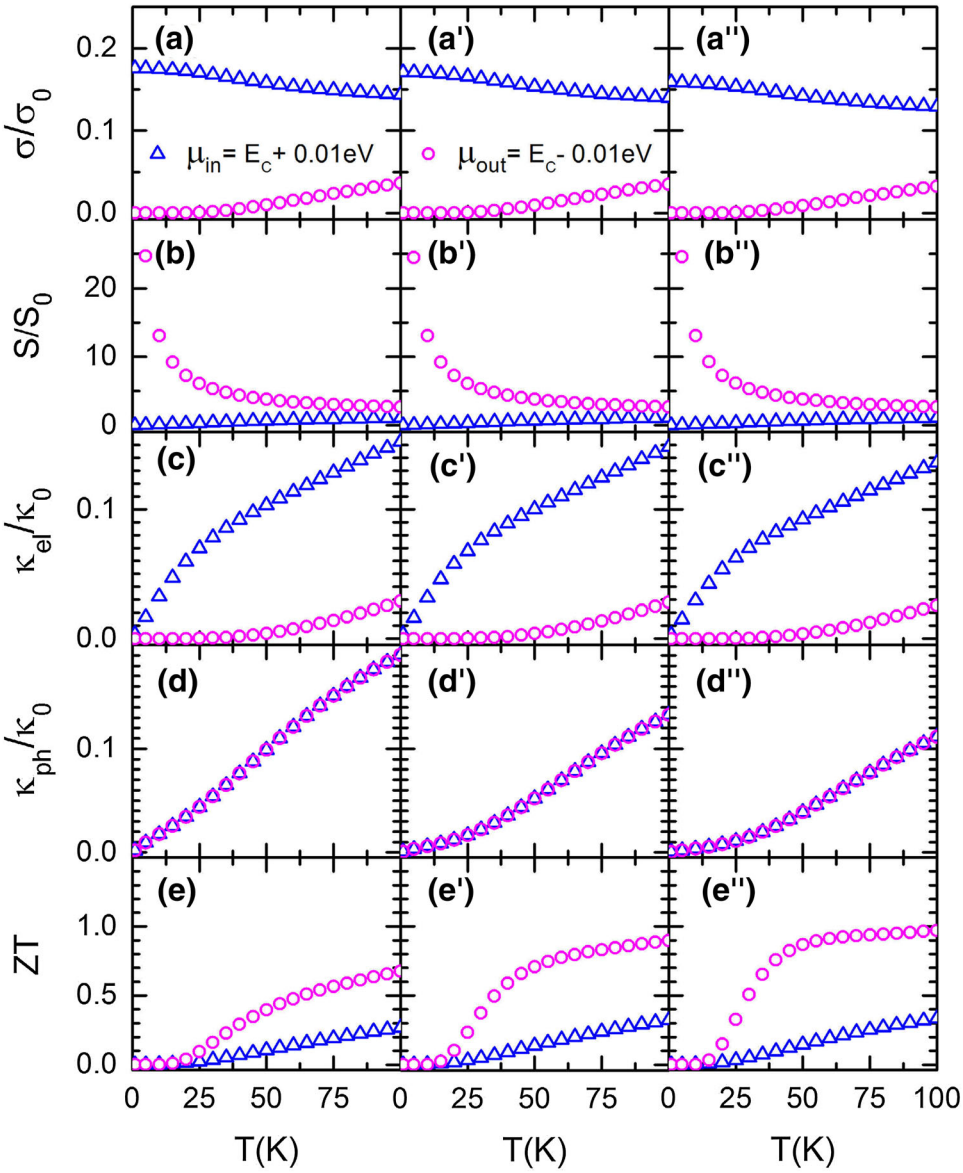

Fig. 7. Temperature (T) dependence of (a, a′, a″) electrical conductivity (σ), (b, b′, b″) Seebeck coefficient (S), thermal conductivities by (c, c′, c″) electrons (κ_{el}) and (d, d′, d″) phonons (κ_{ph}), and (e, e′, e″) figure-of-merit (ZT) for periodically segmented nanobelt and nanowires with cross-sections of (a–e) 7 × 1, (a′–e′) 7 × 3, and (a″–e″) 7 × 5 atoms.

systems and they are the hopping integral (t), atomic mass (M), central (α) and non-central (β) restoring force constants. Actually, the results only depend on two normalized ones $\hbar\omega_\alpha/|t|$ and $\hbar\omega_\beta/|t|$, where $\omega_\alpha = \sqrt{\alpha/M}$ and $\omega_\beta = \sqrt{\beta/M}$. In Fig. 10, the room-temperature (T = 300 K) thermoelectric ZT is plotted as a function of these normalized parameters for t_A/t_B = 1, 0.5, and 0.3. In the last two cases, quasiperiodically segmented nanowires with cross-section of 7 × 5 atoms are considered, as in Fig. 8. Notice a general enhancement of ZT in Fig. 10 with the quasiperiodicity strength, i.e., ZT grows when the ratio t_A/t_B moves away from the periodic case with t_A/t_B = 1, and a similar dependence of ZT on $\hbar\omega_\alpha/|t|$ and $\hbar\omega_\beta/|t|$ for the three analyzed cases. Observe also the existence of two maximums of ZT located at $\hbar\omega_\alpha \approx \hbar\omega_\beta \to 0$ and at $\hbar\omega_\alpha \approx \hbar\omega_\beta \approx 0.1|t|$ for each value of t_A/t_B, where the first one is due to the vanish of lattice thermal conductivity. The second maximum of ZT at $\hbar\omega_\alpha \approx \hbar\omega_\beta \approx 0.1|t|$ is originated from the increase of the vibrational band width when $\hbar\omega_\alpha$ and $\hbar\omega_\beta$ grow, whose phononic $\mathrm{DOS}(\omega^2)$ and $\mathrm{Tr}\left\{A_x\tilde{G}_{ph}(\omega^2)A_x\tilde{G}_{ph}(\omega^2)\right\}_l$ for the periodic case are similar to those shown in Fig. 1d.[22] In other words, the growth of $\hbar\omega_\alpha$ and $\hbar\omega_\beta$ leads to a

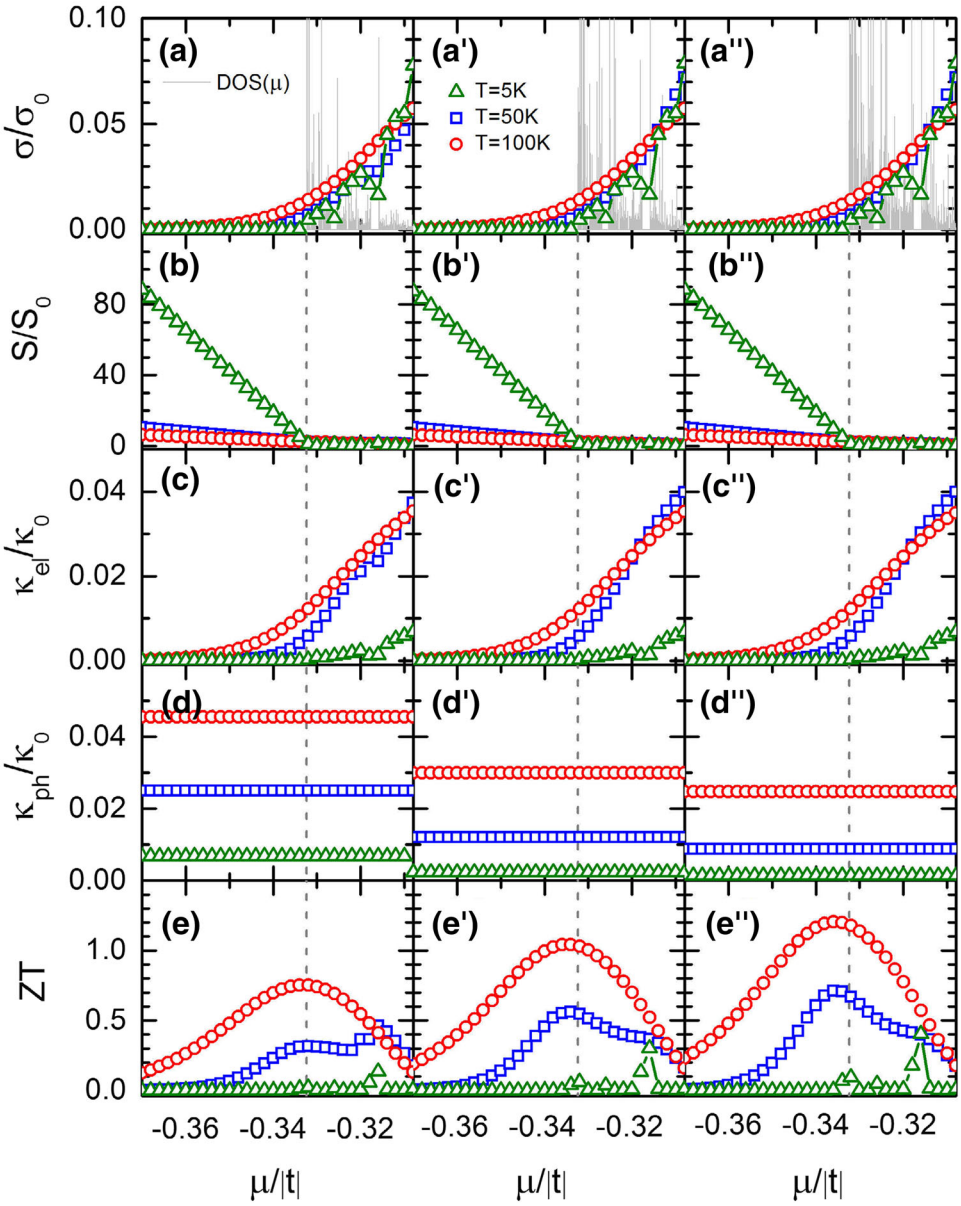

Fig. 8. (a, a′, a″). Density of states (DOS) and electrical conductivity (σ), (b, b′, b″) Seebeck coefficient (S), (c, c′, c″) thermal conductivity by electrons (κ_{el}), (d, d′, d″) thermal conductivity by phonons (κ_{ph}), and (e, e′, e″) figure-of-merit (ZT) as functions of chemical potential (μ) for quasiperiodically segmented nanobelts and nanowires with inhomogeneous cross-sections of (a–e) 7 × 1, (a′–e′) 7 × 3, and (a″–e″) 7 × 5 atoms.

shift of the maximum of both phononic DOS and $\mathrm{Tr}\left\{A_x\tilde{G}_{ph}(\omega^2)A_x\tilde{G}_{ph}(\omega^2)\right\}_l$ toward high frequency and then, for a fixed temperature the Bose–Einstein distribution in Eq. 6 will cover a smaller portion of three-dimensional phonon band. In consequence, a minor lattice thermal conductivity and a larger ZT.

Moreover, Fig. 10 shows an asymmetrical dependence of ZT on $\hbar\omega_\alpha$ and on $\hbar\omega_\beta$, since for both longitudinal and transversal vibration modes the non-central first-neighbor interactions (β) has a double contribution to the lattice thermal conductivity than the central one (α) within the Born model. It would be worth stressing that the results of ZT presented in the previous sections correspond to two specific points of $\hbar\omega_\alpha = 0.03|t|$ and $\hbar\omega_\beta = 0.0134|t|$ on the surfaces of $t_A/t_B = 1$ and $t_A/t_B = 0.3$ in Fig. 10. Hence, the enhancement of ZT through the quasiperiodicity seems to be general and independent of the Hamiltonian parameters chosen.

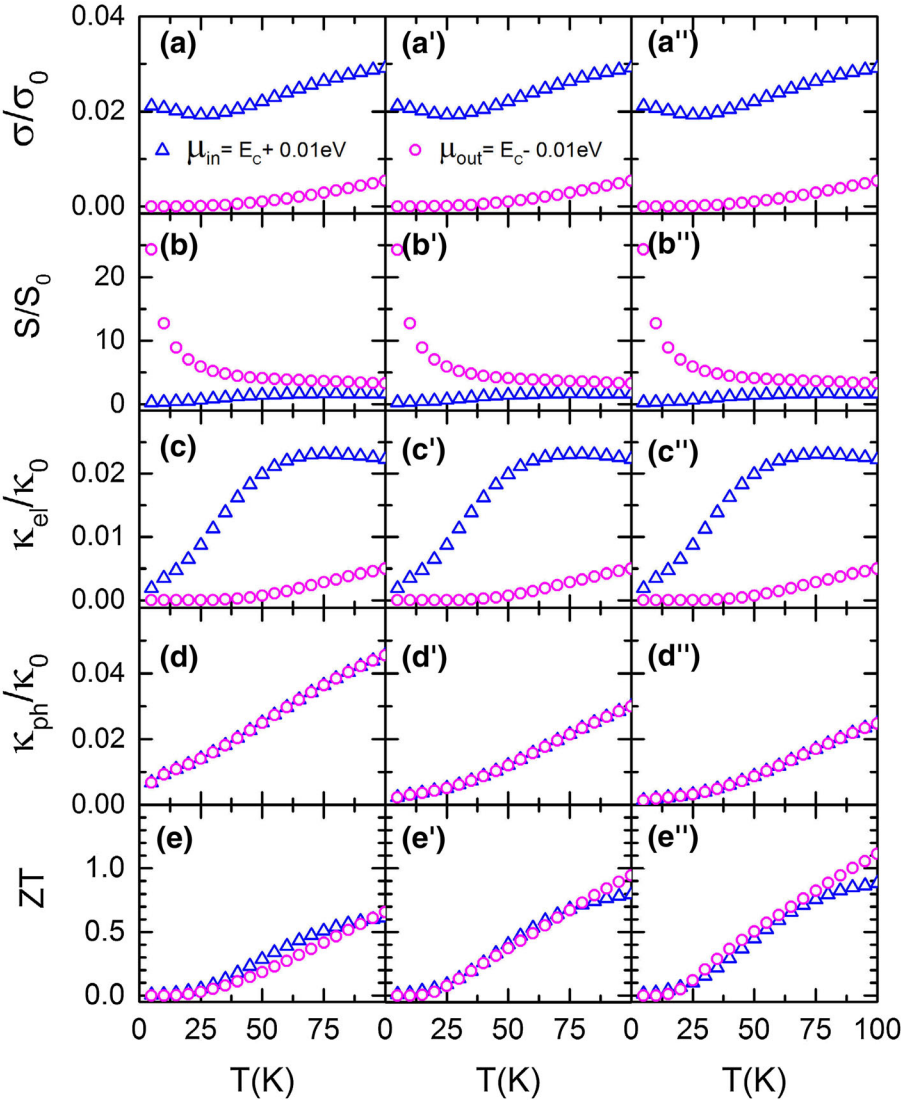

Fig. 9. Temperature (T) dependence of (a, a′, a″) electrical conductivity (σ), (b, b′, b″) Seebeck coefficient (S), (c, c′, c″) thermal conductivity by electrons (κ_{el}), (d, d′, d″) thermal conductivity by phonons (κ_{ph}), and (e, e′, e″) figure-of-merit (ZT) for quasiperiodically segmented nanobelts and nanowires with inhomogeneous cross-sections of (a–e) 7 × 1, (a′–e′) 7 × 3, and (a″–e″) 7 × 5 atoms.

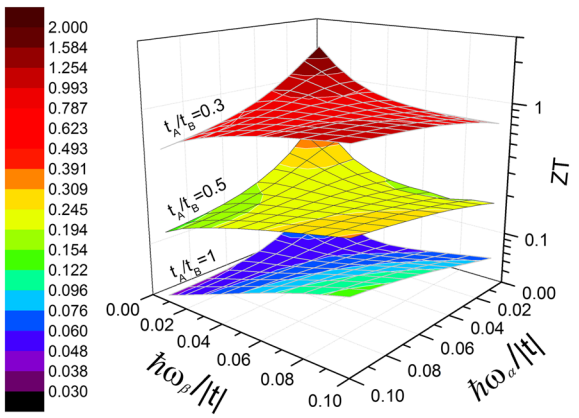

Fig. 10. Thermoelectric figure-of-merit (ZT) at 300 K as a function of normalized Hamiltonian parameters $\hbar\omega_\alpha/|t|$ and $\hbar\omega_\beta/|t|$, for a periodic nanowire with $t_A/t_B = 1$ and quasiperiodically segmented nanowires with $t_A/t_B = 0.5$ and 0.3. All these nanowires have a cross-section of 7 × 5 atoms, as in Fig. 8.

CONCLUSIONS

The effects of structural inhomogeneity on the thermoelectric properties of nanobelt and nanowires with macroscopic length are analyzed by means of a real-space renormalization plus convolution method. The results reveal a clear increase of the thermoelectric figure-of-merit (ZT) when the segmentation is introduced, in accordance with experimental data.[10] In fact, the quasiperiodicity significantly diminishes the thermal conduction of long wavelength acoustic phonons, which are responsible of the phononic conductivity at low temperature, and it is not easy to block their transmission since they do not feel local defects nor impurities. Contrary to periodic nanowires, there is no reduction of ZT when the cross-section area grows. In summary, the results of this work

suggest the possibility of optimizing the thermoelectricity through the inhomogeneity under design.

This analysis was carried out by means of semi-empirical models applied to cubically structured nanowires with a specific set of parameters. However, its main result of the possibility to improve ZT by introducing long-range inhomogeneity into nanowires could not depend on the parameters chosen as shown in "Analysis of Parameter Dependence", and it would be useful in the design and fabrication of efficient thermoelectric devices, as suggested by the results of $M_2O_3(ZnO)_n$ (M = In, Ga, Fe) segmented nanowires.[10]

ACKNOWLEDGEMENTS

This work has been partially supported by Consejo Nacional de Ciencia y Tecnología de México, Project 252943, and by Programa de Apoyo a Proyectos de Investigación e Innovación Tecnológica of Universidad Nacional Autónoma de México (UNAM) through Projects IN113714 and IN114916. Computations were performed at Miztli of Dirección General de Cómputo y de Tecnologías de Información y Comunicación of UNAM, where technical assistance of Silvia E. Frausto del Río and José Luis Gordillo is fully appreciated.

REFERENCES

1. T.M. Tritt, eds., *Thermal Conductivity—Theory, Properties and Applications* (New York: Kluwer Academic-Plenum, 2004), p. 3.
2. J. Kim, J.H. Bahk, J. Hwang, H. Kim, H. Park, and W. Kim, *Phys. Status Solidi RRL* 7, 767 (2013).
3. G.J. Snyder and E.S. Toberer, *Nat. Mater.* 7, 105 (2008).
4. P. Mensch, S. Karg, V. Schmidt, B. Gotsmann, H. Schmid, and H. Riel, *Appl. Phys. Lett.* 106, 093101 (2015).
5. S. Bäßler, T. Böhnert, J. Gooth, C. Schumacher, E. Pippel, and K. Nielsch, *Nanotechnology* 24, 495402 (2013).
6. Z.M. Gibbs, H.-S. Kim, H. Wang, and J. Snyder, *Appl. Phys. Lett.* 106, 022112 (2015).
7. J.E. Cornett and O. Rabin, *Phys. Rev. B* 84, 205410 (2011).
8. J. Kim, S. Lee, Y. Brovman, P. Kim, and W. Lee, *Nanoscale* 7, 5053 (2015).
9. J. Kang, W. Shim, S. Lee, J.W. Roh, J.S. Noh, P.W. Voorhees, and W. Lee, *J. Mater. Chem. A* 1, 2395 (2013).
10. S.C. Andrews, M.A. Fardy, M.C. Moore, S. Aloni, M. Zhang, V. Radmilovic, and P. Yang, *Chem. Sci.* 2, 706 (2011).
11. A. Süto, *J. Stat. Phys.* 56, 525 (1989).
12. M. Kohmoto and B. Sutherland, *Phys. Rev. B* 35, 1020 (1987).
13. P.Y. Yu and M. Cardona, *Fundamentals of Semiconductors Physics and Materials Properties*, 4th ed. (Berlin: Springer, 2010), p. 83.
14. C. Wang and R.A. Barrio, *Phys. Rev. Lett.* 61, 191 (1988).
15. P. Alfaro, R. Cisneros, M. Bizarro, M. Cruz-Irisson, and C. Wang, *Nanoscale* 3, 1246 (2011).
16. T. Markussen, *Nano Lett.* 12, 4698 (2012).
17. B. Kramer and A. MacKinon, *Rep. Prog. Phys.* 56, 1469 (1993).
18. E.N. Economou, *Green's Functions in Quantum Physics*, 3rd ed. (Berlin: Springer, 2006), p. 6.
19. J.K. Flicker and P.L. Leath, *Phys. Rev. B* 7, 2296 (1973).
20. R.J. Elliott, J.A. Krumhansl, and P.L. Leath, *Rev. Mod. Phys.* 46, 465 (1974).
21. V. Sánchez and C. Wang, *Phys. Rev. B* 70, 144207 (2004).
22. C. Wang, F. Salazar, and V. Sánchez, *Nano Lett.* 8, 4205 (2008).
23. A.P. Sutton, *Electronic Structure of Materials* (Oxford: Oxford University Press, 1993), p. 109.
24. C. Wang, C. Ramírez, F. Sánchez, and V. Sánchez, *Phys. Status Solidi B* 252, 1370 (2015).

MRS Advances

http://journals.cambridge.org/ADV

Additional services for ***MRS Advances:***

Email alerts: Click here
Subscriptions: Click here
Commercial reprints: Click here
Terms of use : Click here

Thermoelectricity in periodic and quasiperiodically segmented nanobelts and nanowires

J. Eduardo Gonzalez, Vicenta Sanchez and Chumin Wang

MRS Advances / *FirstView* Article / June 2016, pp 1 - 6
DOI: 10.1557/adv.2016.291, Published online: 02 May 2016

Link to this article: http://journals.cambridge.org/abstract_S2059852116002917

How to cite this article:
J. Eduardo Gonzalez, Vicenta Sanchez and Chumin Wang Thermoelectricity in periodic and quasiperiodically segmented nanobelts and nanowires. MRS Advances, Available on CJO 2016 doi:10.1557/adv.2016.291

Request Permissions : Click here

CAMBRIDGE JOURNALS

Downloaded from http://journals.cambridge.org/ADV, IP address: 132.248.12.16 on 15 Jun 2016

MRS Advances © 2016 Materials Research Society
DOI: 10.1557/adv.2016.291

Thermoelectricity in periodic and quasiperiodically segmented nanobelts and nanowires

J. Eduardo Gonzalez[1], Vicenta Sanchez[2], and Chumin Wang[1]
[1]*Instituto de Investigaciones en Materiales, Universidad Nacional Autonoma de Mexico, D.F., Mexico.*
[2]*Departamento de Fisica, Facultad de Ciencias, Universidad Nacional Autonoma de Mexico, D.F., Mexico*.

ABSTRACT

Thermoelectric properties of segmented nanowires and nanobelts are studied by means of the Kubo-Greenwood formula and a real-space renormalization plus convolution method. The tight-binding and Born models are respectively used for the calculation of electronic and lattice thermal conductivities. In particular, we investigate the thermoelectric figure of merit (*ZT*) of periodic and quasiperiodically segmented nanowires with two different cross sections, where the segments of the quasiperiodic one are ordered following the Fibonacci sequence. The results show an increase of *ZT* when the cross section area of nanowires diminishes. In addition, we present results of *ZT* in segmented nanobelts with an inhomogeneous cross section. For both nanowires and nanobelts, the quasiperiodicity seems to be an important enhancing factor of *ZT*.

INTRODUCTION

Energy conversion through thermoelectric devices constitutes a sustainable alternative for the generation of electricity. Their performance can be measured by using the dimensionless figure-of-merit defined as

$$ZT = \sigma S^2 T / (\kappa_{el} + \kappa_{ph}), \quad (1)$$

where S is the Seebeck coefficient, σ is the electrical conductivity, κ_{el} and κ_{ph} are the electronic and phononic thermal conductivities, respectively [1]. The inherent correlation between these thermoelectric quantities makes difficult to improve the value of *ZT*. Recently, nanowire heterostructures, such as M_2O_3/ZnO (M=In, Ga Fe) with compositional segmentation [2], have demonstrated a significant improvement of *ZT*, mainly due to the phonon scattering at composite interfaces. Likewise, nanobelt heterostructures have been made [3] and the power factor (σS^2) of Sb_2Te_3 nanobelts was found larger than the corresponding bulk value [4].

On the theoretical side, thermoelectric properties can be determined by using the Boltzmann equation [5]. For aperiodic nanostructures, the atomic-scale modeling requires innovative approaches, since the long-range structural disorder makes useless the Bloch theorem and reciprocal space. In this article, we report a quantum mechanical study of thermoelectric properties in periodic and quasiperiodically segmented nanowires and nanobelts by means of the Kubo-Greenwood formula and a real-space renormalization plus convolution method [6], which has the advantage of being computational efficient and able to address a macroscopic number of atoms in a non-perturbative way.

THE MODEL

In the Boltzmann formalism, the thermoelectric quantities can be calculated by means of the Kubo-Greenwood formula as [6,7]

CAMBRIDGE JOURNALS
http://journals.cambridge.org Downloaded: 15 Jun 2016 IP address: 132.248.12.16

$\sigma(\mu,T)=e^2L_0(\mu,T)$, $S(\mu,T)=-\dfrac{L_1(\mu,T)}{|e|TL_0(\mu,T)}$, and $\kappa_{el}(\mu,T)=\dfrac{L_2(\mu,T)L_0(\mu,T)-L_1^2(\mu,T)}{TL_0(\mu,T)}$,

where

$$L_n(\mu,T)=\frac{-2\hbar}{\pi m^2\Omega}\int_{-\infty}^{\infty}dE\,(E-\mu)^n\frac{\partial f}{\partial E}Tr\left\{\hat{p}_x\tilde{G}(E)\hat{p}_x\tilde{G}(E)\right\}, \tag{2}$$

Ω is the system volume, $\hat{p}_x$ is the projection of momentum operator along the nanostructure, $f(E)=\{1+\exp[(E-\mu)/(k_BT)]\}^{-1}$ is the Fermi-Dirac distribution with chemical potential μ and temperature *T*, $\tilde{G}(E)=G^+(E)-G^-(E)$ is the discontinuity of Green's functions, being $G^+(E)$ and $G^-(E)$ the retarded and advanced single-electron Green's functions, respectively.

On the other hand, the lattice thermal conductivity (κ_{ph}) can be calculated by using the Kubo-Greenwood formula for phonons given by [8]

$$\kappa_{ph}(T)=\frac{-2\hbar^2}{\pi\Omega k_BT^2}\sum_l\int_0^{\infty}d\omega\frac{\omega^2e^{\hbar\omega/k_BT}}{(e^{\hbar\omega/k_BT}-1)^2}Tr\left\{\mathbf{A}_x\tilde{G}_{ph}(\omega)\mathbf{A}_x\tilde{G}_{ph}(\omega)\right\}_l, \tag{3}$$

where the sum of *l* is over the longitudinal and transversal modes, $\tilde{G}_{ph}(\omega)$ is the discontinuity of phononic Green's functions determined by $(M\omega^2\mathbf{I}-\mathbf{\Phi})\mathbf{G}_{ph}(\omega)=\mathbf{I}$ and the elements of matrix $\mathbf{A}_x$ are $[\mathbf{A}_x]_{\nu\nu'}(l,j)\equiv\frac{1}{2}(\mathbf{R}_l-\mathbf{R}_j)_x\Phi_{\nu\nu'}(l,j)$, being $\Phi_{\nu\nu'}(l,j)=\partial^2V_{lj}/\partial u_\nu(l)\partial u_{\nu'}(j)$ the dynamic matrix. In the Born model [9], $V_{lj}=\frac{1}{2}(\alpha-\beta)\left|[\mathbf{u}(l)-\mathbf{u}(j)]\cdot\hat{\mathbf{n}}_{lj}\right|^2+\frac{1}{2}\beta\left|[\mathbf{u}(l)-\mathbf{u}(j)]\right|^2$ is the interaction potential with central (α) and non-central (β) restoring forces between nearest-neighbor atoms *l* and *j*, whose bond direction is indicated by the unitary vector $\hat{\mathbf{n}}_{lj}$ and displacements from their respective equilibrium positions are $\mathbf{u}(l)$ and $\mathbf{u}(j)$.

Let us consider a single band tight-binding Hamiltonian ($\hat{H}$) with null on-site self-energies given by $\hat{H}=\sum_{\langle l,j\rangle}\left\{t_{l,j}\left|l\right\rangle\left\langle j\right|+t_{j,l}\left|j\right\rangle\left\langle l\right|\right\}$, where $t_{l,j}=t_{j,l}$ is the nearest-neighbor hopping integral. For the sake of simplicity, a uniform bond length (*a*) is taken and $\hat{p}_x=\frac{im}{\hbar}[\hat{H},x]=\frac{ima}{\hbar}\sum_l\left\{t_{l,l+1}\left|l\right\rangle\left\langle l+1\right|-t_{l-1,l}\left|l\right\rangle\left\langle l-1\right|\right\}$. For a cubically structured solid, the Hamiltonian $\hat{H}$ and the dynamic matrix $\mathbf{\Phi}$ are separable, *i.e.*, $\hat{H}=\hat{H}_{\parallel}\otimes\hat{I}_{\perp}+\hat{I}_{\parallel}\otimes\hat{H}_{\perp}$, where $\hat{H}_{\parallel}$ ($\hat{I}_{\parallel}$) and $\hat{H}_{\perp}$ ($\hat{I}_{\perp}$) are Hamiltonians (identity matrices) of the parallel and perpendicular subsystems, respectively. For systems beyond of one dimension, Eqs. (2) and (3) can be rewritten through the convolution theorem as

$$L_n(\mu,T)=\frac{-2\hbar}{\pi m^2\Omega}\int_{-\infty}^{\infty}dE(E-\mu)^n\frac{\partial f}{\partial E}\sum_\lambda Tr\{\hat{p}_x\tilde{G}^{\parallel}(E-E_\lambda)\hat{p}_x\tilde{G}^{\parallel}(E-E_\lambda)\} \tag{4}$$

and

$$\kappa_{ph}(T)=\frac{-2\hbar^2}{\pi\Omega k_BT^2}\sum_{\lambda,l}\int_0^{\infty}d\omega\frac{\omega^2e^{\hbar\omega/k_BT}}{(e^{\hbar\omega/k_BT}-1)^2}Tr\{\mathbf{A}_x\tilde{G}_{ph}^{\parallel}(\omega^2-\omega_\lambda^2)\mathbf{A}_x\tilde{G}_{ph}^{\parallel}(\omega^2-\omega_\lambda^2)\}_l, \tag{5}$$

CAMBRIDGE JOURNALS
http://journals.cambridge.org Downloaded: 15 Jun 2016 IP address: 132.248.12.16

where E_λ and $M\omega_\lambda^2$ are eigenvalues of $\hat{H}_\perp$ and $\mathbf{\Phi}_\perp$, respectively. In this article, we only analyze the bond problem, *i.e.*, nanowires with null self-energies and a constant atomic mass (M).

SEGMENTED NANOWIRES

In this section, we investigate the thermoelectric properties of periodic and quasiperiodically segmented nanowires (SNW), as respectively illustrated in Figures 1(a,b) and 1(a',b') for cross sections of (a,a') 4×4 and (b,b') 9×9 atoms connected by hopping integrals t. These SNW contain two kinds of segments constituted by three bonds with hopping integrals t_A or t_B along the nanowires. For the quasiperiodic case, these segments are ordered following the Fibonacci sequence.

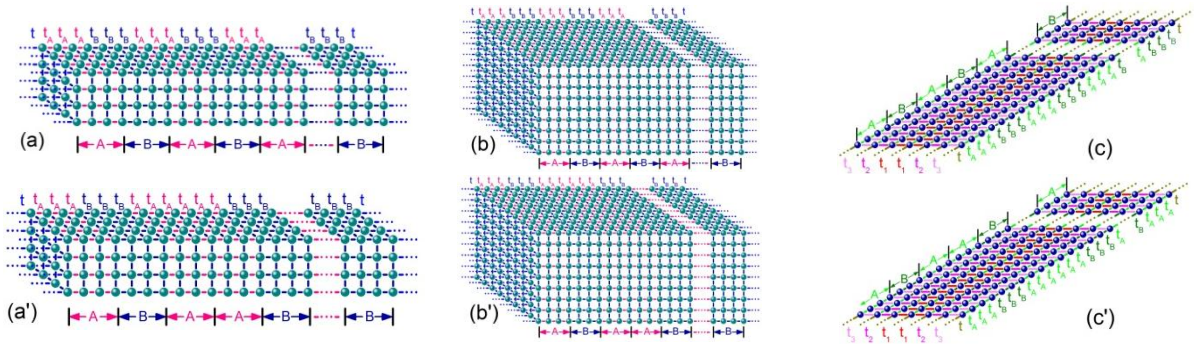

Figure 1. Schematic representations of (a,b,c) periodic and (a',b',c') quasiperiodically segmented nanowires with square cross-sections of (a,a') 4×4 and (b,b') 9×9 atoms and (c,c') nanobelts with a cross section of 7×1 atoms connected by hopping integrals t_1, t_2 and t_3. These nanostructures contain two kinds of segments A and B of three bonds characterized by hopping integrals t_A and t_B, respectively.

In Figures 2, we show (a,a') the electronic density of states $DOS(\mu)=-\frac{1}{\pi}\sum_j \mathrm{Im}[G_j^+(\mu)]$, (b,b') electrical conductance $g(\mu)=\sigma(\mu)\Omega_\perp/\Omega_\square$ normalized by the quantum conductance $g_0=2e^2/h$, (c,c') Seebeck coefficient (S) normalized by $S_0=-k_B/|e|$, (d,d') thermal conductance by electrons $K_{el}=\kappa_{el}(\mu)\Omega_\perp/\Omega_\square$, (e,e') thermal conductance by phonons $K_{ph}=\kappa_{ph}(\mu)\Omega_\perp/\Omega_\square$ in the unity of the thermal quantum conductance $K_0=\pi k_B^2 T/(6\hbar)$, and (f,f') the figure-of-merit (ZT) as functions of the chemical potential (μ) for periodic (blue open circles) and quasiperiodic (red solid circles) SNW with cross sections of (a-f) $\Omega_\perp=9\times9$ and (a'-f') 4×4 atoms at a temperature of 25 K. The numerical calculations were carried out by taking $t_A=0.5t$, $t_B=t$, $\alpha_A=0.5\alpha$, $\alpha_B=\alpha$, $\beta_A=0.5\beta$, $\beta_B=\beta$ and $M=4.81381\times10^{-26}kg$, where $t=-1eV$ is the hopping integral, $\alpha=100\,N/m$ and $\beta=20\,N/m$ are respectively central and non-central restoring force constants of the periodic leads. The periodic SNW have a length of 402653185 atoms and the quasiperiodic ones possess a length of 953434 atoms. All the nanostructures analyzed in this paper are connected to two semi-infinite periodic leads with null self-energies, hopping integrals t, central α and non-central β restoring force constants. Note in Figures 2(a,a') that both periodic and quasiperiodic SNW have the same electronic band edges (E_c) at $E_c=-4.236|t|$ for SNW of

CAMBRIDGE JOURNALS
http://journals.cambridge.org Downloaded: 15 Jun 2016 IP address: 132.248.12.16

Figures 1(a,a') and at $E_c = -4.8043|t|$ for SNW of Figures 1(b,b'), where maximum *ZT* are located. Moreover, quasiperiodic SNW have lower electronic and phononic conductance than those of periodic ones, which leads to a larger *ZT* in quasiperiodic SNW than that of periodic ones.

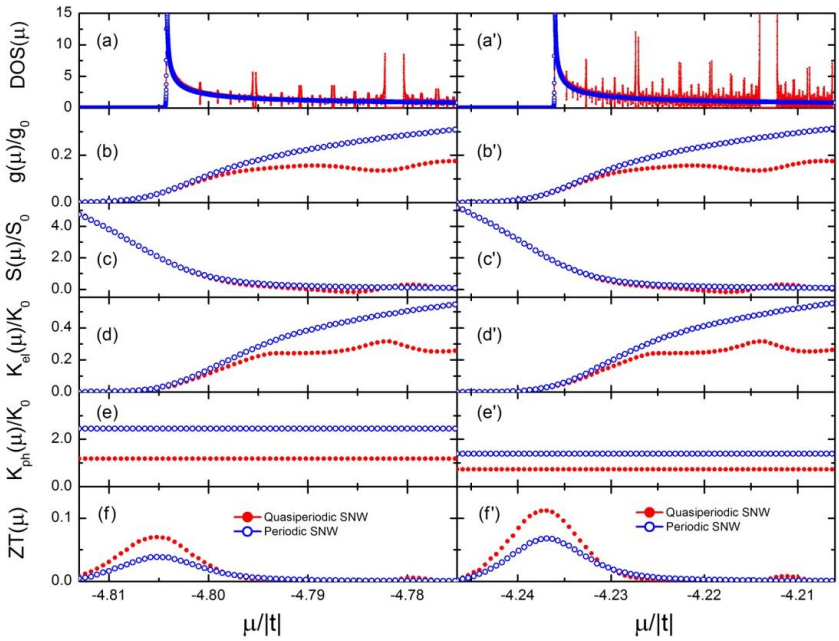

Figure 2. Chemical potential (μ) dependence of (a,a') Density of states (*DOS*), (b,b') electrical conductance (g), (c,c') Seebeck coefficient (*S*), (d,d') thermal conductance by electrons (K_{el}), (e,e') thermal conductance by phonons (K_{ph}), and (f,f') figure of merit (*ZT*) for periodic (blue open circles) and quasiperiodic (red solid circles) segmented nanowires (SNW) with cross sections of (a-f) 9×9 and (a'-f') 4×4 atoms at 25 Kelvins.

SEGMENTED NANOBELTS

In this section, we investigate the thermoelectric properties of periodic and quasiperiodically segmented nanobelts (SNB), as respectively illustrated in the Figures 1(c) and 1(c'). These SNB have a thickness of one atom, a width of seven atoms and segments formed by three bonds with hopping integrals of t_A or t_B along the nanobelts. For the quasiperiodic case, these segments are arranged following the Fibonacci sequence. In the cross section, we have symmetrically distributed non-constant hopping integrals t_1, t_2 and t_3.

In Figures 3, we show (a,a',a") electrical conductivity $\sigma(\mu,T)$, (b,b',b") Seebeck coefficient $S(\mu,T)$, (c,c',c") thermal conductivity by electrons $\kappa_{el}(\mu,T)$, (d,d',d") lattice thermal conductivity $\kappa_{ph}(\mu,T)$, and (e,e',e") figure-of-merit (*ZT*) as functions of chemical potential (μ). The electrical and thermal conductivities are respectively normalized by $\sigma_0 = e^2\Omega_\square/(a\pi\hbar)$ and $\kappa_0 = k_B\omega_\alpha\Omega_\square/(2a\pi)$ of a periodic chain, being $\omega_\alpha = \sqrt{\alpha/M}$. Figures 3(a-e) exhibit results of a fully periodic nanobelt with $t = -1\,eV$, $\alpha = 100\,N/m$ and $\beta = 20\,N/m$, while Figures 3(a'-e') and 3(a"-e") respectively show results for periodic and quasiperiodic SNB with $t_A = 0.3\,t$, $t_B = t$, $\alpha_A = 0.3\alpha$, $\alpha_B = \alpha$, $\beta_A = 0.3\beta$ and $\beta_B = \beta$. These two SNB, as showed in Figures 1(c) and

CAMBRIDGE JOURNALS
http://journals.cambridge.org Downloaded: 15 Jun 2016 IP address: 132.248.12.16

1(c'), have a inhomogeneous cross section of 7×1 atoms connected by hopping integrals $t_1 = 1.248378\,t$, $t_2 = 0.854990\,t$, $t_3 = 0.579251\,t$, central $\alpha_1 = 1.248378\,\alpha$, $\alpha_2 = 0.854990\,\alpha$, $\alpha_3 = 0.579251\,\alpha$, and non-central restoring force constants $\beta_1 = 1.248378\,\beta$, $\beta_2 = 0.854990\,\beta$, and $\beta_3 = 0.579251\,\beta$. The periodic nanobelt and SNB have a length of $\Omega_{\square} = 100663296$ atoms, and the length of quasiperiodic SNB is $\Omega_{\square} = 117264507$ atoms.

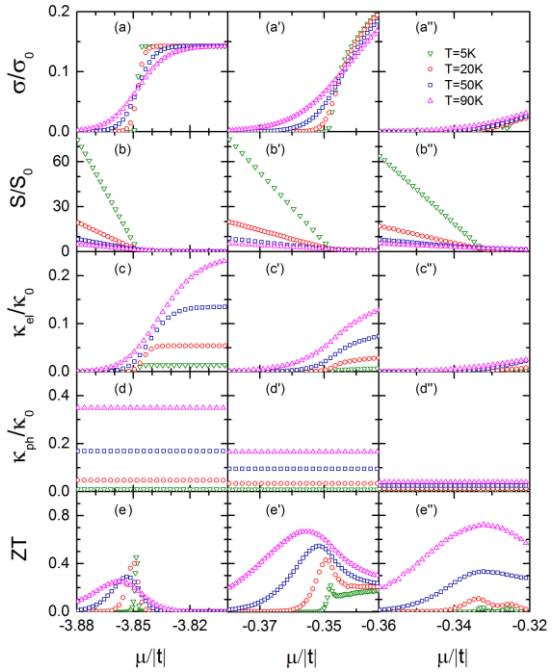

Figure 3. (a,a',a") Electrical conductivity (σ), (b,b',b") Seebeck coefficient (S), (c,c',c") thermal conductivity by electrons (κ_{el}), (d,d',d") thermal conductivity by phonons (κ_{ph}), and (e,e',e") figure of merit (*ZT*) as functions of chemical potential (μ) for periodic (a-e), periodically segmented (a'-e'), and quasiperiodically segmented (a"-e") nanobelts with cross sections of 7×1 atoms at several temperatures.

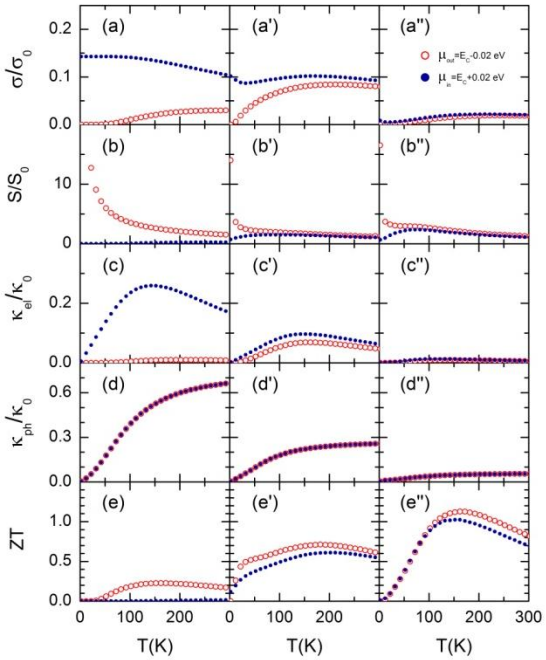

Figure 4. Temperature (*T*) dependence of (a,a',a") electrical conductivity (σ), (b,b',b") Seebeck coefficient (S), (c,c',c") thermal conductivity by electrons (κ_{el}), (d,d',d") thermal conductivity by phonons (κ_{ph}), and (e,e',e") figure of merit (*ZT*) for periodic (a-e), periodically segmented (a'-e'), and quasiperiodically segmented (a"-e") nanobelts with cross sections of 7×1 atoms and $\mu = \mu_{in}$ or μ_{out}.

The analyzed band edges (E_c) in Figure 3 are located at $E_c = -3.8477\,|t|$, $E_c = -0.34784\,|t|$, and $E_c = -0.33734\,|t|$ respectively for the fully periodic nanobelt, periodic and quasiperiodic SNB. Note that the electrical conductivity (σ) of quasiperiodic SNB is significantly smaller than those of periodic nanobelt and periodic SNB. For a given temperature (*T*), the Seebeck coefficient (*S*) is of the same order of magnitude for three analyzed nanobelts. Observe that the thermal conductivities κ_{el} and κ_{ph} of the periodic nanobelt are larger than those of the periodic and quasiperiodic SNB. This fact reduces the thermoelectric figure-of-merit (*ZT*) of periodic nanobelt, in accordance to Eq. (1). In addition, a maximum *ZT* is found in three analyzed nanobelts, since σ grows and *S* diminishes when the chemical potential (μ) increases [10].

Figures 4 show the temperature (*T*) dependence of thermoelectric properties for the same nanobelts as in Figures 3. Observe two behaviors in Figures 4(a-a''); the metallic one (blue solid

CAMBRIDGE JOURNALS
http://journals.cambridge.org Downloaded: 15 Jun 2016 IP address: 132.248.12.16

circles) when $\mu=\mu_{in}=E_c+0.02|t|$ is inside and semiconducting one (open red circles) when $\mu=\mu_{out}=E_c-0.02|t|$ is outside the electronic band. In fact, the thermal conductivity by electrons (κ_{el}) is related to σ through the Wiedemann-Franz law given by $\kappa_{el}=\frac{\pi^2 k_B^2}{3e^2}\sigma T$, when $\mu=\mu_{in}$. Furthermore, *S* decreases monotonically with *T* when $\mu=\mu_{out}$ and κ_{ph} diminishes with the structural disorder. Notice also that there are maximums of *ZT* in the temperature space and they reach large values when $\mu=\mu_{out}$.

CONCLUSIONS

In this paper, we report the thermoelectric properties of periodic and quasiperiodically segmented nanowires and nanobelts of macroscopic length in comparison to fully periodic ones without segments. The calculations were carried out by using the Kubo-Greenwood formula and a real-space renormalization plus convolution method. For all analyzed nanowires and nanobelts, we observe maximums of *ZT* in both temperature and chemical potential spaces. In fact, larger *ZT* are found when $\mu=\mu_{out}$ in comparison to those of $\mu=\mu_{in}$, *i.e.*, semiconductors should be better thermoelectric materials than metals. On the other hand, results reveal the importance of the segmentation in *ZT* and its further improvement when the quasiperiodicity is introduced, since its presence reduces the density of long-wavelength phonons and partially avoids the thermal conduction by phonons at low temperature. Finally, the present study suggests the possibility to improve *ZT* by introducing an inhomogeneous cross section of nanowires or nanobelts, and setting a proper chemical potential position by applying a gate voltage [11].

ACKNOWLEDGEMENTS

This work has been partially supported by UNAM IN113714 and IN114916. Computations were performed at Miztli of DGTIC-UNAM.

REFERENCES

1. E. Macia, *Thermoelectric Materials Advances and Applications* (Taylor & Francis, 2015) pp. 38.
2. S. C. Andrews, M. A. Fardy, M. C. Moore, S. Aloni, M. Zhang, V. Radmilovic, and P. Yang, *Chem. Sci.* **2**, 706 (2011).
3. Z. L. Wang, *Adv. Mater*. **15**, 432 (2003).
4. G. H. Dong, Y. J. Zhu, G. F. Cheng, and Y. J. Ruan, *J. Alloy. Compd*. **550**, 164 (2013).
5. T. M. Tritt (Ed.), *Thermal Conductivity: Theory, Properties & Applications* (Kluwer, 2004) pp. 3.
6 V. Sanchez and C. Wang, *Phys. Rev. B* **70**, 144207 (2004).
7. T. Markussen, *Nano Lett.* **12**, 4698 (2012).
8. J. K. Flicker and P. L. Leath, *Phys. Rev. B* **7**, 2296 (1973).
9. P. Alfaro, R. Cisneros, M. Bizarro, M. Cruz-Irisson, and C. Wang, *Nanoscale* **3**, 1246 (2011).
10. G. J. Snyder and E. S. Toberer, *Nature Materials* **7**, 105 (2008).
11. Y. Tian, M. R. Sakr, J. M. Kinder, D. Liang, M. J. MacDonald, R. L. J. Qiu, H.-J. Gao, and X. P. A. Gao, *Nano Lett.* **12**, 6492 (2012).

CAMBRIDGE JOURNALS
http://journals.cambridge.org Downloaded: 15 Jun 2016 IP address: 132.248.12.16

UNAM POSGRADO Ciencia e Ingeniería de Materiales

COORDINACION DEL POSGRADO EN CIENCIA E INGENIERIA DE MATERIALES
UNIDAD DE POSGRADO, EDIFICIO "C", UNAM
CIRCUITODE POSGRADOS, CIUDAD UNIVERSITARIA
04510 MEXICO, D.F.
TEL: 56224730 Y 56237017
pceim-asist@iim.unam.mx

CONSTANCIA DE EXAMEN DE GRADO

El(a) Dra. Mirna Villavicencio Torres

en su carácter de Secretario del Sínodo del Examen de Grado de Maestra en Ciencia e Ingeniería de Materiales, de la UNAM, por la modalidad de examen general de conocimientos de la alumna

GUTIÉRREZ RODRÍGUEZ ADRIANA PATRICIA

hago constar que obtuvo la calificación de APROBADO,

el día 26 de julio de 2016.

Atentamente
"POR MI RAZA HABLARÁ EL ESPÍRITU"
EL SECRETARIO

Mirna Villavicencio Torres

Firma

COORDINACION DE POSGRADO EN CIENCIA E INGENIERIA DE MATERIALES

c.c.p. Coordinador del Posgrado en Ciencia e Ingeniería de Materiales.

UNIVERSIDAD NACIONAL AUTÓNOMA DE MÉXICO

POSGRADO EN CIENCIA E INGENIERÍA DE MATERIALES
FACULTAD DE CIENCIAS

FENÓMENO DE RESONANCIA EN NANOALAMBRES RAMIFICADOS

QUE PARA OPTAR POR EL GRADO DE:
MAESTRA EN CIENCIA E INGENIERÍA DE MATERIALES

PRESENTA:
ADRIANA PATRICIA GUTIÉRREZ RODRÍGUEZ

TUTOR PRINCIPAL
DRA. VICENTA SÁNCHEZ MORALES
FACULTAD DE CIENCIAS

MIEMBROS DEL COMITÉ TUTOR
DR. CHUMIN WANG CHEN
INSTITUTO DE INVESTIGACION EN MATERIALES
DR. RAUL P. ESQUIVEL SIRVENT
INSTITUTO DE FÍSICA

CIUDAD UNIVERSITARIA, A 26 DE MAYO DE 2016.

Agradecimientos

Mi mayor agradecimiento a mi esposo Amílcar y a mis hijos Aízen y Aldebarán, mis principales motores y motivos para realizar este trabajo. Gracias por su apoyo y su amor incondicional, por esperarme en las noches para dormir y por la paciencia que me tuvieron durante todo el periodo de estrés. Gracias por creer en mí y por animarme a seguir de pie. Los amo.

A padres Patricia y Esteban, mis primeros maestros. y mis modelos a seguir. Gracias a su amor, apoyo, confianza y valores inculcados es que he logrado llegar hasta donde estoy. Me han brindado muchas facilidades para cumplir mis sueños y si no fuera por ustedes yo no sería la profesionista que soy el día de hoy. Gracias papás.

Gracias a mi hermano David y a su esposa Alejandra que me brindaron el apoyo y me abrieron las puertas de casa muchas veces, porque sin ustedes no hubiera concluido mi escrito.

A mi equipo de trabajo conformado por la Dra. Vicenta Sánchez, el Dr. Chumin Wang, el Dr. Raul Esquivel, el M. en C. I. M. Fernando Sánchez y el M. en C. I. M. Guillermo Munguía, por la guía y el enriquecimiento profesional y personal.

Le agradezco al Dr. Francisco Miguel Castro, al Dr. Miguel Cruz, al Dr. Oracio Navarro y a la Dra. Mirna Villavicencio por sus comentarios para corregir y enriquecer este trabajo.

Finalmente, agradezco a la Universidad Nacional Autónoma de México por abrirme las puertas, al CONACyT por el apoyo económico que me permitió ser alumna de tiempo completo, a la DGAPA por la beca recibida a través del proyecto PAPIIT IN114916 para obtener el grado y a la DGTIC por permitirme usar las supercomputadoras.

UNIVERSIDAD NACIONAL AUTÓNOMA DE MÉXICO

CONSTANCIA DE EXAMEN

Dra. Vicenta Sánchez Morales, secretario del jurado que examinó a **Abraham Lima Buendia** para optar por el grado de **Maestro en Ciencias (Física)** hace constar que obtuvo la calificación de Aprobado con Mención Honorífica

Ciudad Universitaria, Cd. Mx., a 27 de enero de 2017.

EL SECRETARIO DEL JURADO

FIRMA

pcf
posgrado en ciencias físicas
u n a m

Folio: 4078003011718

El interesado deberá consultar la página
www.dgae.unam.mx para saber el avance
en la expedición del pergamino.

UNIVERSIDAD NACIONAL AUTÓNOMA DE MÉXICO

POSGRADO EN CIENCIAS FÍSICAS
FACULTAD DE CIENCIAS

INTERACCIÓN ELECTRÓN-ELECTRÓN EN LA LOCALIZACIÓN Y SUPERCONDUCTIVIDAD EN SISTEMAS APERIÓDICOS

PROTOCOLO DE INVESTIGACIÓN
QUE PARA OPTAR POR EL GRADO DE:
MAESTRO EN CIENCIAS (FÍSICA)

PRESENTA:
ABRAHAM LIMA BUENDIA

TUTOR PRINCIPAL:
DRA. VICENTA SÁNCHEZ MORALES
FACULTAD DE CIENCIAS, UNAM

MIEMBROS DEL COMITÉ TUTOR
DR. CHUMIN WANG CHENG
INSTITUTO DE INVESTIGACIONES EN MATERIALES, UNAM

DR. LUIS ANTONIO PÉREZ LÓPEZ
INSTITUTO DE FÍSICA, UNAM

MÉXICO D.F. ENERO DE 2017

Agradecimientos

"El agradecimiento es la memoria del corazón"
Lao Tse

Listar a todas las personas a quienes debo agradecer mi formación académica y humana, seguramente produciría un resultado inconmensurable, sin embargo, en esta lista destaca la ***Dra. Vicenta Sánchez Morales*** por haberme permitido formar parte de su grupo de trabajo y haber sido mi tutora durante mí formación como maestro en ciencias, convirtiéndose en mi brújula académica y moral. De igual manera agradezco inmensamente al ***Dr. Chumin Wang Chen*** y al ***Dr. Luis Antonio Pérez López*** por darme su apoyo académico, por compartir su tiempo y sus experiencias ayudándome a la elaboración de este protocolo de investigación.

En forma conjunta agradezco al ***Dr. Oracio Navarro***, al ***Dr. Rafael Baquero***, al ***Dr. Raúl P. Esquivel*** y a la ***Dra. Renela M. Valladares*** por los comentarios que ayudaron a culminar y mejorar este texto.

A mi hermano y maestro Jesús, por ser mi guía y por estar a mi lado incondicionalmente, a mis amigos Julio, Azucena, Jesús, Daniel, Fernando, Guillermo, Carlos, Gustavo, Edzna, Marco, Marisol, Youssef, Yaithd, Miguel, Odín, Alvar y Charly, así como a todas esas personas que al igual que ellos me han brindado su apoyo cuando más lo he necesitado dándome consejos, ánimos y fortaleza cuando sentía que el mundo no podría seguir avanzando.

Agradezco a la Universidad Nacional Autónoma de México y al Posgrado en Ciencias Físicas UNAM por haberme brindado la oportunidad de llevar acabo mis estudios de maestría y proporcionarme las bases para empezar mí vida como investigador. Al departamento de Física de la Facultad de Ciencias por proporcionarme un espacio dentro del cubículo 303 donde he desarrollado mis labores como estudiante de posgrado y a todos mis alumnos que también han contribuido a mi formación profesional.

Finalmente agradezco a ***CONACYT*** por haberme proporcionado una beca para poder financiar mis estudios de maestría, a la ***DGAPA*** por el apoyo recibido a través del proyecto PAPIIT IN114916 y a la DGTIC por permitirme usar las supercomputadoras Miztli.

Engineering Information Institute

2016 ENGII Conferences Program Guide

Chemistry, Biology and Medicine

Nanjing, China

June 1-3, 2016

www.engii.org

Scientific Research Publishing

千人智库
高效引才 科学决策

EDCs, while photochemical and photocatalytic processes have proved themselves as perspective methods for water purification and disinfection from these compounds. Besides the broad number of investigations devoted to decomposition of BPs using photochemical approaches, there is almost no information about mechanistic aspects regarding the photochemistry of BPs.

In this work aqueous photochemistry of three bisphenols (4,4'-hydroxyphenylmethane (BPF), 4,4'-hydroxyphenylethane (BPE) and 4,4-Bis(4-hydroxyphenyl)valeric acid (DPA)) was studied by means of stationary (XeBr excimer lamp, 282 nm) and laser flash photolysis (6 ns, Nd:YAG laser, 266 nm). Main attention was paid to determination of primary photochemical processes, nature, spectral and kinetic properties of excited states and primary intermediates, rate constants of their reactions. Also, final photoproducts and quantum yields of the photolysis were determined and on the basis of obtained data scheme of BPs photolysis was proposed.

This work was financially supported by Russian Foundation for Basic Research (grants № 16-33-00335 mol_a, 14-03-00692).

[1] T. Suzuki, Y. Nakagawa, I. Takano, K. Yaguchi, Y. Kazuo. Environ. Sci. Technol. 2004, 38, 2389–2396

[2] M.-Y. Chen, M. Ike, M. Fujita. Environ. Toxicol. 2002, 17, 80"

Article ID: CPC2016_90007

Title: Photophysical Properties of Perylenetetra-carboxylic Diimide Dimers with Slipped "face-to-face" Stacked Structure and Different Bay Substitutions

Name: Heyuan Liu

Affiliation: China University of petroleum (East China)

E-mail: liuheyuan123@upc.edu.cn

Abstract

A series of perylenetetracarboxylic diimides (PDIs) dimers with slipped "face-to-face" stacked structure and different substituents at the bay positions have been synthesized and the molecular structures are characterized by 1H NMR, MALDI-TOF and elemental analysis. And different sub-stituents at the bay positions of the PDI ring bring about various steric hindrance. These different steric hindrance have caused significant differences on the absorption and emission spectra. The correlation between the photophysical properties and the molecular structure is discussed.

Article ID: CPC2016_90006

Title: Photonic localization and transmittance in macroscopic aperiodic multilayers

Name: Vicenta Sanchez

Affiliation: Universidad Nacional Autonoma de Mexico

E-mail: vicenta@unam.mx

Abstract

The propagation of a wave through a medium is very sensitive to the structures at wavelength scale. In consequence, dielectric materials with periodic, quasiperiodic, or aperiodically ordered structures are considered excellent candidates for making optical components capable of reflecting, confining or guiding light, just as electrons and holes in electronic devices. These materials are called photonic crystals. In this work, we study the optical properties of quasiperiodic and aperiodic heterostructures, whose layers are ordered following the generalized Fibonacci sequence defined by the substitution rules of A->A^{m}B^{n} and B->A. To carry out this study, we developed a new unified renormalization method for the quasiperiodic and aperiodic transfer matrixes in order to analyse the transmittance for a macroscopic number of layers. In particular, we calculate the transmittance in quasiperiodic or aperiodic multilayers for transverse electric (TE) and magnetic (TM) polarizations by varying parameters such as the angle of incidence, refractive index, layer thickness and wavelength. We find an analytical expression for the transmittance, when the layers follow a generalized Fibonacci sequence for several generations. In addition, we find the self-similarity in transmittance spectra when the arrangement of layers follows a quasiperiodic sequence (n=1) and a zone where the spectrum presents an oscillating behaviour if the order is aperiodic (n>1),

when the incidence angle is null. Finally, the photonic localization is investigated by looking at the Lyapunov coefficient and its results are compared with the transmmitance ones for different incident angles.

Article ID: CPC2016_90008

Title: Theoretical design of boron nitride based catalysts for oxygen reduction reaction

Name: Andrey Lyalin

Affiliation: National Institute for Materials Science (NIMS)

E-mail: LYALIN.Andrey@nims.go.jp

Abstract

It is demonstrated that boron nitride (BN), which is catalytically inert insulator with a wide band gap, can be functionalized and act as an electrocatalyst for oxygen reduction reaction (ORR). Such functionalization can be achieved by the nitrogen doping or deposition of the BN nanosheets on some transition metals, such as Ni(111) or Au(111). Density-functional theory calculations show that interaction of BN nanosheets with the metal supports results in formation of the band states in the forbidden zone of BN, as it occurs in the case of Ni(111) support or a slight protrusion of the unoccupied BN states toward the Fermi level as it observed for Au(111) support. Modification of the BN band structure can be explained by the orbital mixing and electron sharing at the interface. Analysis of the binding preference and adsorption energies of the ORR intermediates on functionalized BN nanosheets demonstrate possibility of ORR. It is experimentally proved that overpotential for ORR at the gold electrode is significantly reduced by depositing BN nanosheets (Fig. 1). The present study demonstrates the possibility to functionalize inert materials to become ORR catalysts, opening new ways to design effective Pt-free catalysts for fuel cells based on materials never before considered as catalysts.

CMD26 - *Condensed Matter in Groningen* is an international conference covering all aspects of condensed matter physics, including soft condensed matter, liquid physics, biophysics, materials science, quantum physics and quantum simulators, low temperature physics, quantum fluids, strongly correlated materials, semiconductor physics, magnetism, surface and interface physics, electronic, optical, structural, and mechanical properties of materials, acoustics, and disordered media. An important place will be granted to interdisciplinary topics as well as to the development of research infrastructure in Europe.

The scientific programme will consist of a series of plenary and semi-plenary talks and **Mini-colloquia**. Within each Mini-colloquium, there will be invited lectures, oral contributions and posters.

CMD26 - *Condensed Matter in Groningen* is organized by the Condensed Matter Division of the European Physical Society (EPS) with support from the Foundation for Fundamental Research on Matter (FOM), which is part of the Netherlands Organization for Scientific Research (NWO).

CMD26 - *Condensed Matter in Groningen* is the next in the series of biyearly EPS-CMD conferences, the last of which was held in Paris. The meeting will be held **from September 4th through September 9th, 2016,** in the Martiniplaza Conference Centre in Groningen, The Netherlands.

Groningen by night

Postersession Tuesday
September 6th ,12:40 – 15:00

From topological materials to topotronics

Eric de Vries	P27
Dziawa	P28
Voerman	P29
Eduardo Castro	P30
Dzsaber	P31

Quantum One-Dimensional Systems

Puviani	P32
Roddaro	P33
Calzona	P34
Goncalves	P35
Linker	P36
Lichtenstein	P37
Pino D'Amico	P38
Barbarani	P39
Cikit	P40
Sanchez	P41

Physics of protein nanoshells

Marchetti	P42
Holmes	P43
Denning	P44
Van der Borg	P45
Hashemi Shabestari	P46
Blijleven	P47
Maity	P48
Martin Gonzales	P49
Jiménez Zaragoza	P50
Sorkin	P51
Maassen	P52
Lherbette	P53
Paquay	P54

P41: Electronic localization and transport in macroscopic generalized Fibonacci lattices: A renormalization approach

Colloquium: Quantum One-Dimensional Systems

Fernando Sanchez[1], Vicenta Sanchez[1], Chumin Wang[2]

[1]*Facultad de Ciencias, Universidad Nacional Autonoma de Mexico, CIUDAD DE MEXICO, Mexico*
[2]*Instituto de Investigaciones en Materiales, Universidad Nacional Autonoma de Mex, CUIDAD DE MEXICO, Mexico*

The structural disorder of a solid can profoundly modify the nature of electronic states. It is well known that they are all extended in periodic lattices and exponentially localized in random-disordered systems of one and two dimensions [1]. In particular, electronic transport and wavefunction localization are two closely related phenomena, but their behavior in truly macroscopic aperiodic lattices is a non-widely addressed issue. In this work, we study the electrical conductivity of generalized Fibonacci (GF) lattices [2] through the Kubo-Greenwood formula, while the localization of electronic wavefunction is analyzed by means of the Lyapunov exponent and participation ratio (*PR*) [3]. For periodic chains, an analytical expression of the Lyapunov exponent is obtained. We have also developed for the first time a real-space renormalization method to calculate the *PR* of macroscopic GF lattices described by tight-binding Hamiltonians. Moreover, we report a novel unified renormalization method for the Kubo-Greenwood formula applied to GF chains. For quasiperiodic lattices, the results reveal a power-law decay of the spectral averages for both *PR* and DC conductivity when the system length increases. In addition, we present a systematic analysis of the AC conductivity spectra observing truly large resonant peaks in comparison to the ballistic one. The electrical conductance of GF nanowires is also investigated by combining the renormalization method to the convolution theorem [4]. Finally, the results suggest that *PR* could not be proper for the analysis of critically localized states.

[1] E. Abrahams, P.W. Anderson, D.C. Licciardello, and T.V. Ramakrishnan, *Phys. Rev. Lett.* **42**, 673 (1979).
[2] A. Chakrabarti and S.N. Karmakar, *Phys. Rev. B* **44**, 896 (1991).
[3] R. Oviedo-Roa, L.A. Pérez, and C. Wang, *Phys. Rev. B* **62**, 13805 (2000).
[4] V. Sánchez and C. Wang, *Phys. Rev. B* **70**, 144207 (2004).

P42: Detection and Mechanical Characterization of Lipid Nanoshells using Atomic Force Microscopy

Colloquium: Physics of protein nanoshells

Margherita Marchetti[1], Daan Vorselen[1], Gijs Wuite[1], Wouter Roos[2]

[1]*VU University Amsterdam, AMSTERDAM, The Netherlands*
[2]*Rijksuniversiteit Groningen, GRONINGEN, The Netherlands*

Multilamellar vesicles (MLVs) have beneficial properties over currently used unilamellar vesicles (LUVs) for drug delivery, such as more hydrophobic volume for hydrophobic drugs. Moreover, they may have altered mechanical properties, which are suggested to influence cellular uptake. We investigated the mechanics of small MLVs using atomic force microscopy (AFM). We quantified the mechanical response of single liposomes by AFM nano-indentation. Analyzing the total distance of breaks in force-indentation curves we were able to determine the degree of lamellarity (1-5) of individual vesicles. This allowed us to characterize the influence of multilamellarity on morphological and mechanical properties. We found that MLVs, upon adhesion with a surface, stay in a more spherical shape respect to ULVs. Furthermore, the stiffness increases linearly with the addition of each lipid bilayer (0.0027 N/m added stiffness). We speculate that the added osmotic pressure, due to the inner and less-deformed vesicles, together with their bending, cause the observed stiffening. These results suggest that small MLVs might have beneficial properties for cellular uptake.

EMN BUDAPEST MEETING

September 9-13, 2016

Budapest, Hungary

Program & Abstracts

organization and function while minimizing the effect of printing on cell viability and without compromising printing fidelity and stability of the construct.

Many bioinks have been formulated for various cells types, but those currently used for 3D printing still have challenges and limitations, mainly low cell viability during printing and limited resolution and fidelity.
To overcome these limitations, we developed a new concept of extrusion-based bioprinting technique, which implements a microfluidic control in the dispensation of the bioink. The coupling of microfluidic platforms with the dispensing system is made possible by the use of a coaxial extrusion head that induces the solidification of the bioink in the form of a hydrogel simultaneously to its deposition.

In particular, among other components, the bioink contains alginate, whose gelation is induced by exposing it to a crosslinking solution containing calcium ions. The bioink and the crosslinking solution are delivered respectively through the internal and external needles of a coaxial-needles system. At the ending tip of the dispensing head the two solutions meet causing the immediate solidification of the bioink due to the ionic crosslinking of alginate. In this way, it is possible to deposit hydrogel fibers with dimensions ranging between 150 and 300 μm. The printing conditions described above are mild since bioink viscosity is low and crosslinking conditions can be tuned to be harmless toward encapsulated cells.

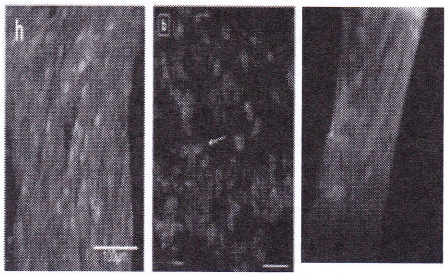

Figure1.Examples of bioprinted constructs embedding different cell types (from left to right): human umbilical vein endothelial cells (HUVECs) embedded in a chemically crosslinked gelatin methacrylate gel; BM-Human Mesenchymal Stem Cells (BM-hMSCs) embedded in a chemically crosslinked gelatin methacrylate-hyaluronic methacrylate-chondroitin methacrylate gel; myoblasts embedded in PEGylated fibrinogen gel.

1. C. Colosi, M. Costantini, R. Latini, S. Ciccarelli, A. Stampella, A. Barbetta, M. Massimi, L. Conti Devirgiliis, M. Dentini, *Journal of Material Chemistry B* **2**, 6779 (2014).
2. C. Colosi, S.-R. Shin, V. Manoharan, S. Massa, M. Costantini, A. Barbetta, M. R. Dokmeci, M. Dentini, A. Khademhosseini, *Advanced Materials* **28**, 677 (2016).
3. M. Costantini, J. Idaszek, K. Szoke, J. Jaroszewicz, M. Dentini, A. Barbetta, J. E. Brinchmann, W. Święszkowski *Biofabrication*, **8**, 035002, (2016).

P-01: Quasiperiodicity and mirror symmetry in photonic devices

Vicenta Sanchez[1], J. Guillermo Munguia-Fernandez[1], Chumin Wang[2]

[1]*Departamento de Física, Facultad de Ciencias, Universidad Nacional Autónoma de México*
[2]*Instituto de Investigación en Materiales, Universidad Nacional Autónoma de México*
Email: chumin@unam.mx

The wave propagation through a dielectric medium has been shown to be very sensitive to its structure at wavelength scale [1]. In consequence, photonic devices based on dielectric layers ordered following the periodic or quasiperiodic sequence are capable of reflecting, confining, guiding or filtering lights, just as electrons and holes in electronic devices [2]. In this work, we report a comparative study of the light transmission in dielectric heterostructures with Fibonacci, Thue-Morse, Rudin-Shapiro, Triadic Cantor and Period-doubling sequences [1,3]. Furthermore, heterostructures with mirror symmetry can be obtained by concatenating an aperiodic multilayer to its mirror structure or conjugate one. For example, the sequence of a mirror Fibonacci multilayer can be written as ABAAB-BAABA, while a conjugate one as ABAAB-BABBA. Within the quarter-wave condition, where the optical thickness of each layer is $\lambda/4$, we observe a perfect transmission sharp peak at λ for multilayers with mirror symmetry. The full width at half maximum (FWHM) of this peak is investigated in detail for analyzed periodic and aperiodic multilayers with mirror symmetry, keeping constant the total number of layers and the refraction-index ratio of layers A and B. In addition, we investigate the variation of transmittance spectra with the incident angle for both transversal electric (TE) and transversal magnetic (TM) polarizations. Finally, the results of this study show the decisive importance of heterostructural order in the design and fabrication of photonic devices.

This work has been partially supported by UNAM-PAPIIT-IN114916. Computations were performed at Miztli of DGTIC-UNAM

1. E. Maciá, *Rep. Prog. Phys.* **75**, 036502 (2012).
2. J. D. Joannopoulos, S. G. Johnson, J. N. Winn, and R. D. Meade, *Photonic Crystals: Molding the Flow of Light*, 2nd Ed. (Princeton University Press, 2008).
3. A. Palavicini and C. Wang, *Optics and Photonics Journal* **3**, 20 (2013).

Materials Research Society
The Materials Gateway

Abstract Status

DocumentID/ControlID:	2559910
Title:	Resonant AC and Optical Absorption Spectra of Aperiodic Branched Nanowires
Paper Number:	NM1.13.17
Presentation Date:	November 30, 2016
Presentation Time:	08:00 PM to 10:00 PM
Presentation Type:	Poster
Room:	Hynes, Level 1, Hall B
Status:	**Accepted**

Please complete this form and click "Submit" at the bottom to confirm your presentation.

Your Name Vicenta Sanchez

(•) **Yes, The abstract will be presented.**

( ) **No, we will not be able to present the abstract. Please withdraw it.**

Confirm

2016 Materials Research Society Fall Meeting
Symposium NM1: Semiconducting Nanowires, Nanoribbons and Heterostructures - Synthesis, Characterizations and Functional Devices (Abstract No. 2559910)

Resonant AC and optical absorption spectra of aperiodic branched nanowires

Vicenta Sanchez[1], Fernando Sanchez[1] and Chumin Wang[2]

[1]*Departamento de Física, Facultad de Ciencias, Universidad Nacional Autónoma de México, CDMX, México*
[2]*Instituto de Investigaciones en Materiales, Universidad Nacional Autónoma de México, CDMX, México*

The electronic transport induced by oscillating electromagnetic field in non-crystalline nanostructures is still an unclear issue, where the interference between the electronic wavefunction and aperiodic potentials has multiple consequences. Recently, branched nanowires with tunable three-dimensional (3D) morphology have been obtained, and they have wide applications in energy conversion and storage devices [1]. Nonlinear electrical properties of branched nanowires have also been reported [2]. In general, the aperiodic arrangement of branches avoids the use of the reciprocal space and then, such systems should be addressed in the real space. In this work, a renormalization plus convolution method developed for the Kubo-Greenwood formula [3] is used to investigate the electronic transport in branched nanowires. We report a three order-of-magnitude enhancement in comparison to the ballistic alternating current (AC) conductivity, when periodic or quasiperiodically placed branches are introduced to an otherwise periodic nanowire, which are connected to two semi-infinite periodic leads at its ends [4]. Moreover, the temperature variation analysis suggests the possibility to observe these resonant AC conducting peaks at room temperature. Given that the imaginary part of the dielectric function is proportional to the AC conductivity, we further calculate the optical absorption in these aperiodic branched nanowires, finding significant improvements in their absorption spectra at infrared range, useful for the solar cell applications.

This work has been partially supported by UNAM-IN114916. Computations were performed at Miztli of DGCTIC, UNAM.

[1] C. Cheng and H.J. Fan, *Nano Today* **7**, 327 (2012).
[2] D.B. Suyatin, J. Sun, A. Fuhrer, D. Wallin, L.E. Fröberg, L.S. Karlsson, I. Maximov, L.R. Wallenberg, L. Samuelson and H.Q. Xu, *Nano Lett.* **8**, 1100 (2008).
[3] V. Sanchez and C. Wang, *Phys. Rev. B* **70**, 144207 (2004).
[4] V. Sanchez and C. Wang, *Phil. Mag.* **95**, 326 (2015).